Investigating tumor metabolism with mass spectrometry imaging

by

Madison Shiyuk

B.Sc., University of Victoria, 2024

A Thesis Submitted in Partial Fulfillment of

the Requirements for the Degree of

MASTER OF SCIENCE

in the Department of Biochemistry and Microbiology

University of Victoria

We acknowledge and respect the Lək̓ʷəŋən (Songhees and Xʷsepsəm/Esquimalt) Peoples on whose territory the university stands, and the Lək̓ʷəŋən and W̱SÁNEĆ Peoples whose historical relationships with the land continue to this day.

Supervisory Committee

Investigating tumor metabolism with mass spectrometry imaging

by

Madison Shiyuk
B.Sc., University of Victoria, 2024

Supervisory Committee

Dr. David R. Goodlett, Supervisor
Department of Biochemistry and Microbiology

Dr. Helena Pětrošová, Departmental Member
Department of Biochemistry and Microbiology

Dr. Julian J. Lum, Departmental Member
Department of Biochemistry and Microbiology

Dr. Kyle Duncan, Outside Member
Department of Biochemistry and Microbiology

Abstract

Tumor metabolism plays a critical role in shaping the tumor immune microenvironment and contributes to immunosuppression in cancer. In ovarian cancer, metabolic competition and accumulation of immunoregulatory metabolites can impair T cell activation and promote exhaustion, resulting in immunotherapeutic resistance and poor patient outcomes. These tumors are highly heterogeneous, and metabolic interactions between cancer cells and immune cells often occur within spatially restricted microenvironments. Thus, mass spectrometry imaging (MSI) has emerged as a powerful technique for spatial metabolomics, enabling label-free mapping of metabolites and lipids directly within tissue sections while preserving tissue organization. However, several analytical limitations remain for spatial profiling of tumor immune microenvironments. Small molecules, such as methionine cycle metabolites, are implicated in immune modulation in tumors, yet they remain difficult to detect using conventional approaches for matrix-assisted laser desorption/ ionization mass spectrometry imaging (MALDI MSI). Further, use of a single MSI modality results in inherent specificity for target molecular classes, motivating development of multimodal workflows integrating two or more MSI approaches.

The objective of this work was to develop and apply MSI-based workflows to investigate metabolic heterogeneity within the tumor immune environment. Methodological approaches were established for spatial detection of methionine cycle metabolites using MALDI MSI with on-tissue chemical derivatization. A complementary multimodal workflow was developed to support multimodal imaging experiments combining metabolite, lipid, and immune marker detection within tumor tissues.

Application of multimodal workflows revealed spatial metabolic differences associated with immune cell infiltration in murine tumor models and human ovarian cancer specimens. Regions enriched for CD8+ T cells exhibited distinct metabolic signatures, including increased abundance of several amino acids and lipids containing arachidonic acid fatty acyl chains. Together, this work demonstrates the utility of mass spectrometry imaging for spatially resolving metabolic features of the tumor immune microenvironment and provides technical foundations for integrating metabolite, lipid, and protein imaging to study immune-metabolic interactions in cancer.

Table of Contents

Contents

List of Tables

List of Figures

List of Abbreviations

2,5-DHA……..2,5-dihydroxyacetophenone

2,5-DHB……2,5-dihydroxybenzoic acid

2,5-DHT……..2,5-dihydroxyterephthalic acid

4-APEBA……..4-(2-((4-bromophenethyl)-dimethylammonio)-ethoxy)-benzaminium dibromide

9AA……9-aminoacridine

BH……...Benjamini-Hochberg

CA9……carbonic anhydrase 9

CD3……cluster of differentiation 3

CD4……cluster of differentiation 4

CD8……cluster of differentiation 8

CHCA…….α-cyano-4-hydroxycinnamic acid

DAN-HCl……..1,5-diamonionapthalene hydrochloric acid

EDC……1-ethyl-3-(3-dimethylaminopropyl)carbodiimide

FDR……..false discovery rate

GLUT-1……..glucose transporter 1

GSH……...glutathione

IHC……...immunohistochemistry

MALDI ……...matrix-assisted laser desorption/ ionization

MR……methionine restricted (diet)

MSI……...mass spectrometry imaging

nanoDESI…….nanospray desorption electrospray ionization

NEDC……N-(1-napthyl)ethylenediamine dihydrochloride

PC-MT™……..photocleavable mass tag (AmberGen)

PD-1……..programmed cell death protein 1

RMS…….....root mean square

SAH……..S-adenosyl homocysteine

SAM…….S-adenosyl methionine

TAHS……..*N,N,N*-trimethylammonioanilyl hydroxysuccinimidyl carbamate iodide

TIC…….total ion current

TIL……..tumor-infiltrating lymphocytes

TIMS…….trapped ion mobility spectrometry

TME…….tumor microenvironment

Acknowledgements

I would like to express deep gratitude and appreciation for many people who have contributed to my learning and success over the past two years. Through the course of this degree, I have worked harder than I ever thought possible, and I would not have been able to do so, let alone have fun with it, without the support of so many important people in my life.

First and foremost, I would like to thank Dr. Helena Pětrošová for her instrumental role in my personal and professional growth. Helena, you somehow manage to find the perfect balance between holding me to high standards and believing in my ability to reach them. I am endlessly appreciative for the time and effort you have put into supporting me through this project.

I would also like to thank Dr. Dave Goodlett for his guidance and support in my growth from an undergraduate honors student to a (soon-to-be) holder of an M.Sc. degree. Thank you for your endless patience and for sharing your vast knowledge with me.

Thank you to the members of my supervisory committee, Dr. Kyle Duncan and Dr. Julian Lum, for their critical roles in the success of my project. It has been a pleasure to work with and learn from you.

I have many colleagues to thank, for their roles in demonstrating scientific excellence and for being a joy to work with, especially Angela Jackson, Kate McMurray, Sophie Culos, Gillian Leach, Ken Weke, and Silas Porter Crenna. It has been a privilege to learn from you and with you, whether on the topic of mass spectrometry or plants. I would also like to extend my

gratitude to Dave Schibli and Derek Smith for all their behind-the-scenes work in keeping our amazing center running. Finally, thank you to all the past and present members of the Goodlett Lab and UVic Genome BC Proteomics Centre for creating such a memorable and enjoyable experience. I will miss all of you!

Thank you to my family for your immeasurable support in my academic journey. To my parents, Tyson and Tammy, thank you for teaching me to work hard and to follow my passions. For my whole life, I have been able to look up to two people who love their careers, love to learn, and work incredibly hard to support our family. I would not have become the person I am today without you. Thank you.

To my sisters, Allie, Olivia, and Kiera. Each of you inspires and motivates me every day. The high standards you hold for yourselves have pushed me to keep up with you, let alone try to be a good role model. Thank you for all the laughs, conversations, and support that keep me going.

Last, but not least, I owe a big, huge, thank you to Dawson. You have been my lifeline through the ups, downs, and chaos of this program. Thank you for getting me through each day by keeping me fed, rested, supported, cared for, and most importantly, happy. I am certain I would not have been able to do this without you. Thank you.

Chapter 1: Introduction

1.1 Ovarian carcinoma

1.1.1 Ovarian carcinoma epidemiology and treatment

Ovarian carcinoma is one of the most lethal gynecological malignancies in Canada, with a 5-year net survival rate of 44% [1]. Despite representing a relatively low proportion of overall cancer diagnoses, the mortality burden of ovarian carcinoma is disproportionately high. National projections for 2025 estimate that ovarian cancer accounts for approximately 2.5% (n = 3,100) of new cancer cases but up to 4.9% of cancer-related deaths (n = 2,000) [2]. In line with these predictions, ovarian cancer demonstrates a high global age-standardized mortality to incidence ratio (0.51) [3], reflecting poor long-term outcomes despite advances in cancer therapeutics. High mortality rates are driven by late diagnosis, limited durability of current treatments, and high rates of platinum-resistant relapse, representing an urgent need for improved understanding of ovarian cancer pathology and development of more effective treatment strategies.

Late-stage diagnosis of ovarian cancer is a major contributor to poor clinical outcomes. Prior to diagnosis with ovarian cancer, approximately 95% of patients experience nonspecific symptoms including abdominal pain, bloating, and urinary urgency or frequency [4]. The gradual onset and nonspecific nature of these symptoms often delays investigations, resulting in 80% of ovarian cancer diagnoses occurring in advanced stages (FIGO stages III-IV) [5]. Advanced-stage ovarian cancer is associated with markedly worse survival; in the United States, five-year survival rates for stage III-IV ovarian cancer are 10-40%, in comparison to 70-95% for patients diagnosed in

stages I-II [6]. In addition to influencing prognosis, disease stage at diagnosis plays a critical role in guiding clinical management and treatment options.

Treatment strategies for ovarian cancer are guided by disease extent and patient-specific risk factors. Early-stage disease is typically managed with cytoreductive surgery followed by platinum chemotherapy, most commonly carboplatin plus paclitaxel [5,7,8]. In contrast, patients presenting with advanced-stage disease require more intensive and complex treatment approaches. These strategies often combine cytoreductive surgery, systemic chemotherapy, and targeted agents directed at specific oncogenic pathways [9–11]. Despite minor refinements to platinum-based regimens [12], the core components of ovarian cancer therapies have remained largely unchanged for decades. Recent therapeutic innovations have primarily focussed on targeted agents to exploit specific drivers of tumor growth and progression, particularly for advanced disease.

Targeted therapies have provided modest clinical benefits for select patient populations but have not substantially altered overall survival at the population level. One targeted strategy involves inhibiting angiogenesis by blocking vascular endothelial growth factor (VEGF) signalling. Bevacizumab, a monoclonal antibody targeting VEGF, extended progression-free survival by 2-4 months in phase III clinical trials [13,14]. However, a subsequent meta-analysis found no significant improvements in overall survival [15].

Another targeted approach involves inhibition of DNA repair pathways using poly(ADP-ribose) polymerase (PARP) inhibitors such as olaparib and niraparib. These therapies exploit defects in homologous recombination-mediated DNA repair in patients with breast cancer gene (BRCA)-

mutated or homologous recombination-deficient (HRD) tumors [16,17]. In a phase III clinical trial, olaparib was associated with improved 7-year survival rates, although the results were not statistically significant [18]. Niraparib significantly prolonged median progression-free survival (24.8 *vs.* 8.3 months)[17]; however, benefits to overall survival have not been observed [19].

While these findings demonstrate the therapeutic potential of targeted therapies, their applicability is limited to tumors harbouring relevant molecular features. Importantly, these same molecular features also predict sensitivity to platinum-based chemotherapy. For example, PARP inhibitors exploit defects in homologous recombination repair pathways, which are strongly associated with platinum sensitivity [20]. Thus, PARP inhibitor clinical trials enrolled patients whose tumors responded to prior platinum-based chemotherapy [16,17]. Consequently, patients whose tumors fail to respond to platinum chemotherapy remain without targeted treatment options, highlighting platinum resistance as a major barrier to treating ovarian cancer.

Resistance to platinum-based chemotherapy continues to limit durable treatment responses in ovarian cancer. Platinum agents such as carboplatin and cisplatin exert cytotoxic effects by forming DNA crosslinks that disrupt DNA replication and transcription, resulting in cell death [21]. Tumor cells can evade these effects through several mechanisms, including enhanced DNA damage repair, reduced intracellular drug accumulation, and tolerance to DNA damage [22]. Approximately 20-30% of patients exhibit primary platinum resistance and fail to achieve responses to first-line chemotherapy [23]. Among those who initially respond, the majority ultimately experience disease recurrence; up to 75% of patients with advanced-stage disease relapse within 5 years [24,25], and 60-75% of recurrent tumors develop platinum resistance [26]. The emergence of platinum resistance substantially limits treatment options. Treatment with non-

platinum chemotherapies, such as paclitaxel or gemcitabine, typically result in progression-free survival durations of only 3-9 months [26,27]. Further, targeted therapies are most effective in platinum-sensitive tumors, limiting their applicability in platinum-resistant disease [20].

These therapeutic limitations reflect a plateau in treatment advancements for ovarian cancer, with therapeutic strategies remaining largely unchanged since the mid-1990s. Despite extensive investigation over the past several decades, few advances have translated into broadly applicable treatments with significant impacts on overall survival. Thus, there remains a need for innovative treatment strategies. Emerging research investigating immunotherapy for ovarian cancer is gaining momentum as a promising approach towards improvement of patient outcomes.

1.1.2 Immunotherapy for ovarian cancer

Immunotherapy involves manipulation of a patient's innate or adaptive immune responses to promote anti-tumor immune activity that destroys cancer cells. However, immunotherapies designed to stimulate anti-tumor immunity have produced limited clinical responses despite the evidence that immune cells are present within the ovarian tumor microenvironment (TME) [28,29]. This limited success is largely attributed to the immunosuppressive characteristics of ovarian carcinoma. Multiple mechanisms contribute to immune resistance in ovarian cancer, including bias towards regulatory T cells [30], T cell exhaustion [31], loss of tumor-specific antigens [32,33], and metabolic dysregulation of the TME [34–36]. Together, these mechanisms enable tumors to avoid immune destruction by limiting the survival, activation, and effector function of tumor-infiltrating lymphocytes (TILs), which play a critical role in anti-tumor immunity.

Presence of TILs within ovarian tumors is associated with improved survival and reduced relapse in ovarian cancer [28]. In particular, infiltration of CD8+ T cells within the tumor epithelium is associated with favourable outcomes [28]. However, the prognostic impact of TILs depends on the balance of T cell populations within the TME. Regulatory T cells (Tregs), which suppress effector T cell activation and proliferation, limit anti-tumor immune responses [37]. Accordingly, a high $CD8^+$/ Treg ratio within tumors is associated with improved prognosis [28], while increased Treg infiltration is associated with reduced survival in ovarian cancer [38]. In addition to suppression by Tregs, T cells within the ovarian TME frequently develop an exhausted phenotype characterized by expression of inhibitory receptors and impaired effector function [30,39]. Several factors contribute to the development of T cell exhaustion within tumors, including metabolic stress in the TME [40]. These observations reflect the ability of ovarian tumors to actively shape their local immune environment to promote immunosuppression. Together, these findings highlight a major challenge for ovarian cancer immunotherapy: effector T cells can be impaired by Tregs and T cell exhaustion.

An important mechanism contributing to T cell exhaustion in the TME is immune checkpoint signalling. Lymphocytes including CD4+ and CD8+ T cells, as well as peripheral B cells, express the inhibitory receptor programmed cell death protein 1 (PD-1). Engagement of PD-1 with programmed death-ligand 1 (PD-L1) induces inhibitory signalling that suppresses T cell activation and effector function [41]. In ovarian cancer, TILs frequently express inhibitory receptors, contributing to functional exhaustion [31]. Thus, immune checkpoint inhibitors that block PD-1/PD-L1 interactions have been investigated as a strategy to restore anti-tumor T cell activity. However, clinical responses to these therapies in ovarian cancer have been limited. For

example, a phase II clinical trial reported an objective response rate of approximately 8% for the checkpoint inhibitor pembrolizumab in patients with recurrent ovarian cancer [29]. These findings suggest that immune suppression within the ovarian TME is multifactorial and involves additional mechanisms that limit effective anti-tumor immune responses.

Another major challenge for anti-tumor immunity in ovarian cancer is loss of tumor-specific antigens required for T cell recognition. Activation of CD8+ T cells requires recognition of peptide antigens presented on human leukocyte antigen (HLA) class I molecules. Consequently, downregulation of HLA or defects in antigen-processing machinery can reduce T cell recognition of tumor cells. Loss of HLA class I expression has been associated with poor clinical outcomes in ovarian cancer [32]. Similarly, reduced expression of antigen-processing components has been linked to decreased TIL in ovarian tumors [33]. These observations illustrate how tumors evade immune detection by limiting antigen presentation.

Collectively, these findings demonstrate that immune suppression in ovarian cancer arises through multiple mechanisms that impair T cell function within the TME. Regulatory T cell activity, immune checkpoint signalling, and defects in antigen presentation all contribute to limiting anti-tumor immunity. However, these mechanisms do not fully explain how ovarian tumors establish immunosuppressive conditions within the local tumor environment. Increasing evidence suggests that metabolic dysregulation in the TME is a critical driver of immune suppression. Metabolic activity within tumors is spatially heterogeneous, leading to regional differences in nutrient availability, oxygen levels, and metabolite accumulation that influence immune cell function. However, the spatial organization and underlying mechanisms of these immunosuppressive metabolic environments remain poorly understood.

1.1.2.1 Metabolic dysregulation as a driver of immune suppression

Ovarian cancer, like many other cancers, reprograms its metabolism to promote tumor survival and evade immune destruction. Several metabolic pathways have been implicated in tumor-mediated immune suppression, including glucose and amino acid metabolism. Tumor glucose metabolism is characterized by enhanced glucose uptake *via* glucose transporter 1 (GLUT-1) [42] and increased glycolytic activity [43], resulting in rapid consumption of glucose by tumor cells. This metabolic shift can deplete glucose within the TME, restricting nutrient availability for TILs and impairing CD8+ T cell effector functions [44]. In addition, hypoxic tumor regions rely on glycolysis due to limited oxygen availability for oxidative phosphorylation. Hypoxia induces expression of carbonic anhydrase IX (CA9), an enzyme that facilitates pH regulation in the context of increased lactic acid production from glycolysis [45]. Together, lactate accumulation and CA9 activity promote extracellular acidification, which suppresses proliferation and cytokine production in CD8+ T cells [46].

Dysregulated amino acid metabolism also contributes to tumor immune suppression. Arginine metabolism plays a central role in regulating T cell function within the TME. Increased expression of arginase enzymes, which catalyze the conversion of arginine to ornithine, depletes arginine in the TME and impairs proliferation and T cell effector function [47]. Ornithine also serves as a precursor for polyamine synthesis (**Figure 1**), which has been shown to promote Treg differentiation and contribute to tumor immunosuppression [48]. Cysteine represents an additional metabolic constraint on T cell activity, as depletion of cystine in the TME restricts T cell proliferation and effector function [49]. Methionine metabolism represents another important

pathway regulating T cell function within the TME. Methionine is an essential amino acid involved in several cellular processes including methylation reactions, redox balance, and polyamine synthesis (**Figure 1**) [50]. Methionine serves as a precursor for S-adenosyl methionine (SAM), the primary methyl donor for histone methylation during T cell differentiation (**Figure 1**) [51]. However, elevated SAM levels are associated with epigenetic reprogramming that inhibits anti-tumor T cell functions [52]. Tumor cells commonly overexpress methionine transporter L-type amino acid transporter 4 (SLC43A2), resulting in methionine depletion and SAM accumulation that impairs T cell function [53]. Thus, methionine restriction has been identified as a potential strategy to alter tumor methionine metabolism and restore anti-tumor immune activity [54].

Figure 1. *Methionine cycle metabolic pathway.*

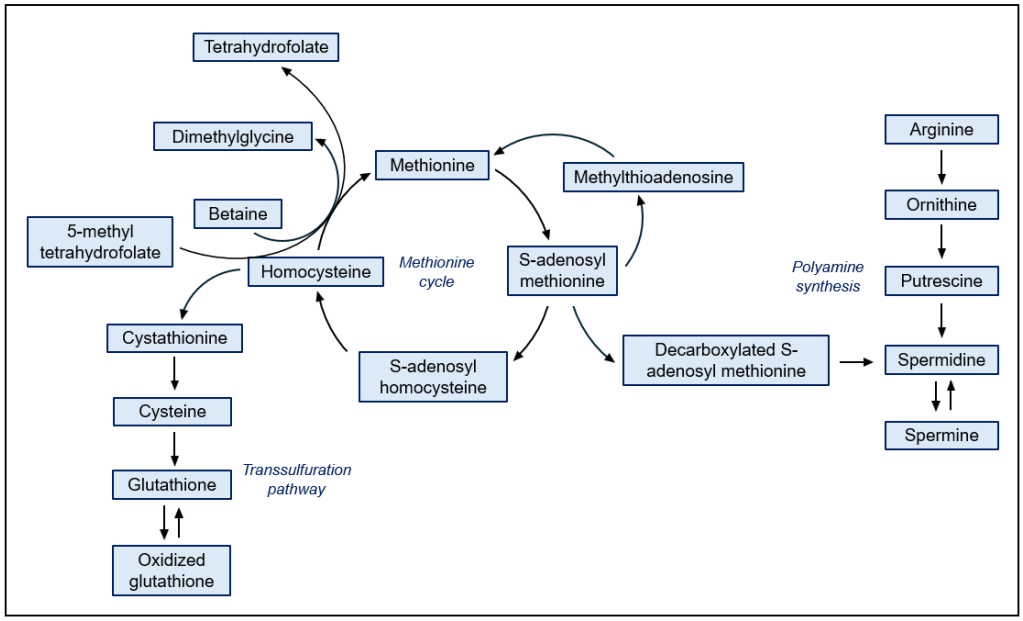

In addition to amino acid metabolism, metabolites involved in cellular redox metabolism may also influence anti-tumor immunity. Nicotinamide, a precursor for NAD^+ biosynthesis, supports T cell function and limits exhaustion [55].

Lipid metabolism also plays an important role in regulating immune activity within tumors. Lipids function as structural components of cellular membranes and as signalling molecules that influence immune cell behaviour. Arachidonic acid-containing phospholipids represent an important class of immune-relevant lipids within the TME. These lipids serve as membrane reservoirs for arachidonic acid, which can be released by phospholipase A2 and subsequently converted into inflammatory mediators including prostaglandins and leukotrienes [56]. These metabolites regulate multiple aspects of immune signalling. In particular, prostaglandin E2 suppresses $CD8^+$ T cell activation and cytotoxic function through cAMP-mediated signalling pathways [57]. Phosphatidylinositols (PIs) are another class of immune-relevant membrane lipids that serve as precursors for phosphoinositides involved in intracellular signalling. During T cell receptor engagement, phosphoinositide signalling cascades are activated, leading to downstream pathways that control T cell activation, proliferation, and effector function [58].

To conclude, ovarian cancer employs several major mechanisms to avoid immune destruction, creating significant barriers for development of effective immunotherapeutic treatments. Although many studies have identified individual pathways involved in tumor immune suppression, most approaches investigate these mechanisms in isolation without considering interactions within the complex TME. Techniques capable of interrogating spatial relationships between tumor cells, immune cells, and their surrounding metabolic environments are therefore essential for understanding how metabolic processes shape immune activity within tumors.

1.4 Mass spectrometry imaging

The metabolic landscape of solid tumors is spatially heterogeneous, with distinct niches defined by nutrient gradients and immune infiltration [59]. Analytical approaches that disrupt tissue morphology through homogenization obscure these localized metabolic variations and limit understanding of interactions between tumor cells, immune cells, and the TME. Mass spectrometry imaging (MSI) addresses this challenge by enabling spatially resolved detection of molecules directly within intact tissue sections. This label-free technique involves using an ionization source to release molecules from discrete regions of the tissue, with the resulting ions measured by a mass analyzer to determine their mass-to-charge ratio. Mass spectrometry experiments can be performed in positive or negative ion mode, which determines whether molecules are detected as positively or negatively charged ions and influences which molecular classes are most effectively observed. During MSI acquisition, ion abundances are measured sequentially cross the sample surface to generate spatially registered data. These data can then be reconstructed into ion images that enable visualization of the relative abundances of individual molecules while preserving tissue architecture. In contrast to conventional mass spectrometry approaches that require homogenization of solid samples, MSI enables spatially informed analysis of metabolites and other molecules within complex biological systems.

Multiple ionization strategies have been developed for MSI, each using distinct mechanisms to generate gas-phase ions from biological surfaces. Examples of ionization sources include matrix-assisted laser desorption/ ionization (MALDI)[60,61] and nanospray desorption electrospray ionization (nanoDESI) [62], which differ substantially in energy deposition and interactions with the sample surface. The ionization mechanism dictates the classes of molecules most efficiently

detected, as well as sample preparation requirements and achievable spatial resolution, defined as the smallest spatial feature that can be distinguished during analysis. In general, MALDI enables efficient ionization of larger and less polar molecules, while nanoDESI is well-suited for detection of small, polar molecules. The laser-based ionization mechanism of MALDI requires use of a chemical matrix to facilitate ion formation, while nanoDESI does not require matrix application. The focussed laser used for MALDI enables higher spatial resolution, whereas nanoDESI typically samples larger regions of tissue and consequently achieves lower spatial resolution. In addition to the ionization source, the analytical capabilities of an MSI platform are also determined by the type of mass analyzer used.

Ionization sources are coupled to mass analyzers, such as quadrupole time-of-flight (qTOF) or ion trap instruments, which determine mass resolution, sensitivity, and acquisition speed of mass spectrometric analyses. Mass resolution refers to the ability to distinguish molecules with similar mass-to-charge ratios, sensitivity reflects the ability to detect low-abundance molecules, and acquisition speed describes the rate at which mass spectra are collected during MSI experiments. Thus, the combination of ion source and mass analyzer configurations defines the analytical capabilities of an MSI platform and influences its suitability for specific molecular classes or biological questions. Different ionization sources and mass analyzers provide complementary advantages, which has motivated development of multimodal MSI workflows that integrate two or more MSI techniques and provide a more comprehensive molecular characterization of biological samples.

1.4.1 MALDI MSI

Matrix-assisted laser desorption/ ionization MSI involves the use of a laser to desorb and ionize molecules from the surface of a tissue. This technique enables molecular mapping of diverse molecular classes including proteins [61], peptides [63], lipids [64,65] glycans [66], and amino acids [67]. Detection of these molecular species largely depends on sample preparation and instrument settings including laser energy, ion polarity, and mass range. Sample preparation for MALDI MSI may include washing tissue sections with a solvent or chemical modification of molecules to improve detection sensitivity. This is followed by application of a chemical matrix required for laser-mediated desorption and ionization. After sample preparation, the mass spectrometer coupled to a MALDI ion source must be tuned to improve sensitivity of detection for the molecular classes of interest. Together, sample preparation and instrument parameters determine which molecular species can be efficiently detected in a MALDI MSI experiment.

1.4.2 Sample preparation for MALDI MSI

1.4.2.1 Applying washes to increase sensitivity of detection

Sample preparation plays a critical role in determining sensitivity and molecular coverage in MSI experiments, especially when analyzing low-abundance metabolites. Biological samples contain numerous molecules, including phospholipids, salts, and embedding materials, that ionize readily and can suppress detection of molecules of interest. Thus, washing tissue sections with solvents has emerged as a strategy to reduce chemical background and minimize ion suppression while preserving spatial localization of endogenous molecules.

Several organic solvents have been investigated for tissue washing with a goal of selectively removing interfering molecules based on differences in solubility. Selection of an appropriate solvent depends on the solubility of both ion-suppressive species and target analytes. For analytes sensitive to ion suppression by lipid ions, acetone is frequently used for its ability to efficiently remove lipids from tissues and improve sensitivity of detection for small molecule metabolites [68].

Alcohol-based washes, including methanol and ethanol, are similarly used to remove soluble salts and lipids [69,70]. Methanol has relatively high polarity, resulting in efficient extraction of polar metabolites and residual salts that contribute to ion suppression [69]. However, the high polarity of methanol can also increase solubility of endogenous metabolites, potentially resulting in analyte loss and delocalization during washing. Ethanol provides an intermediate polarity that can balance removal of interfering lipids with preservation of metabolites, and has been used in several studies to enhance peptide and metabolite detection [70,71].

In contrast to organic solvents, aqueous salt solutions are often used to selectively remove inorganic ions that contribute to adduct formation during ionization [72,73]. Solutions containing volatile ammonium salts, such as ammonium formate, exchange endogenous metal cations (*e.g.* sodium and potassium) with ammonium ions that rapidly evaporate under vacuum conditions. This exchange reduces formation of heterogeneous adducts, thus improving signal intensity for low-abundance molecular species [72,73].

Overall, tissue washing strategies provide opportunities to improve detection sensitivity in MSI experiments through selective removal of interfering compounds. However, solvent selection

must balance the removal of ion-suppressing species with the preservation of endogenous analytes and tissue morphology. Thus, careful selection of an appropriate organic solvent is essential for improving sensitivity of detection.

1.4.2.2 On-tissue chemical derivatization

Detection of metabolites by MALDI MSI is challenging due to several physicochemical and analytical limitations. Many metabolites are non-aromatic and highly polar, which can reduce their incorporation into matrix crystals and decrease ionization efficiency [74]. Additionally, the low *m/z* region of MALDI mass spectra is often dominated by matrix-derived ions and chemical background, which can obscure signals from low-mass metabolites [75]. Chemical derivatization addresses these limitations by modifying metabolites to increase molecular weight, introducing aromatic rings capable of more effective interactions with the MALDI matrix, and incorporating permanent charges that improve ionization efficiency.

Although derivatization has long been established in liquid chromatography mass spectrometry (LC-MS) workflows, adaptation of these methods for *in-situ* experiments has expanded the range of metabolites detectable with MSI analysis. On-tissue derivatization workflows typically involve selection of a reagent targeting specific functional groups on the molecule of interest, its application using an automatic sprayer, humidified incubation to promote reaction kinetics, and , matfor MALDI MSI [67,76]. Careful reagent selection, and optimization of solvent composition and incubation conditions is required to maximize reaction efficiency while preserving metabolite localization and tissue morphology [77].

Numerous derivatization agents have been described for use in MALDI MSI experiments. In this work, two reagents targeting primary amine or carboxylic acid functional groups were investigated, as these groups are commonly present in small molecule metabolites. The derivatization agent *N,N,N*-trimethylammonioanilyl hydroxysuccinimidyl carbamate iodide (TAHS) selectively reacts with primary amines through formation of stable carbamate linkages [76,78], while 4-(2-((4-bromophenethyl)-dimethylammonio)-ethoxy)-benzaminium dibromide (4-APEBA), activated with 1-ethyl-3-(3-dimethylaminopropyl)carbodiimide (EDC) targets carboxylic acids with carbodiimide-mediated coupling [79,80] (**Figure 2**). In both cases, the resulting metabolite derivatives feature predictable mass shifts corresponding to incorporation of the derivatization agent. This mass addition supports molecular annotations and reduces interferences from low-mass background ions (*e.g.*, matrix ions). Further, derivatization with both TAHS and 4-APEBA results in incorporation of a quaternary ammonium group with a permanent positive charge, improving ionization efficiency in positive polarity MSI experiments (**Figure 2**).

Figure 2. *Reaction schematics for derivatization with TAHS and 4-APEBA + EDC.*

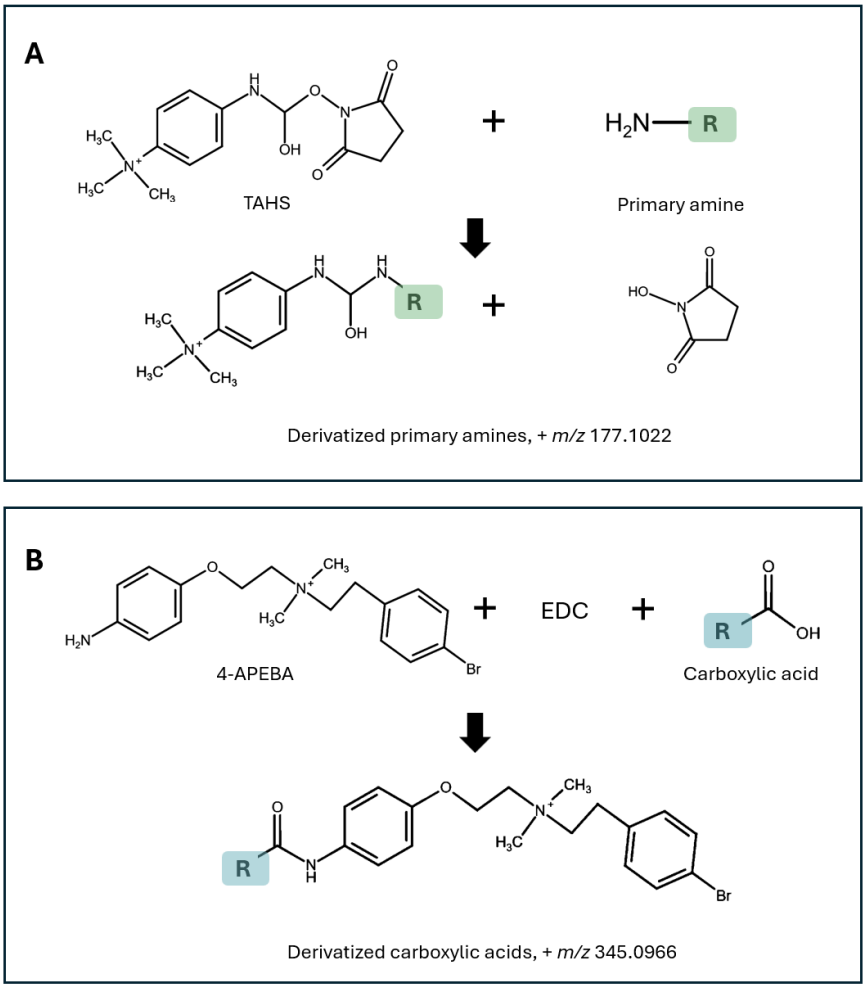

A. TAHS reacts with primary amines to form a derivatized product with a mass shift of + *m/z* 177.1022. **B.** 4-APEBA, activated with EDC, reacts with carboxylic acids to produce a derivative with a mass shift of + *m/z* 345.9066.

1.4.2.3 Chemical matrix

In addition to derivatization strategies, selection of an appropriate MALDI matrix also strongly influences ionization efficiency and analyte coverage. Application of chemical matrix is an essential step in sample preparation for MALDI MSI, enabling extraction and ionization of analytes from a complex sample. During application, soluble analytes migrate into matrix-containing droplets prior to solvent evaporation [74]. Subsequent co-crystallization immobilizes analytes and promotes optimal interactions with the MALDI laser. Most MALDI matrices are aromatic organic acids that strongly absorb ultraviolet laser energy, enabling controlled energy transfer to analytes during desorption while minimizing their fragmentation [81]. Through this process, matrix mediates conversion of solid-phase biomolecules into gas-phase ions suitable for detection *via* mass spectrometry.

Selection of an appropriate chemical matrix influences the range of detectable molecules in addition to data quality and reproducibility. Efficient analyte extraction requires compatibility between the solvent used for matrix deposition and the solubility of target analytes, as analytes must migrate into solvent droplets during application [74]. Solvent composition also influences evaporation during matrix deposition, which determines whether analytes remain in matrix-containing droplets long enough to permit formation of homogenous co-crystals [82]. Uniform crystal size and distribution are essential for maintaining spatial resolution and minimizing signal variability between laser shots [83]. Additionally, matrix-derived ions should not obscure analyte signals, particularly in the low *m/z* range where chemical background can reduce detection sensitivity of small molecules [75].

Selection of an appropriate chemical matrix for small molecule analysis is complicated by the extensive chemical diversity of these compounds. Matrix solvents compatible with one or a few target metabolites are unlikely to be compatible with all metabolites of interest. This leads to heterogeneous co-crystallization and molecule-dependent ionization efficiency [82]. Variation in functional groups among target molecules also influences their proton affinity, requiring matrices capable of supporting formation of either positive or negative ions depending on analyte chemistry.

Examples of matrices used for positive-ion detection of small molecules include 2,5-dyhydroxybenzoic acid (2,5-DHB)[84] and α-cyano-hydroxycinnamic acid (CHCA)[85], which provide efficient UV absorption and facilitate incorporation of small molecules into matrix crystals. More recently, 2,5-dihydroxyterephthalic acid (2,5-DHT) has been developed to enhance sensitivity of amino acid detection through improved extraction efficiency and reduced background interference in the low-mass range [86]. These matrices are readily soluble in polar organic solvents, facilitating extraction of hydrophilic metabolites during matrix deposition. For negative-ion detection of small molecule metabolites, matrices including 9-aminoacridine (9AA)[87], N-(1-napthyl)ethylenediamine dihydrochloride (NEDC)[88], and 1,5-diaminonapthalene hydrochloride (DAN-HCl)[89] are frequently employed, as they promote deprotonation of acidic metabolites while minimizing matrix-related interference.

Numerous matrices have also been optimized for lipid imaging by MALDI MSI, reflecting the structural diversity and proton affinity of lipid subclasses [90]. Comprehensive lipidomic analysis requires acquisition in both ion polarities to capture lipid species with different headgroup

chemistries; however, single-polarity experiments may provide sufficient molecular coverage depending on target lipid classes. In this work, lipid analyses were performed in negative ion mode for investigation of lipid classes including cardiolipins (CLs), phosphatidylethanolamines (PEs), phosphatidylinositols (PIs), and phosphatidylserines (PSs). To investigate these lipid classes, several matrices including as 2,5-dihydroxyacetophenone (2,5-DHA)[91] and norharmane [92] are commonly used due to their ability to efficiently extract and ionize acidic phospholipids from tissue surfaces. These matrices enable sensitive detection of lipid subclasses that readily undergo deprotonation, including those of interest in this work [91,92]. Beyond sample preparation parameters, instrumentation settings also play an important role in determining molecular coverage and data quality in MALDI MSI experiments.

1.4.3 Instrumentation for MALDI MSI

Mass spectrometry imaging instruments consist of an ionization source coupled to a mass analyzer. A MALDI ionization source employs a laser to generate gas-phase ions prior to mass analysis. In this work, ions were analyzed using a qTOF mass analyzer for MALDI MSI experiments. Laser-mediated ion generation is specific to MALDI, whereas other MSI modalities employ alternative ionization mechanisms.

1.4.3.1 Laser

In MALDI ionization, a pulsed ultraviolet laser is used to desorb and ionize crystals including matrix and analyte molecules. Each laser pulse deposits energy into the matrix, which absorbs the radiation and transfers energy into nearby analyte molecules, resulting in formation of gas-phase ions [81,82]. Several parameters of the laser can be adjusted to control this process, including

laser power, frequency, number of shots per pixel, and laser spot size. These settings collectively influence ion yield, spatial resolution, and data quality in MALDI MSI experiments.

Laser power represents the relative fraction of the maximum calibrated laser pulse energy delivered to the sample during each laser shot and is typically reported as a percentage rather than an absolute energy value. Increasing laser power can enhance molecule desorption and ionization, leading to higher signal intensity [93]. However, excessive laser energy can damage the tissue surface and promote fragmentation of molecules containing labile bonds [94]. Consequently, laser power must be empirically optimized to balance signal intensity while preserving molecular and sample integrity.

1.4.3.2 Mass detector

Following ionization with a MALDI ion source, ions are transferred into a mass analyzer where they are separated according to their mass-to-charge ratio (*m/z*). Several types of mass analyzers can be coupled to MALDI ion sources for imaging experiments, including time-of-flight (TOF), Orbitrap, and Fourier transform ion cyclotron resonance (FTICR) instruments. The present study employed a qTOF mass analyzer. Although Orbitrap and FTICR analyzers can achieve substantially higher mass resolution, qTOF instruments offer a balance between mass accuracy, resolving power, and acquisition speed.

In a qTOF instrument, ions first pass through a quadrupole mass filter, which can transmit ions across a broad *m/z* range or selectively isolate precursor ions for tandem mass spectrometry experiments [95]. In tandem mass spectrometry, selected precursor ions are fragmented in a

collision cell to generate product ions that provide structural information for molecular identification. Following quadrupole filtering, ions are accelerated into the time-of-flight analyzer by a high-voltage electric field, where their travel time through a flight tube of known length is measured [96]. Ions with different mass-to-charge ratios travel at different velocities, resulting in arrival times at the detector that can be used to determine their *m/z* [96]. However, many biologically relevant molecules remain difficult to resolve using *m/z* alone due to the presence of numerous isobaric and isomeric species.

1.4.3.3 Trapped ion mobility spectrometry

Instruments used for MALDI MSI can couple a qTOF mass analyzer with trapped ion mobility spectrometry (TIMS). Although qTOF analyzers provide accurate mass measurements with sufficient resolving power for many experiments, presence of isobaric species (molecules with very similar mass-to-charge ratios) and isomeric species (molecules with the same molecular formula but different structures) can create barriers to confident molecular annotations. To address this limitation, TIMS introduces an additional gas-phase separation prior to TOF detection [97,98]. In TIMS, ions are separated according to their mobility, providing an orthogonal dimension of separation that complements *m/z* measurements.

Within the TIMS cell, an inert carrier gas flow pushes ions against an electric field gradient. Ions are immobilized when the drag force generated by the gas flow is equal to the electric field force [99]. The electric field is then gradually reduced, allowing ions to elute from the TIMS cell according to their mobility. Ion mobility (K_i) is then determined from the velocity of the carrier gas (V_g) and the strength of the electric field when the ion elutes (E_x) [99]:

$$K_i = \frac{V_g}{E_x}$$

The collision cross section (CCS) of each ion can then be calculated from the measured mobility, providing information related to the rotationally averaged surface area of the ion [99]. The enhanced molecular specificity provided by TIMS enables insights into molecular heterogeneity within complex biological environments, where isomeric and isobaric species frequently co-localize [100]. Further, combined CCS and *m/z* measurements can be compared to database references to strengthen molecular annotations in comparison to assignments based on *m/z* alone [100]. While specific MALDI instrumentation, including TIMS, can improve molecular coverage, certain classes of small and highly polar metabolites remain challenging to detect using MALDI MSI workflows.

1.4.4 Nanospray desorption electrospray ionization MSI

Despite advances in MALDI MSI such as TIMS, detection of small and highly polar metabolites remains challenging due to matrix-derived background signals and variability in ionization efficiency. Nanospray desorption electrospray ionization mass spectrometry imaging (nanoDESI MSI) is an ambient ionization technique that enables spatially resolved detection of small molecules directly from tissue surfaces and provides complementary molecular coverage to MALDI MSI.

A nanoDESI ion source consists of two capillaries positioned at an angle relative to the tissue surface [101]. The primary capillary continuously delivers extraction solvent, forming a liquid

bridge between the capillary tip and the sample surface [101]. Endogenous molecules dissolve into the extraction solvent and are transferred into a secondary capillary that delivers extracted analytes to the mass spectrometer for electrospray ionization [101]. The capillaries raster across the sample surface, resulting in spatially resolved molecular information that can be reconstructed into ion images similarly to other MSI techniques [102].

To support the work described here, nanoDESI datasets were acquired by collaborators at Vancouver Island University. The instrument configuration included a nanoDESI ion source coupled to an Orbitrap mass analyzer, which provides high mass resolution and mass accuracy for confident annotation of small molecule metabolites. The electrospray-based ionization mechanism of nanoDESI favours detection of water-soluble metabolites, including amino acids, nucleotides, organic acids, and other intermediates involved in metabolic pathways [103]. Extraction efficiency and analyte coverage depend strongly on the composition of the extraction solvent. For detection of small molecule metabolites, mixtures of water and methanol are commonly employed to facilitate efficient extraction while maintaining stable electrospray conditions [103,104]. Together, MALDI MSI and nanoDESI provide complementary molecular coverage, motivating the development of multimodal imaging workflows that integrate these ionization strategies.

1.5 Multimodal mass spectrometry imaging

Conventional MSI workflows are typically optimized for detection of a single molecular class (*e.g.* small molecules, lipids, or proteins) given that sample preparation and data acquisition parameters favouring one class of analytes can suppress or obscure others. As no single MSI modality provides comprehensive coverage of the molecular landscape within complex tissues, combining them in a multimodal workflow circumvents their individual limitations.

Multimodal workflows enable investigators to integrate MSI approaches that differ in ionization mechanisms and molecular coverage. For example, desorption electrospray ionization (DESI) enhances detection of polar metabolites that are often suppressed in MALDI workflows, while MALDI enhances detection of lipids and other higher-mass analytes [105,106]. By integrating complementary MSI modalities such as MALDI and electrospray-based desorption ionization techniques (*e.g.* DESI or nanoDESI), multimodal imaging workflows can expand molecular coverage beyond what is achievable with a single imaging technique.

Protein detection can also be integrated into MALDI MSI workflows using MALDI immunohistochemistry (MALDI IHC)[107,108]. This approach involves use of antibodies conjugated to photocleavable mass tags (PC-MTs™) that are released prior to MALDI ionization and detected as reporter ions [107]. This approach enables multiplexed detection of targeted proteins and is compatible with prior MALDI MSI experiments performed on the same tissue section [107,108].

Mass spectrometry imaging techniques can also be combined with microscopy techniques that provide morphological or cellular context. Antibody-based immunofluorescence imaging enables visualization of specific protein markers that are not directly detectable by MSI or MALDI IHC [109]. When performed on serial tissue sections, immunofluorescence allows spatial comparisons between molecular distributions visualized with MSI and patterns of protein expression, such as immune cell markers. By targeting proteins that are not detectable by MSI, immunofluorescence enables investigation of spatial relationships between immune markers and metabolite distributions.

While multimodal imaging approaches expand molecular coverage and biological insight, practical challenges complicate development of robust workflows. Many imaging techniques are irreversible or damage the tissue surface, requiring multimodal experiments to be performed on serial tissue sections. However, serial sections often exhibit small morphological differences resulting from biological variation or distortions introduced during cryosectioning. These discrepancies can reduce confidence in co-localization analyses, especially when studying microanatomical features. Performing multiple imaging experiments on the same tissue section can minimize alignment errors and preserve true molecular co-localization. Consequently, use of serial sections or a single tissue section ultimately depends on the biological question being addressed. Studies investigating spatial correlations between large tissue regions may tolerate minor differences between sections, while experiments aimed at correlating molecular distributions within microscopic features may require imaging of the same tissue section to preserve spatial fidelity.

Overall, multimodal imaging workflows provide an opportunity to investigate complex biological samples. This approach may yield new insights into heterogeneous ovarian tumors, where metabolic activity, lipid signalling, and immune cell interactions occur within distinct spatial niches. In ovarian cancer, metabolic adaptations in tumor cells contribute to immune suppression and resistance to immunotherapy, yet many studies fail to consider interactions between these pathways within the spatial organization of tumor tissues. Thus, multimodal imaging approaches provide an important strategy for integrating molecular information obtained from intact tissue sections.

In the present work, complementary imaging modalities were integrated to investigate metabolic heterogeneity within tumors. Mass spectrometry imaging approaches enabled analysis of metabolites, lipids, and proteins in tumor tissues. These workflows were applied in mouse tumor models and human ovarian cancer samples to examine relationships between tumor metabolism and T cell infiltration within the tumor microenvironment.

Hypothesis & Objectives

Hypothesis

Improved spatial detection of metabolites combined with multimodal imaging workflows will reveal spatial relationships between immune cells and regions of metabolic dysregulation within tumors, providing insight into metabolic mechanisms contributing to tumor immunosuppression.

Aim 1

Optimize MALDI mass spectrometry imaging workflows for spatial detection of methionine cycle metabolites in tumor tissues.

Aim 2

Develop and apply a multimodal mass spectrometry imaging workflow integrating metabolite, lipid, and protein imaging to investigate metabolic effects of dietary methionine restriction and their spatial associations with T cells in tumor tissues.

Aim 3

Apply multimodal imaging to human ovarian cancer tissues to determine how metabolic heterogeneity relates to T cell infiltration within the tumor microenvironment.

Chapter 2: Optimizing MALDI MSI methods for detection of methionine cycle metabolites

2.0 My contributions

Madison Shiyuk performed all MALDI MSI-related experiments and data analysis. Cell culture and animal experiments were performed by Dr. Tian Zhao (BC Cancer, Victoria, BC). The derivatization reagent 4-APEBA was provided by Dr. Kevin Zemaitis (Pacific Northwest National Laboratory, WA, USA).

2.1 Chapter Introduction

Metabolic dysregulation in the TME contributes to tumor-mediated immune suppression that impairs T cell activation and effector function. These metabolic constraints have important implications for development of immunotherapeutic strategies for ovarian cancer. Among the pathways required for anti-tumor immunity, methionine metabolism plays a central role in T cell differentiation, expansion, and effector function [51,52]. Cancer cells can outcompete T cells for methionine, limiting methyl donor availability and suppressing T cell responses [53]. Although methionine metabolism recognized as an important regulator of anti-tumor immunity, how metabolite levels vary within tumors and relate to immune cell infiltration remains unclear.

Tumors consist of subclonal populations of cells that acquire distinct genetic mutations over time and include stromal and immune cells, giving rise to localized metabolic niches within the TME [59]. Variations in nutrient availability and metabolic pathway activity across these regions shape interactions between tumor and immune cells. Mass spectrometry imaging offers a strategy to

investigate these spatial metabolic patterns; however, detection of small, polar metabolites associated with methionine metabolism remains challenging using conventional MALDI MSI workflows.

Consistent with these analytical challenges, previous MALDI MSI studies have detected only a limited subset of methionine metabolites, and comprehensive coverage of this pathway has not been achieved [76,110,111]. Therefore, targeted optimization of MALDI MSI workflows is required to improve coverage of methionine cycle metabolites and enable investigation of metabolic heterogeneity in tumors.

Multiple components of the MALDI MSI workflow influence metabolite detection. Metabolites containing labile bonds are susceptible to in-source decay, requiring laser power optimization to prevent fragmentation [94]. Chemical matrix selection determines ionization efficiency and background interference from matrix ions [74]. Solvent washing prior to matrix application can reduce ion suppression by removing lipids and salts that compete with target metabolites for ionization [68–73]. On-tissue chemical derivatization can enhance detection of poorly ionizable species through targeted chemical modification [76,78–80]. Systematic optimization of these parameters is essential for maximizing coverage of methionine metabolites.

In this chapter, these strategies were evaluated to establish an optimized MALDI MSI workflow for spatial mapping of metabolites involved in methionine cycle metabolism in a murine tumor model. Development of this method provides a foundation for subsequent investigation of relationships between these metabolic pathways and tumor-infiltrating lymphocytes.

Chapter 2.2 Methods

2.2.1 Cell cultures

2.2.1.1 EG7-OVA tumor cells

Lymphoma tumor cells from the EG7-OVA cell line (American Type Culture Collection [ATCC], Cat. No. CRL-2113) were cultured in ATCC-modified Roswell Park Memorial Institute (RPMI) medium (Gibco, Cat. No. A1049101) supplemented with 10% fetal bovine serum (Hyclone, Cat. No. SH30396.03HI), 50 µM β-mercaptoethanol (Sigma Aldrich, Cat. No. M3148-100ML), 1% penicillin/streptomycin (Hyclone, Cat. No. SV30010), 2 mM L-glutamine (Hyclone, Cat. No. SH3003401), and 400µg/ mL of geneticin (G418; Gibco, Cat. No. 10131-035). Cells were maintained at 37 °C and 5 % CO_2 in a humidified CO2 incubator (Thermo Fisher Scientific) and used at passage numbers 20.

2.2.1.2 $CD8^+$ T cells

Primary mouse $CD8^+$ T cells were isolated from OT-1 mouse spleens. Splenocytes were obtained by mechanically dissociating spleens through a 40 µm cell strainer (Falcon, Cat. No. C352340) into phosphate-buffered saline (PBS; Gibco, Cat. No. 0010023). Red blood cells were lysed using 1 mL ammonium-chloride-potassium (ACK) lysing buffer (Gibco, Cat. No. A1049201) for one minute at room temperature. Cells were washed in PBS, filtered through a 40 µm cell strainer, and $CD8^+$ T cells were isolated using an EasySep™ Mouse CD8+ T cell Isolation Kit (StemCell Technologies, Cat. No. 19853) according to the manufacturer's instructions. Isolated $CD8^+$ T cells were cultured in RPMI medium (Hyclone, Cat. No. SH30255) with 10% fetal bovine serum (Hyclone, Cat. No. SH30396), 50 µM β-mercaptoethanol (Sigma-Aldrich,

Cat. No. M3148), 1% penicillin/ streptomycin (Hyclone, Cat. No. SV30010), 2 mM L-glutamine (Hyclone, Cat. No. H3003401), and 50 U/mL recombinant mouse IL-2 (PeproTech, Cat. No. AF-212-12-100UG). For T cell activation, 96-well plates were pre-coated with anti-CD3 (Biolegend, Cat. No. 100202) and anti-CD28 (Invitrogen, Cat. No. 14-0289-82) antibodies for 2 hours at 37°C. Isolated $CD8^+$ T cells were seeded at 1 x 10^6 cells/ well and incubated in a humidified CO_2 incubator (Thermo Fisher Scientific) at 37°C and 5% CO_2 for 2 days.

2.2.2 Animal studies

All animal studies were approved by the University of Victoria's Animal Care Committee (AUP #2023-019(3)) and conducted in accordance with Canadian Council for Animal Care guidelines. Animal studies were performed with assistance from the Animal Care Service at the University of Victoria as a paid service.

Female B6 Thy 1.1 mice (Jackson Laboratory, Strain No. 00406; RRID: IMSR_JAX:00406) were housed in groups at 22°C with a 12-hour light-dark cycle. At four months of age, mice were randomized by body weight and subcutaneously injected with 1 x 10^6 EG7-OVA tumor cells. Tumor volumes were measured twice weekly using digital calipers (Thermo Fisher Scientific, Cat. No. 06-664-16) and calculated as tumor volume = length x width x width / 2. Mice were euthanized when the tumor volume was greater than 1500 mm^3 or bodyweight loss exceeded 20%.Tumors were harvested, embedded in 2% carboxymethylcellulose (CMC; Fisher Scientific, Cat. No. ICN15056090), snap-frozen in liquid nitrogen vapor, and stored at -80°C.

2.2.3 Cryosectioning

Tissues were mounted onto a cryostat chuck using optimal cutting temperature (OCT) mounting medium (Thermo Fisher Scientific, Cat. No. 4585) and sectioned at 10 µm thickness using a CM1950 cryostat (Leica Biosystems) and a C25 microtome blade (Feather, Cat. No. 24070549). The chamber and sectioning head temperatures were maintained at -15°C and -16°C, respectively. Serial sections were thaw-mounted onto indium-tin oxide (ITO)-coated glass slides (Delta Technologies, Cat. No. CB- 901N-S111) for 2-3 minutes, then placed in a nitrogen desiccator cabinet for 1 hour. Slides were sealed with ParaFilm (Thermo Fisher Scientific, Cat. No. PM992) and stored at -80°C. Prior to sample preparation and MSI analysis, tissue sections were equilibrated to room temperature for 1 hour in a nitrogen desiccator.

2.2.4 Tissue washes

Methanol (Thermo Fisher Scientific; Cat. No. A4564), ethanol (Commercial Alcohols, Cat. No. P016EAAN), acetone (Thermo Fisher Scientific, Cat. No. A9294), and 150 µM ammonium formate (Sigma Aldrich, Cat. No. AC168615000) were pre-cooled to -20°C in glass Coplin jars. When needed, slides were fully submerged in the selected solvent for 2 minutes, followed by vacuum drying for 10 minutes.

2.2.5 Chemical standards

Metabolite chemical standards (Sigma Aldrich) were spotted onto slides adjacent to tissue sections at 10 µM concentration: arginine (Cat. No. A5131), betaine (Cat. No. 61962), cysteine (Cat. No. 30089), cystathionine (Cat. No. C7505), dimethylglycine (Cat. No. D6382),

glutathione (GSH; Cat. No. G4251), oxidized glutathione (Cat. No. G4376), homocysteine (Cat. No. 44925), methionine (Cat. No. 64319), MTA (Cat. No. D5011), ornithine (Cat. No O5250), putrescine (Cat. No. 32810), S-adenosyl methionine (SAM; Cat. No. A4208), S-adenosyl homocysteine (SAH; Cat. No. A9384), spermidine (Cat. No. S2626), spermine (Cat. No. 85605), tetrahydrofolate (Cat. No. T3125), and 5-methyltetrahydrofolate (Cat. No. M0132). Standards were vacuum-dried for 10 minutes prior to on-tissue derivatization or chemical matrix application.

2.2.6 On-tissue chemical derivatization

For on-tissue derivatization with TAHS (Toronto Research Chemicals Cat. No. T210505), the reagent was applied to tissue sections when appropriate using an HTX M5 Sprayer (HTX Technologies). Reagent concentrations, solvent composition, and application parameters are provided in **Supplementary Table 1.** Slides were incubated 60°C in a humidified chamber for 18 h, followed by drying for 10 minutes in a nitrogen desiccator cabinet prior to matrix deposition (2,5-DHB; **Chapter 2.2.7**).

The derivatization agent 4-APEBA was synthesized at the Pacific Northwest National Laboratory as previously described [112] and was kindly provided by Dr. Kevin J. Zemaitis. When needed, solutions of EDC (Sigma Aldrich, Cat. No. E6383) and 4-APEBA were deposited onto tissues using an HTX M5 sprayer (parameters outlined in **Supplementary Table 1**). The EDC solution was applied immediately before 4-APEBA, and slides were incubated for 5 minutes at room temperature prior to 2,5-DHB matrix application (**Chapter 2.2.7**).

2.2.7 Chemical matrix application

Matrix solutions of 2,5-DHB (Sigma Aldrich, Cat. No. 149357), CHCA (Sigma Aldrich, Cat. No. C2020), 2,5-DHT (Sigma Aldrich, Cat. No. D107603), NEDC (Sigma Aldrich, Cat. No. 222488), 9AA (Sigma Aldrich, Cat. No. 92817), and DAN-HCl (Tokyo Chemical Industry, Cat. No. D5689) were applied using an HTX M5 sprayer (HTX Technologies) coupled to an external syringe pump (Harvard Apparatus). Solvents composition and application parameters are provided in **Supplementary Table 1**.

2.2.8 MALDI mass spectrometry imaging

2.2.8.1 MALDI MSI of underivatized tissues

All tissues were imaged using a timsTOF *flex* MALDI-2 instrument (Bruker Daltonics) in the mass range *m/z* 60-650 and a 50 µm step size. Slides coated with 2,5-DHB, CHCA, and 2,5-DHT were analyzed in positive ion mode, while slides coated with NEDC, 9AA, or DAN-HCl were analyzed in negative ion mode.

Custom SmartBeam (Bruker) laser settings were used: 500 shots per pixel, 10 000 Hz frequency, and 5.0 µs post-ionization delay. The following settings were tuned to maximize transmission in the low mass range: funnel RF amplitudes (funnel 1: 125 Vpp, funnel 2: 200 Vpp, multipole: 200 Vpp), collision cell voltage (5.0 eV), collision RF (350 Vpp), quadrupole ion energy (5.0 eV), and pre-TOF focus (35.0 µs transfer time; 3.5 µs pre-pulse storage). External mass calibration was performed prior to data acquisition using an ESI-L low concentration tuning mix (Agilent Technologies, Cat. No. G1969-85000). Online calibration was performed during data acquisition

using high-abundance metabolite species as reference ions. In positive ion mode, taurine (*m/z* 126.0225), C16:1 (*m/z* 255.2324), C16:0 (*m/z* 257.2481), C18:2 (*m/z* 281.2481), C18:1 (*m/z* 283.2638), and C18:0 (*m/z* 285.2794) were used as reference ions. In negative ion mode, the corresponding deprotonated ions of these molecules were used: taurine (*m/z* 124.0068), C16:1 (*m/z* 253.2168), C16:0 (*m/z* 255.2324), C18:2 (*m/z* 279.2324), C18:1 (*m/z* 281.2481), and C18:0 (*m/z* 283.2637).

2.2.8.2 MALDI MSI of derivatized tissues

Following on-tissue chemical derivatization (**Chapter 2.2.6**) and matrix application (**Chapter 2.2.7**), instrument tuning was adjusted to maximize detection of derivatized metabolites over the mass range *m/z* 80-700. Acquisition parameters were identical to those described in **Chapter 2.2.8.1**, except for the following: collision cell voltage (10.0 eV), collision RF (700 Vpp) and pre-TOF focus (65.0 µs transfer time; 6.0 µs pre-pulse storage).Matrix-derived ions from 2,5-DHB were for online calibration during acquisition (*m/z* 137.0223, *m/z* 155.0339, *m/z* 273.0394, and *m/z* 409.0554).

2.2.8.3 Laser power optimization

Chemical standards for S-adenosyl methionine, S-adenosyl homocysteine, and glutathione were analyzed in positive ion mode using the instrument settings described in **Chapter 2.2.8.1**, with laser power varied from 25% to 85% (25%. 35%, 45%, 55%, 65%, 75%, and 85%)

2.2.9 Post-MALDI MSI H&E staining

After imaging, the 2,5-DHB matrix was removed by two 3-minute washes in 70% acetonitrile at 4ºC. Next, tissue sections were fixed in 10% neutral buffered formalin (Sigma Aldrich, Cat. No. HT501128) for 30 minutes. Tissues were then rehydrated in a graded ethanol series: 100% ethanol (2 washes for 2 minutes each), then 90%, 70%, and 50% ethanol for 3 minutes each. Slides were washed for 2 minutes in LC-MS water (Thermo Fisher Scientific, Cat. No. W6-4) and stained with Gill's hematoxylin No. 2 (Sigma Aldrich, Cat. No. GHS216) for 4 minutes. Excess stain was removed with two rounds of three slow dips in LC-MS water, followed by differentiation in Scott's Modified Tap Water Substitute (0.2% w/v sodium bicarbonate [Sigma Aldrich, Cat. No. S6014] + 2% w/v magnesium sulfate [Sigma Aldrich, Cat. No. 208094] in LC-MS water) for 30 seconds. Tissues were then counterstained with Eosin Y (2.5 % w/v in 80% ethanol with 0.5% acetic acid; Sigma Aldrich, Cat. No. E4009; acetic acid: Anachemia, Cat. No. 00598-463), then dehydrated in an ethanol series (70%, 80%, 90%, 100%, 100%; 2 minutes each) and cleared in xylenes (Sigma Aldrich, Cat. No. 1330-20-7) for 2 minutes. Slides were air-dried and coverslipped using Permount™ mounting medium (Thermo Fisher Scientific, Cat. No. SP15-100) and glass coverslips (Fisher Scientific, Cat. No. 22-266882). Brightfield optical images were obtained at 4x magnification using a PathScan Enabler 5 (Meyer Instruments).

2.2.10 Data analysis

Data were analyzed using SCiLS Lab™ (version 2026b; Bruker) with intensity signals normalized to total ion current (TIC). For analysis of chemical standards detected across varying laser powers, signal intensities were normalized to root mean square (RMS). Metabolite identities were putatively assigned based on accurate mass measurements and comparison with

chemical standards. Mean signal intensities were exported for 19 methionine cycle metabolites (**Supplementary Table 2**). Metabolite signals were filtered by using a signal-to-noise ratio, calculated by dividing metabolite intensity by the corresponding signal from matrix and embedding medium for each tumor. A small pseudocount (0.01) was added to background intensities to prevent division artifacts. Metabolites were retained if they met a signal-to-noise ratio of ≥3:1. Retained metabolite signals were visualized using GraphPad Prism (version 11.0.0[84]).

2.3 Results

2.3.1 Laser power optimization

Several MALDI laser parameters, including frequency and number of shots per pixel, influence signal intensity and molecule fragmentation. Laser power was selected for systematic optimization as it directly controls energy deposition during ionization and strongly influences fragmentation. Laser power also fluctuates over time due to factors such as instrument maintenance and routine use and therefore requires periodic monitoring to maintain consistent performance. This is particularly important for methionine cycle metabolites, as several targets generate fragments with the same mass-to-charge ratio as other metabolites of interest. Specifically, SAM, SAH, and GSH produce fragments with the same structures as methionine, homocysteine, and cysteine, respectively (**Figure 3A-C**).

To assess the effect of laser power on fragmentation of SAM, SAH, and GSH, chemical standards of these metabolites were analyzed using 2,5-DHB across laser powers from 25% to 85%. Signal intensities of intact metabolites and metabolite fragments were compared with each laser power (**Figure 3D & E**). For all three metabolites, signal intensities increased when laser power was increased from 25% to 55%, reaching a maximum at 55% (**Figure 3D**). Signal intensities then declined at higher laser powers, with SAM exhibiting the most rapid decrease (**Figure 3D**). Fragment ion intensities increased in relative abundance between 35% and 65% laser power, peaking at 65%, and decreased at higher laser powers (**Figure 3E**). Fragments of SAM and SAH showed greater relative increases than those from GSH, indicating higher susceptibility to in-source decay (**Figure 3E**).

At 55% laser power, intact metabolite signals were highest while fragment ion intensities remained relatively low (**Figure 3D & E**), with intact metabolite signal intensities approximately 40-fold higher than fragment signals (**Figure 3D & E**). Based on these measurements, 55% laser power was selected for subsequent imaging experiments using 2,5-DHB.

Figure 3. *Laser power-dependent changes in signal intensity and fragmentation of SAM, SAH, and GSH.*

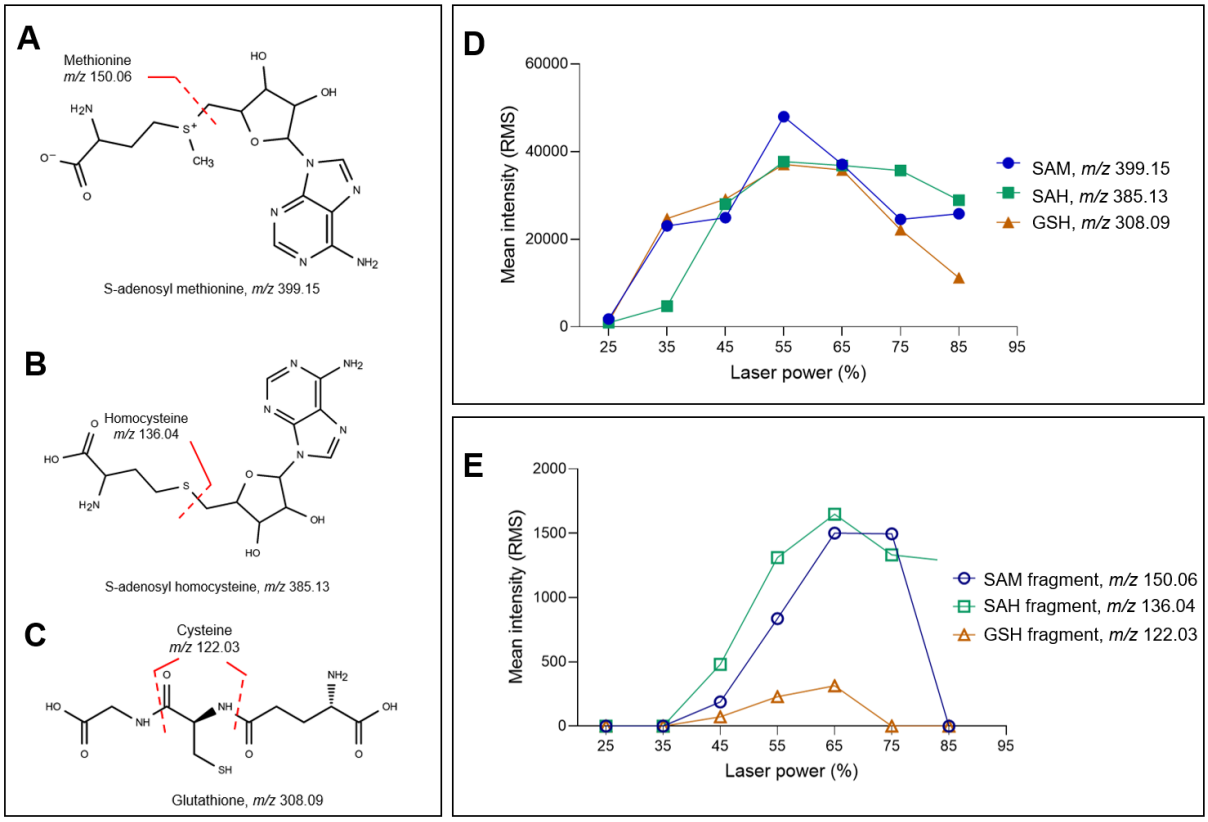

A-C. Chemical structures of (**A**) SAM, (**B**) SAH, and (**C**) GSH with fragment ions of the same *m/z* as methionine, homocysteine, and cysteine shown. **D-E.** Signal intensities of chemical standards corresponding to (**D**) intact SAM, SAH and GSH, or (**E**) fragments of SAM, SAH, and GSH across a range of MALDI laser power settings. Data were normalized to RMS prior to analysis.

2.3.2 Optimizing chemical matrix selection

Six chemical matrices were evaluated to achieve maximal coverage of methionine cycle metabolites (**Figure 1**) within a single MALDI MSI experiment. Serial tissue sections were used to facilitate comparisons between sample preparation conditions. Given that several target metabolites were predicted to ionize preferentially in positive or negative ion polarity, three matrices were assessed in each ion mode.

In positive ion polarity, the matrix 2,5-DHB resulted in the highest coverage of methionine cycle metabolites (4/19; **Table 1**). Use of CHCA or 2,5-DHT did not enable detection of any metabolites that were not also detected with 2,5-DHB (**Table 1**). In negative ion mode, both DAN-HCl and 9AA resulted in detection of 3/19 methionine cycle metabolites (**Table 1**). Across all matrices, 7 unique metabolites were detected, and the highest coverage achieved with a single method was 4/19 metabolites (2,5-DHB; **Table 1**). To further improve metabolite coverage, solvent washing was investigated.

Table 1*. Coverage of methionine cycle metabolites using six different MALDI matrices.*

Matrix	Coverage in positive ion mode	Coverage in negative ion mode
2,5-DHB	Arginine, GSH, MTA, and SAM (4/19)	N/A
CHCA	Arginine, MTA, and SAM (3/19)	N/A
2,5-DHT	Arginine (1/19)	N/A
NEDC	N/A	GSH (1/19)
DAN-HCl	N/A	GSH, ornithine, and SAH (3/19)
9AA	N/A	GSH, GSSG, and MTA (3/19)

Methionine cycle metabolites detected with MALDI MSI using 2,5-DHB, CHCA or 2,5-DHT matrices in positive ion mode and NEDC, DAN-HCl, or 9AA matrices in negative ion mode. Metabolite identities were putatively assigned based on accurate mass measurements and comparison with chemical standards. Only metabolites with a signal-to-noise ratio ≥3 were retained.

2.3.3 Solvent washing

To evaluate the impact of solvent washing on metabolite detection, four solvents of increasing polarity (acetone, ethanol, methanol, and ammonium formate) were applied prior to matrix deposition. Based on results from **Chapter 2.3.1**, analyses were performed in positive ion mode using 2,5-DHB, which provided the greatest metabolite coverage. Unwashed tissue served as a negative control.

Washing with acetone, methanol, ethanol, or ammonium formate resulted in detection of 3, 3, 4, and 0 metabolites, respectively (**Figure 4A**). Acetone and ethanol enabled detection of betaine, which was not observed in the unwashed tissue (**Figure 4C**). Similarly, washing with methanol or ethanol resulted in detection of ornithine, which was not detectable without washing (**Figure 4F**). In contrast, MTA and SAM, detected in unwashed tissue, were not observed following any of the solvent washes (**Figure 4E & G**). Ammonium formate washing did not result in detection of any target metabolites (**Figure 4A**).

Overall, solvent washing enabled detection of two additional metabolites (betaine and ornithine; **Figure 4C & F**) but did not increase total coverage beyond four of nineteen target metabolites under any single condition (**Figure 4A**). On-tissue chemical derivatization was therefore evaluated to further enhance metabolite detection.

Figure 4. *Coverage and signal intensities of methionine cycle metabolites following tissue washes.*

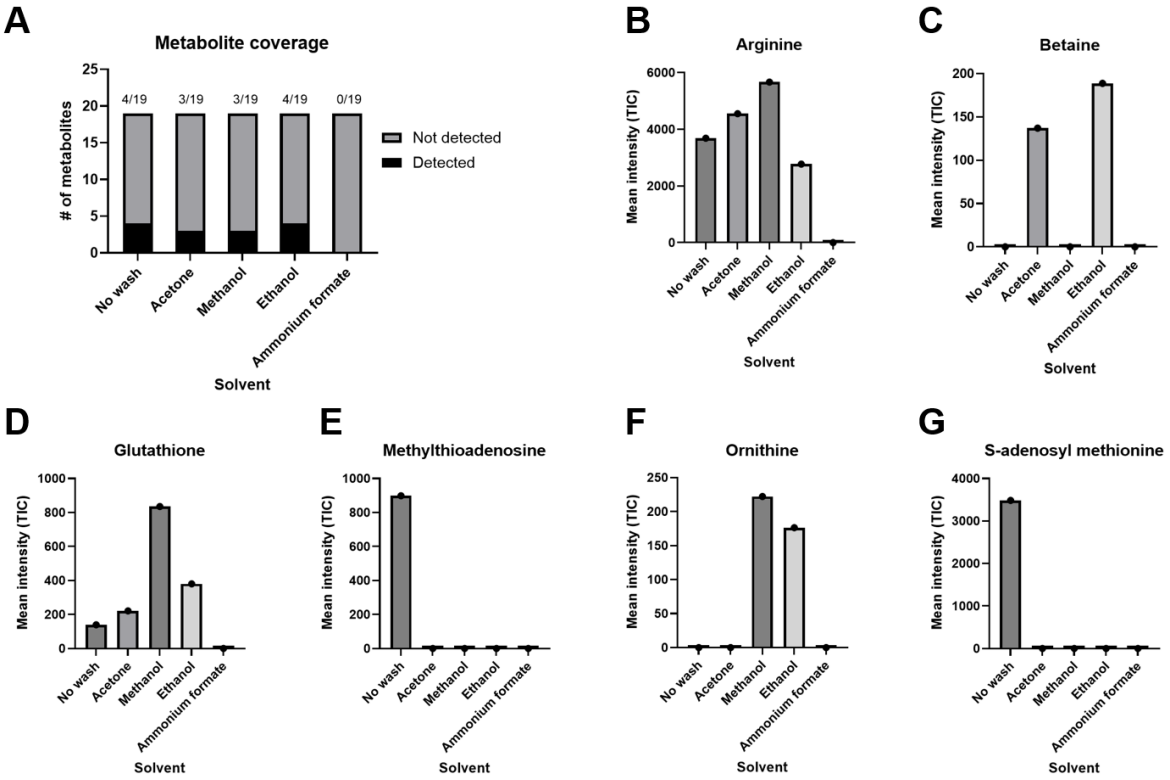

A. Coverage of methionine cycle metabolites detected in tissues subjected to no wash or washes with acetone, methanol, ethanol, or ammonium formate. All tissues were imaged in positive ion polarity with 2,5-DHB as a matrix. **B-G.** Mean intensities (normalized to TIC) of metabolites detected under each wash condition. Metabolite identities were putatively assigned based on accurate mass measurements and comparison with chemical standards. Only metabolites exceeding a signal-to-noise ratio ≥3 were retained.

2.3.4 On-tissue chemical derivatization

To determine the effect of on-tissue derivatization on methionine cycle metabolite detection, derivatization with 4-APEBA + EDC or TAHS was investigated. Chemical standards were applied beside each tissue section to serve as a positive control, and an underivatized tissue section was used as a negative control. Serial tissue sections were used to facilitate comparisons of metabolite signal intensities.

Derivatization with 4-APEBA + EDC did not improve metabolite coverage in comparison to the underivatized condition (**Table 2**). In contrast, derivatization with TAHS increased coverage of methionine cycle metabolites to 12 of 19 metabolites (**Table 2**). Eight metabolites were uniquely detected following TAHS derivatization: cystathionine, cysteine, GSSG, homocysteine, ornithine, putrescine, spermidine, and spermine (**Table 2**).

Tissue sections derivatized with 4-APEBA + EDC exhibited visible cracking in ion images and post-imaging hematoxylin and eosin (H&E) staining (**Figure 5B**). This was not observed in underivatized or TAHS-derivatized tissues (**Figure 5A & C**). Tissues derivatized with TAHS also showed increased basophilia in H&E staining (**Figure 5A & C**).

Overall, on-tissue derivatization with TAHS provided the highest coverage of methionine cycle metabolites among the conditions evaluated (12/19 metabolites) and preserved tissue integrity throughout MALDI MSI and subsequent histology staining (**Table 2; Figure 5C**).

Table 2. *Coverage of methionine cycle metabolites following on-tissue chemical derivatization.*

Derivatization agent	Metabolite coverage
Underivatized control	Arginine, GSH, MTA, and SAM (4/19)
4-APEBA + EDC	Arginine, GSH, methionine, and SAH (4/19)
TAHS	Arginine, cystathionine, cysteine, GSH, GSSG, homocysteine, methionine, ornithine, putrescine, SAH, spermidine, and spermine (12/19)

Methionine cycle metabolites detected without derivatization, following derivatization with 4-APEBA + EDC, or following derivatization with TAHS. All tissues were imaged in positive ion mode using 2,5-DHB matrix. Metabolites were putatively assigned based on accurate mass measurements and comparison with chemical standards analyzed under identical conditions. Only metabolites exceeding a signal-to-noise ratio ≥3 were retained.

Figure 5. *Ion images and H&E stains following on-tissue chemical derivatization.*

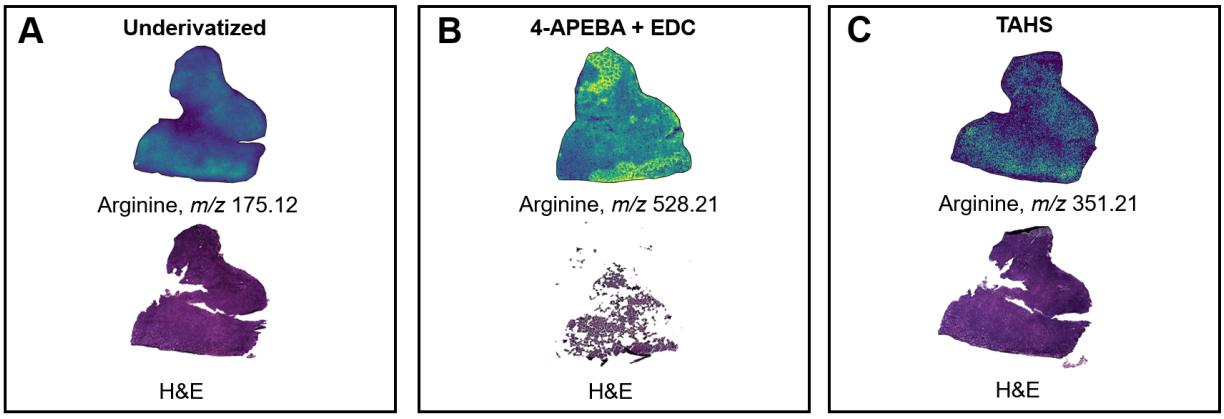

Ion images of arginine detected (**A**) without derivatization, (**B**) following derivatization with 4-APEBA + EDC, or (**C**) following derivatization with TAHS. All tissues were imaged in positive ion mode using 2,5-DHB matrix, and metabolite identities were assigned using accurate mass measurements and comparison to chemical standards. Tissues were subjected to hematoxylin and eosin (H&E) staining after MALDI MSI analysis, and optical images are shown for stained tissues following (**A**) no derivatization, (**B**) derivatization with 4-APEBA + EDC, or (**C**) derivatization with TAHS are shown.

2.4 Chapter Discussion

The primary objective of this chapter was to optimize a MALDI MSI workflow for detection of methionine cycle metabolites (**Figure 1**). Laser power, matrix selection, solvent washing, and derivatization strategies were systematically evaluated to improve metabolite coverage while preserving tissue integrity.

In-source fragmentation was a key consideration. S-adenosyl methionine and SAH exhibited greater fragmentation than GSH with increasing laser power, likely due to labile glycosidic bonds compared to more stable amide bonds in GSH [81,82,113]. These findings highlight the importance of optimizing laser energy to balance signal intensity and molecular integrity.

Matrix selection alone was insufficient to overcome analytical limitations associated with MALDI MSI for metabolites. Despite testing six matrices across both ion modes, only four of nineteen target metabolites were detected under any single condition. Detection favoured higher molecular weight metabolites, while smaller metabolites remained largely undetectable, consistent with reduced sensitivity in the low *m/z* region due to matrix ions, chemical noise, and ion suppression from salts and lipids[75]. These findings indicate that matrix chemistry alone cannot adequately support detection of small, polar metabolites.

Washing tissue sections with various solvents produced trade-offs between reduced ion suppression and analyte loss. Acetone, methanol and ethanol improved signal for some metabolites, likely through removal of lipid species, but reduced detection of others. These findings align with previous reports demonstrating that organic solvent washes can both alleviate

ion suppression and remove endogenous metabolites [69,70]. Ammonium formate washing did not enable detection of any target metabolites, consistent with removal of highly soluble metabolites during aqueous washing [72]. These results demonstrate that although organic washes can alleviate ion suppression for select metabolites, they may simultaneously remove small molecules.

Given limited improvements to metabolite coverage achieved from matrix selection and washing, on-tissue chemical derivatization was investigated to enhance ionization efficiency. Derivatization with 4-APEBA + EDC did not improve coverage and resulted in substantial tissue damage, suggesting limited compatibility with desiccated mammalian tissues, consistent with previous optimization for use in hydrated samples such as plants or agar [79,80]. In contrast, TAHS derivatization substantially increased metabolite coverage and enabled detection of diverse amine-containing metabolites, in agreement with previous studies [66,76,114]. However, incomplete detection of target metabolites suggests that reactivity remains dependent on molecular structure, including charge and steric accessibility.

This work has several limitations. Experiments were performed using a single biological replicate; thus, absence of detection may reflect biological variability rather than analytical limitations. Additionally, metabolite annotations were based on accurate mass and chemical standards without confirmation by MS/MS.

Overall, TAHS derivatization provided the greatest improvement in metabolite coverage and represents an effective strategy for detecting methionine cycle metabolites by MALDI MSI. This optimized workflow establishes a foundation for subsequent spatial analysis of methionine metabolism in tumor tissues.

Chapter 3: Developing a multimodal MSI workflow

3.0 My Contributions

Madison Shiyuk performed all MALDI MSI-related experiments and data analyses described in **Chapter 3.2.13**. Cell culture and animal experiments were performed by Dr. Tian Zhao (BC Cancer, Victoria, BC). Mouse NSG tumor model experiments were performed by Jessica Morgan (BC Cancer, Victoria, BC). NanoDESI experiments were performed by Dr. Joseph Monaghan and Kiera Nguyen (Vancouver Island University, Nanaimo, BC). Immunofluorescence staining was performed by Katy Milne and Elise Lownsbrough (BC Cancer, Victoria, BC).

3.1 Chapter Introduction

To evade immune clearance, cancer cells frequently reprogram their metabolism toward an immunosuppressive phenotype. Defining metabolic features of immunosuppressive tumor regions is critical for improving clinical outcomes, given that presence of TILs, particularly $CD8^+$ T cells, is associated with improved patient survival [28]. Methionine metabolism is a key pathway contributing to tumor-mediated immune suppression. Methionine is essential for T cell activation due to its role in epigenetic reprogramming [51]; however, tumor cells can deplete the tumor microenvironment of methionine, limiting its availability for T cells [53]. At the same time, increased methionine consumption by tumor cells promotes accumulation of immunosuppressive metabolites, including MTA and SAM, which are associated with T cell exhaustion [115]. Consequently, dietary methionine restriction has been proposed as a strategy to reduce the

production of immunosuppressive methionine cycle metabolites by cancer cells, thereby improving anti-tumor immune function [54].

Understanding how methionine metabolism shapes immune cell infiltration within tumors requires spatially resolved approaches capable of linking metabolic and immune features within the TME. In this chapter, I developed a multimodal MSI workflow to investigate the impact of a methionine-restricted (MR) diet on tumor metabolism and T cell infiltration. This workflow integrates sequential MSI experiments on the same tissue section for detection of metabolites, lipids, and intact proteins while preserving tissue architecture. Integration of complementary imaging modalities will enable investigation of how dietary methionine restriction shapes spatial metabolic and immune niches within tumors.

3.2 Methods

3.2.1 Cell cultures

Mouse EG7-OVA tumor cells and OT-1 T cells were cultured as previously described (**Chapter 2.2.1**). Mouse E0771 cells (American Type Culture Collection, Cat. No. IOC-ZP255) were cultured in ATCC-modified RPMI medium as previously described (**Chapter 2.2.1.1**).

3.2.2. Animal studies

All animal studies were approved by the University of Victoria's Animal Care Committee (AUP #2023-019(3)) and were conducted in accordance with Canadian Council for Animal Care guidelines.

3.2.2.1 EG7 murine tumor model

Four-month-old female B6 Thy 1.1 mice were injected with 1 x 10^6 EG7-OVA tumor cells as previously described (**Chapter 2.2.2**). On day 5, mice received tail vein infusions of 5 x 10^5 or 1 x 10^6 activated $CD8^+$ OT-1 T cells cultured for 16 hours in control (100 µm methionine) or MR (5 µm methionine) medium. Immediately following OT-1 T cell infusion, mice were placed on a control diet (0.85% methionine: Teklad Cat. No. TD230144; n = 6) or a methionine restricted diet (0.06% methionine; Teklad Cat. No. TD230293; n = 6).

3.2.2.2 NSG murine tumor model

Female NOD/SCID/IL-2Rγ-null (NSG; Jackson Laboratory, Strain No. 005557) mice (6-8 weeks old) were acclimated for 2 weeks prior to subcutaneous injection of 5 x 10^6 OVCAR3 ovarian

tumor cells (ATCC; Cat. No. HTB-161) into the left flank. Tumors were measured three times per week using digital calipers, and area (length x width) was used to determine tumor burden. Mice were euthanized when tumors reached 200 mm^2, and tumors were harvested, embedded in CMC, and snap-frozen in liquid nitrogen.

3.2.3 Poly-L-lysine slide coating

Indium tin oxide (ITO)-coated glass slides (Delta Technologies Ltd, Cat. No. CB-901N-S111) were coated with polylysine to improve tissue adhesion. A solution of 50% poly-L-lysine (Sigma Aldrich, Cat. No. P8920) in LC-MS water (Thermo Fisher Scientific, Cat. No. W6-4) containing 0.1% octylphenoxypolyethoxyethanol (IGEPAL CA-630; Sigma Aldrich, Cat. No. I8896) was prepared. Aliquots of 20 µL were applied to each slide and spread evenly with an L-shaped spreader (Thermo Fisher Scientific, Cat. No. 14-664-230). Slides were dried at 60°C for 10 minutes, cooled to room temperature, and stored until use.

3.2.4 Cryosectioning

Cryosectioning was performed as described in **Chapter 2.2.3**. Tissue sections for MALDI MSI were adhered to polylysine-coated ITO slides (**Chapter 3.2.3**), and sections for immunofluorescence staining or H&E staining were adhered to Superfrost™ Plus slides (Thermo Fisher Scientific, Cat. No. 1255015).

3.2.5 On-tissue chemical derivatization

Chemical standards were applied to glass slides adjacent to tissue sections as described in **Chapter 2.2.5**. On-tissue derivatization with TAHS was performed as described in **Chapter 2.2.6**, including reagent application (**Supplementary Table 1)** and overnight incubation at 60°C in a humidified chamber. Matrix (2,5-DHB) was subsequently applied as described in **Supplementary Table 1**.

3.2.6 MALDI IHC

Following MALDI MSI for lipids, norharmane matrix was removed with two 3-minute washes in methanol at -20ºC. Slides were vacuum-dried (10 minutes) and fixed in 1% paraformaldehyde (PFA; Sigma Aldrich, Cat. No. 158127-100G) for 30 minutes. Slides were washed in 0.1 M phosphate-buffered saline (PBS; 0.0027 M potassium chloride; 0.137 M sodium chloride; pH 7.4; Sigma Aldrich, Cat. No. P4417-100TAB) for 10 minutess, followed by methanol (2 x 3 minutes), and Carnoy's solution (6:3:1 v/v/v ethanol: chloroform: acetic acid; ethanol: Commercial Alcohols, Cat. No. P016EAAN; chloroform: Sigma Aldrich, Cat. No. 366927; acetic acid: Anachemia, Cat. No. 00598-463) for 3 minutes. Tissues were rehydrated through a series of graded ethanol washes: 100% (2 x 2 minutes), then 95%, 70%, and 50% for 3 minutes and washed in Tris-buffered saline (TBS; pH 7.5; Thermo Fisher Scientific, Cat. No. AAJ60764K7) for 10 minutes. Antigen retrieval was performed in alkaline retrieval buffer (Abcam, Cat. No. AB93684) at 95°C for 30 minutes, followed by cooling to room temperature for 30 minutes in the same staining jar. Slides were washed in TBS (10 minutes) and treated for 1 hour in tissue blocking buffer (TBS containing 0.05% w/v octyl-β-glucopyranoside, 5% w/v

bovine serum albumin, and 4% v/v normal rabbit serum (Sigma Aldrich, Cat. Nos. 03757 and 011-000-120; Jackson ImmunoResearch, Cat. No. 011-000-120). Miralys ™ antibody probes (AmberGen) targeting CD3ε, CD8α, and vimentin were prepared at 1 µg/mL (details in **Supplementary Table 4**). A hydrophobic barrier pen (Sigma Aldrich, Cat. No. Z377821) was used to outline a region around each tissue to confine 100 µL of antibody solution to each tissue. Slides were incubated overnight (18 hours) at 4°C in a dark, humidified chamber.

Slides were in TBS for (3 x 5 minutes) each, followed by 50 mM ammonium bicarbonate buffer (Sigma Aldrich, Cat. No. A6141) for 10 seconds and then 3 x 2 minutes. Slides were dried under vacuum (1.5 h) protected from light. Photocleavage was performed for 10 minutes using a light box (AmberGen) to release photocleavable mass tags (PC-MTs™). Next, CHCA matrix was applied using an HTX M5 sprayer (**Supplementary Table 1**) and recrystallized in vapour from 5% isopropanol (Thermo Fisher Scientific, Cat. No. A4644) at 60°C for 75 seconds.

3.2.7 MALDI MSI

3.2.7.1 Metabolites

Following TAHS derivatization, tissues were imaged in positive ion polarity using a timsTOF *flex* MALDI-2 instrument (Bruker Daltonics) with acquisition parameters as described in **Chapter 2.2.8.** Tandem mass spectrometry (MS/MS) was performed on tissues and chemical standards using an isolation width of ± 1 *m/z* around the derivatized precursor ion.

3.2.7.2 Lipids

Tissues were imaged following application of norharmane matrix (**Supplementary Table 1**) on a timsTOF *flex* MALDI-2 instrument at 50 µm spatial resolution over *m/z* 200-2,500 range. Laser settings with SmartBeam (Bruker) included 400 shots per pixel, 10,000 Hz frequency, and 10.0 µs post-ionization delay. Instrument parameters were as follows: funnel RF (350, 500, and 500 Vpp for funnel 1, funnel 2, and multipole), quadrupole ion energy (5.0 eV), and pre-TOF focus (150 µs transfer time;15 µs pre-pulse storage). External calibration was performed using an ESI-L low concentration tuning mix (Agilent Technologies, Cat. No. G1969-85000). Online calibration used norharmane (*m/z* 515.1620), PI-(38:4) (*m/z* 885.5497), CL-(72:8) (*m/z* 1447.9650), and CL-(72:7) (*m/z* 1449.9806). For tissues imaged with 2,5-DHA, the norharmane ion was excluded.

3.2.7.3 MALDI IHC

A timsTOF *flex* MALDI-2 instrument in positive ion mode was used for MSI analysis at 50 µm step size over *m/z* 700-1,850 range. Custom laser settings with SmartBeam (Bruker) were used: 300 shots per pixel, 5,000 Hz frequency, and 0.0 µs post-ionization delay. Instrument parameters were optimized for detection of PC-MTs™, including funnel RF amplitudes (funnel 1 RF: 250 Vpp; funnel 2 RF: 500 Vpp; multipole RF: 500 Vpp), quadrupole ion energy (25.0 eV), and pre-TOF focus (110 µs transfer time; 15.0 µs pre-pulse storage). External calibration was performed prior to analysis using an ESI-L low concentration tuning mix. Online calibration was performed during acquisition with PC-MT™ ions as reference masses (CD3ε: *m/z* 1161.64; vimentin: *m/z* 1230.84) due to minimal matrix or endogenous background signal in the acquired mass range.

3.2.8 NanoDESI MSI

Mass spectrometry imaging with nanoDESI was performed in positive ion mode using an Orbitrap Exploris™ 120 instrument coupled to a custom ion source described previously [104,116]. Two silica capillaries (50 µm inner diameter, 150 µm outer diameter; Molex, Cat. No. 106815002) were positioned at a 90° angle. A spray solvent (9:1 MeOH: H_2O with 0.1% formic acid) was delivered to the primary capillary and aspirated through the secondary capillary using 2-3 L/min nitrogen gas flow controlled by a mass flow controller (Sensirion, Cat. No. SFC-6000D-5LSPM). Tissue sections were rastered beneath the fixed capillary configuration using a motorized stage (Zaber Technologies) 40 µm/s in the x direction with a 150 µm step size in the y direction. Electrospray was generated using a capillary voltage of +3.4 kV. Full-scan data were acquired between *m/z* 70-500 and *m/z* 480-1,000 ranges. Data were converted into imzML format using imzML writer (v1.1.4) [117] and imported into SCiLS Lab™ for analysis.

3.2.9 Post-MSI sample processing

3.2.9.1 Optical images

Tissues subjected to either norharmane or 2,5-DHA for method optimization were imaged at 4x resolution using a PathScan Enabler 5 (Meyer Instruments) before matrix application, after matrix application, and after matrix removal. Matrices were removed from tissues using two 3-minute washes in ice-cold organic solvent. Norharmane was washed off with methanol (Thermo Fisher Scientific, Cat. No. A4564) and 2,5-DHA with acetonitrile (Thermo Fisher Scientific, Cat. No. A9554).

3.2.9.2 Hematoxylin and eosin staining

Hematoxylin and eosin (H&E) staining was performed on tissue sections following sequential nanoDESI MSI, MALDI MSI, and MALDI IHC (**Figure 6**) as described in **Chapter 2.2.8**. Brightfield images were acquired at 20x magnification using an Aperio Versa scanner (Leica Biosystems).

3.2.10 Immunofluorescence staining

Tissue sections serial to those used for multimodal MSI were thawed to room temperature and fixation in 10% neutral buffered formalin (Sigma Aldrich, Cat. No. HT501128) for 30 minutes. Sections were rehydrated through graded ethanol washes (100% ethanol 2 x 2 minutes, then 90%, 70%, and 50% ethanol for 3 minutes each) followed by a rinse in distilled water. Multiplex immunofluorescence staining was performed using an IntelliPATH ® automated staining platform (Biocare Medical). Three sequential staining rounds targeted CD3, CD8α, and CD4. Antigen retrieval was not performed prior CD3 staining but was included in subsequent rounds using pH 6 buffer (Akoya Biosciences, Cat. No. AR6001KT) before CD8α and pH 9 buffer (Akoya Biosciences, Cat. No. AR9001KT) before CD4. Endogenous peroxidase activity was blocked using Peroxidazed 1 (Biocare Medical, Cat. No. PX968) for 5 min, followed by blocking with Sniper 10 (Biocare Medical, Cat. No. BS966) for 10 minutes. Primary antibodies were applied and incubated for 30 minutes: rabbit anti-CD3 (clone SP7; Abcam, Cat. No. ab16669; 1:500) rabbit anti-CD8α (clone D4W2Z; Cell Signalling Technology, Cat. No. 98941; 1:100); and rabbit anti-CD4 (clone EPR19514; Abcam, Cat. No. ab183685; 1:1,000).

Signal detection was performed using horseradish peroxidase (HRP)-conjugated anti-rabbit polymer reagents (M4Rb-HRP for CD3; M2Rb-HRP for CD8α and CD4; Active MOTiF™, Cat. No. 13104) for 10 minutes. Tyramide signal amplification was carried out using Opal fluorophores (Akoya Biosciences, Cat. No. FP1488001KT): Opal 620 (1:100) for CD3; Opal 720 (1:200) for CD8α; Opal 690 (1:100) for CD4 (10 minutes each). Nuclei were counterstained with DAPI (1 drop in 500 μL buffer) for 5 minutes, and slides were coverslipped with ProLong™ Diamond Antifade Mountant (Thermo Fisher Scientific, Cat. No. P36970). Imaging was performed using a Polaris MOTiF™ imaging platform (Akoya Biosciences). Tonsil tissue served control for antibody performance and expected membrane localization.

3.2.13 Data analysis

3.2.13.1 Pre-processing and feature detection

Raw data were imported into SCiLS Lab™ and normalized to TIC. Feature detection for MALDI datasets was performed using the TREX^2 (qTOF) algorithm with an interval width of ± 10 ppm, a minimum relative intensity threshold of 0.5%, a minimum spatial coverage of 5%, and weak spatial noise filtering. Putative lipid annotations were assigned using MetaboScape® (Bruker) *via* the LipidSpecies tool with the MCube Lipid Species Annotation method. Annotated lipid features were grouped by lipid class based on annotations, with feature selection, annotations, and filtering (**Chapter 3.2.13.2**) performed independently for this analysis. For nanoDESI datasets, metabolite features were annotated based on accurate mass matching to a hypothesis-driven list of 78 metabolites (**Supplementary Table 3**).

3.2.13.2 Feature signal quality filtering

Filtering was performed prior to hypothesis testing and independent of statistical outcomes. For nanoDESI metabolites, features were required to exceed an absolute TIC-normalized intensity threshold of 100 arbitrary units in at least 7 of 11 tumors. This reduced the dataset from 78 to 42 metabolites retained for downstream analysis. For lipid features, off-tissue regions consisting of matrix and embedding medium were acquired for each tissue. Mean TIC-normalized intensities from these regions were used to calculate signal-to-noise signal ratios. A small pseudocount (0.01) was added to background intensities to prevent division artifacts. Lipid features were required to meet the following criteria: signal-to-noise ≥ 5, mean TIC-normalized intensity $\geq$ 100 arbitrary units, with both previous criteria satisfied in at least 7 of 11 tumors. Application of these filters reduced the dataset from 287 annotated lipid features to 111 retained for downstream analysis.

3.2.13.3 Lipid class composition analysis

Annotated lipid features were grouped by lipid class based on MetaboScape® annotations. Feature selection and signal quality filtering were performed independently for this analysis using the feature selection and filtering criteria described in **Chapter 3.2.13.1** and **Chapter 3.2.13.2**. The number of lipids within each class was calculated for each dataset, and relative class composition was expressed as the proportion of total annotated lipid features contributed by each class. For visualization, lipid class distributions were plotted as stacked bar charts normalized to 100% using GraphPad Prism.

3.2.13.4 $CD8^+$ T cell detection and region generation

A QuPath (version 0.6.0) workflow was used to detect $CD8^+$ T cells and define regions of interest (ROIs) representing areas of high and low $CD8^+$ T cell infiltration from immunofluorescence images. Automated cell detection was performed using the Positive Cell Detection tool. Nuclei were identified using the DAPI channel with the following parameters: requested pixel size of 0.5 µm, background radius of 12 µm back, smoothing sigma of 2.5 µm, minimum nuclear area of 10 μm^2, maximum nuclear area of 300 μm^2, and an intensity threshold of 4. Cells positive for CD8 were identified based on mean fluorescence intensity in the Opal 570 channel, with a threshold of ≥ 35 arbitrary units used to classify $CD8^+$ T cells. Detection parameters were empirically optimized to accurately identify nuclei and $CD8^+$ T cells while minimizing false positives (**Supplementary Figure 2A**). Mean $CD8^+$ T cell density for each tumor was calculated by dividing the number of $CD8^+$ T cells by the corresponding tumor area and expressed as cells/ mm^2.

To define ROIs, a separate pixel classification workflow was applied to the Opal 570 channel. Results from the $CD8^+$ T cell detection workflow were used to guide selection of pixel-level intensity thresholds. Gaussian prefiltering ($\sigma = 1.5$) was applied to reduce noise, and a fluorescence intensity threshold of 4 arbitrary units was used to identify pixels with elevated CD8 signal. Regions containing pixels exceeding this threshold were defined as "high $CD8^+$ T cell" ROIs. Total tissue area was delineated using the DAPI channel, with pixels of intensity with ≥ 1 arbitrary unit used to define tissue boundaries. The high $CD8^+$ ROI was then subtracted from the DAPI-defined region to generate a "low $CD8^+$ T cell" ROI, representing tissue areas with CD8 signal below the defined threshold. Regions of interest were exported from QuPath as

SCiLS exchange files (.sef), imported into SCiLS Lab™, and co-registered with nanoDESI and MALDI MSI datasets. These annotations were used to generate paired high and low $CD8^+$ T cell regions within each tumor (n = 11). Mean TIC-normalized intensities were calculated for each ROI for downstream statistical analysis. A representative ROI is shown in **Supplementary Figure 4B &C**.

3.2.13.5 Spatial segmentation

Datasets acquired with nanoDESI or MALDI MSI were imported into SCiLS Lab™ and were normalized to TIC. Unsupervised spatial segmentation was performed using the bisecting k-means algorithm with weak spatial denoising. Segmentation was conducted using filtered feature sets consisting of metabolites (n = 42) or lipids (n = 111) retained after signal quality filtering (**Chapter 3.2.13.2**).

3.2.13.6 Statistical analysis

Data processing and statistical analyses were performed in R (version 4.5.3) unless otherwise specified. Mass spectrometry imaging data were imported from imzML files and processed using the *Cardinal* package [118] to extract pixel-level ion intensities within defined *m/z* windows (± 10 ppm). For each target *m/z* value, signal within the specified mass window was summed to yield a single intensity value per pixel. Intensity values were $\log_2$ transformed prior to statistical analysis.

<u>3.2.13.6.1 $CD8^+$ T cell density analysis</u>

Tumor-level $CD8^+$ T cell densities (cells/ mm^2) were compared between diet groups using a two-tailed, unpaired Mann-Whitney test in GraphPad Prism. Tumors were treated as independent biological replicates, and statistical significance was defined as $p < 0.05$.

3.2.13.5.2 Comparison of metabolites detected with different MSI modalities

To assess the effect of dietary methionine restriction on molecular abundance across the full tumor area, linear mixed-effects models were applied to pixel-level intensity data. Models were fit using the *lme4* package, with diet specified as a fixed effect and tumor identity included as a random intercept to account for non-independence of pixels within tumors [119]. Statistical significance of fixed effects was assessed using Type III analysis of variance with Satterthwaite's approximation for degrees of freedom (*lmerTest*) [120]. Separate models were fit for the nanoDESI and MALDI datasets.

3.2.13.6.3 Comparison of CD8-defined regions

To evaluate molecular differences between CD8-defined regions, pixel-level ion intensities were assigned to paired high- and low- $CD8^+$ T cell regions within each tumor, as defined using QuPath (**Chapter 3.2.13.3**). Analyses were restricted to features retained after signal quality filtering, including 42 metabolites and 111 lipids (**Chapter 3.2.13.2**). Linear mixed-effects models were applied as described above, with diet as a fixed effect and tumor as a random intercept.

3.2.13.6.4 Diet effects on molecules in regions with $CD8^+$ T cells

To assess the effect of dietary methionine restriction on molecular patterns in immune-infiltrated regions, analyses were restricted to pixels assigned to high-$CD8^+$ T cell regions (**Chapter 3.2.13.4**) and features retained after filtering (**Chapter 3.2.13.2**). Tumors were grouped by dietary condition (control or MR), and linear mixed-effects models were applied as described above, with diet as a fixed effect and tumor as a random intercept.

3.2.13.6.5 Multiple testing and significance thresholds

For MSI analyses performed in R, p-values were adjusted using the Benjamini-Hochberg (BH) false discovery rate (FDR) procedure [121]. Adjusted p-values (q-values) < 0.05 were considered statistically significant. For visualization, statistical significance was annotated only for comparisons exceeding a fold-change threshold of 2.

3.2.13.6.6 Visualization

Data visualization was performed using GraphPad Prism. For MSI analyses, intensity values were $\log_2$ transformed prior to visualization.

3.3 Results

To investigate the effect of methionine restriction on tumor metabolism and immune infiltration, a multimodal MSI workflow was developed. This workflow integrated sequential nanoDESI MSI for metabolite detection, MALDI MSI for lipid profiling, and MALDI IHC for immune cell protein markers, followed by H&E staining for histological context (**Figure 6**).

Implementation of this workflow required optimization of multiple experimental parameters to ensure robust detection across modalities. For lipid MALDI MSI, matrix selection was evaluated to maximize lipid coverage, and for MALDI IHC, antibody specificity and performance were evaluated using positive and negative controls.

Acquisition of these complementary datasets from a single tissue section enabled direct spatial comparison of metabolic and immune features while preserving tissue architecture. This approach allowed investigation of how dietary methionine metabolism shapes spatially defined immune and metabolic niches within tumors.

Figure 6. *Multimodal workflow design.*

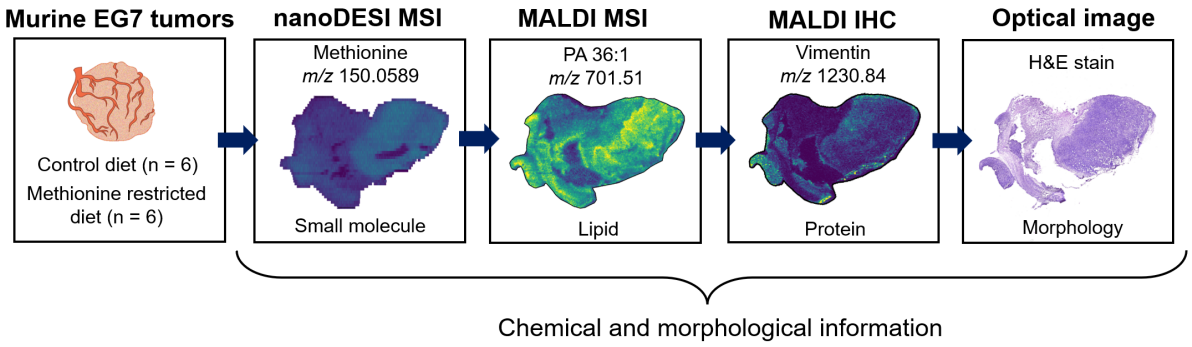

3.3.1 Metabolite coverage by MALDI *vs.* nanoDESI

To assess the robustness of nanoDESI MSI for detection of methionine cycle metabolites, results were compared with a complementary MALDI MSI workflow using TAHS derivatization (**Chapter 2.3.4**). This enabled comparison of spatial organization and detection of biologically relevant differences between nanoDESI and an established MALDI-based approach.

Tandem mass spectra were acquired for TAHS-derivatized cysteine, GSH, GSSG, homocysteine, methionine, putrescine, SAH, spermidine, and spermine to support metabolite annotations (**Supplementary Figure 1**). Relative abundances of arginine, cystathionine, and ornithine were insufficient to obtain diagnostic MS/MS spectra. For nanoDESI MSI, metabolite annotations were supported by high mass accuracy measurements acquired on an Orbitrap instrument.

Unsupervised spatial segmentation was performed independently on both datasets using a shared feature list of methionine metabolites (**Supplementary Table 3**). Segmentation identified highly similar spatial regions across modalities (**Figure 7A & B**).

Methionine cycle metabolites detected by both modalities were compared between control and methionine-restricted (MR) diet groups. Analyses were restricted to metabolites detected with each modality (**Figure 7C & D**). Given the spatially heterogenous nature of MSI data, comparisons between platforms were performed at the pixel level to capture local variations in signal intensity that may be influenced by platform-specific ionization behaviour. Comparison of tumor-level mean intensities showed some consistent trends across metabolites, including decreased arginine and cysteine in MR tumors (**Figure 7C & D**). Both modalities showed

decreased methionine in MR tumors, which reached statistical significance only in MALDI (**Figure 7C & D**). Additional statistically significant differences were not identified between diet groups. However, some metabolites exhibited modality-dependent trends; nanoDESI showed increased spermidine and spermine in MR tumors, where MALDI showed opposite trends (**Figure 7C & D**).

Figure 7. *Comparative analysis of spatial organization and metabolite detection between MSI modalities.*

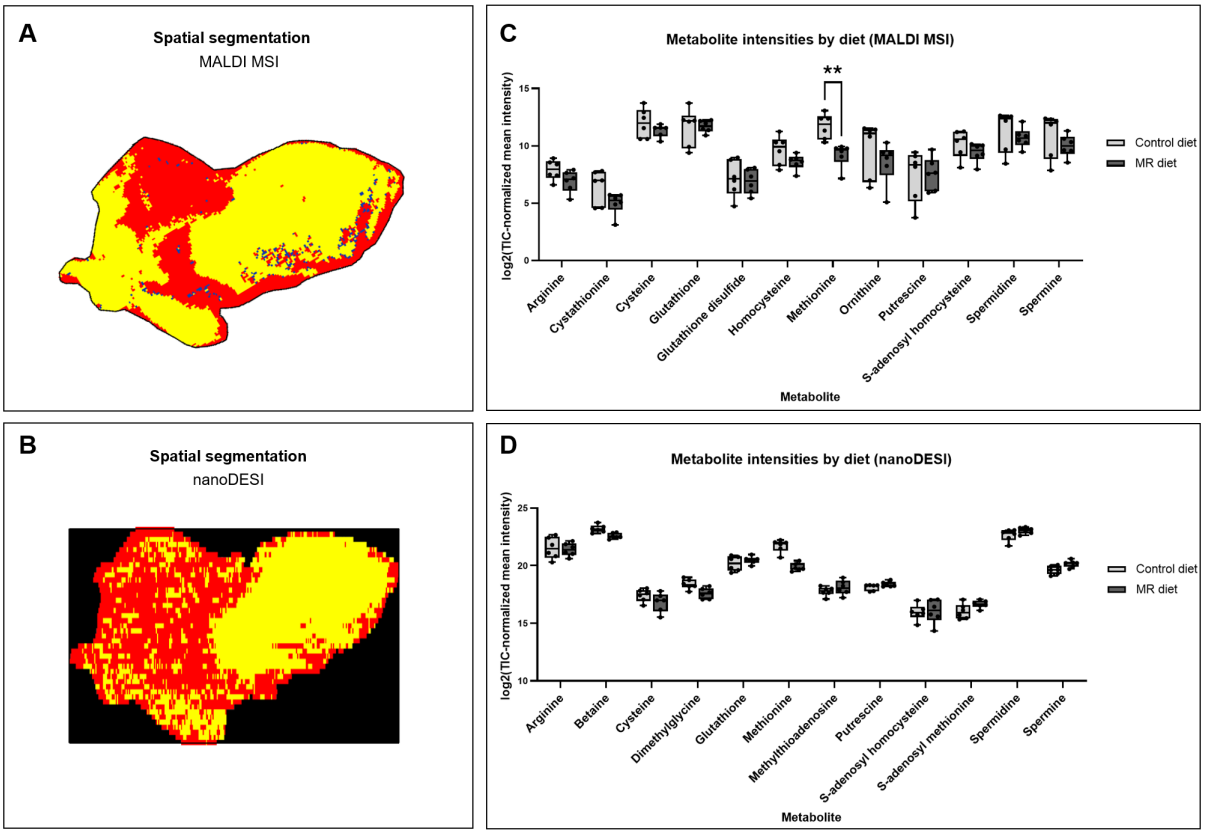

A-B. Representative spatial segmentation maps generated from (**A**) MALDI and (**B**) nanoDESI MSI datasets using identical metabolite feature lists. **C-D.** Tumor-level mean metabolite intensities of in control and MR tumors, detected by (**C**) MALDI or (**D**) nanoDESI MSI. Statistical comparisons were performed independently for MALDI and nanoDESI using pixel-level linear mixed-effects modelling (diet as fixed effect; tumor as random intercept) with BH FDR correction. A two-fold change threshold was applied for effect size interpretation. Asterisks indicate features meeting both q-value and fold-change thresholds (** $q < 0.01$).

3.3.2 Optimizing for detection of lipids via MALDI MSI

To enable lipid imaging following nanoDESI metabolite analysis on the same tissue section (**Figure 6**), matrix selection was first optimized to maximize coverage of lipid classes while preserving tissue integrity.

Tissues were analyzed using two matrices (norharmane and 2,5-DHA) followed by feature finding and lipid annotation. Use of norharmane resulted in a greater number of lipid annotations (n = 588) compared to 2,5-DHA (n = 375) (**Figure 8A**). Lipid class composition also differed between matrices. Norharmane enabled detection of cardiolipins (CLs), phosphatidylserines (PSs), and phosphatidylethanolamines (PEs), while 2,5-DHA predominantly yielded PEs and lysophospholipids (LPIs) (**Figure 8A**). Cardiolipin species were not detected with 2,5-DHA (**Figure 8A**). Next, tissue integrity following matrix application and removal was assessed. Tissue morphology was preserved with norharmane across preparation steps (**Figure 8B**). In contrast, tissues treated with 2,5-DHA exhibited visible cracking following matrix removal and retained residual matrix after washing (**Figure 8B**). Based on these results, norharmane was selected for subsequent lipid imaging experiments.

To evaluate compatibility with sequential imaging (**Figure 6**), norharmane was applied to tissue sections previously imaged by nanoDESI. Unsupervised spatial segmentation was performed independently using nanoDESI metabolite features and MALDI lipid features (**Figure 8C & D**). Segmentation maps derived from each modality identified similar spatial regions (**Figure 8C & D**). Comparison of an individual ion detected by both modalities showed comparable spatial localization patterns (**Figure 8E & F**).

***Figure 8**. Matrix and imaging modality effects on lipid detection and spatial distribution.*

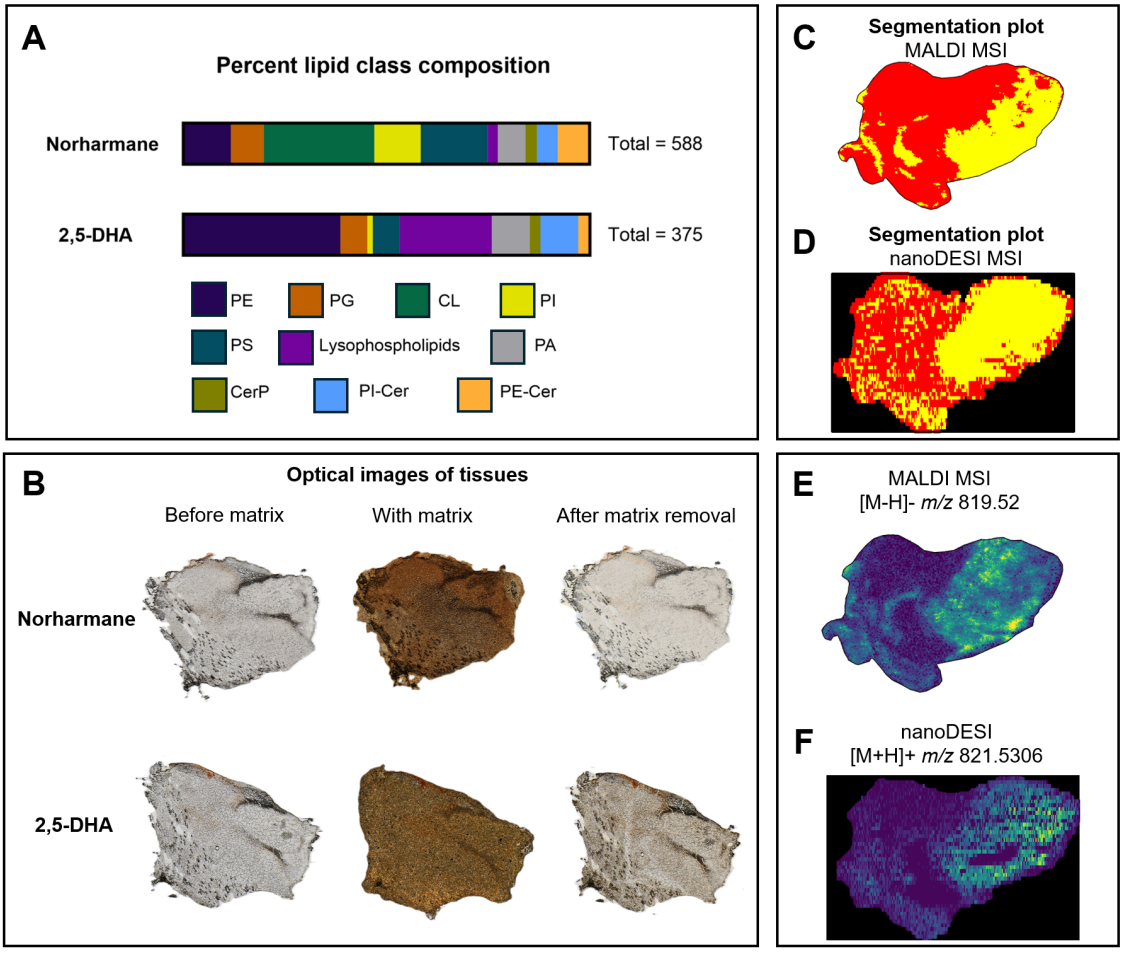

A. Class composition of annotated lipid species detected in MALDI MSI datasets acquired using norharmane or 2,5-DHA matrices. Stacked bar graphs normalized to 100% intensity display the relative contribution of each lipid class to the total number of annotated features detected with each matrix. **B.** Optical images of tissues analyzed with norharmane or 2,5-DHA at different time points through the MALDI MSI workflow. **C-D.** Representative spatial segmentation of **(C)** lipid distributions acquired using MALDI MSI or **(D)** metabolite distributions detected with nanoDESI. Spatial segmentations were performed on the same tissue section following multimodal analysis. **E-F.** Ion images of a feature detected on the same tissue section with **(E)** MALDI MSI or **(F)** nanoDESI MSI to facilitate spatial comparisons.

3.3.3 Application of MALDI IHC within a multimodal workflow

Following nanoDESI metabolite imaging and MALDI lipid analysis, MALDI IHC was performed on the same tissue sections to assess detection of intact protein markers (**Figure 6**). Custom antibody probes were synthesized for this study (AmberGen; **Supplementary Table 4**) and required validation prior to application in tumor tissues.

To assess antibody specificity, a murine NSG tumor, which lacks T cells, was used as a negative control (**Figure 9A-C**). The NSG tissue section was additionally spotted with $CD3\varepsilon^+$ $CD8\alpha^+$ OT-1 T cells as a positive control and with CD3ε- CD8α- EG7-OVA cells to assess signal associated with increased cell density (**Figure 9A-C**). Both the CD3ε and CD8α antibodies produced high signal intensity within the OT-1 T cell spot, with minimal signal detected in the EG7-OVA cell spot and surrounding NSG tissue (**Figure 9A & B**). Vimentin signal was detected throughout NSG tissue, with reduced intensity observed in the OT-1 T cell spot (**Figure 9C**).

The MALDI IHC assay was subsequently applied to EG7 tumor sections from control and MR diet groups that had previously been subjected to nanoDESI and MALDI MSI. Immunofluorescence (IF) staining was performed on serial tissue sections to assess immune cell distributions in parallel with MALDI IHC. Signal corresponding to the CD3ε antibody was observed throughout tumor tissues (F**igure 9D**). Immunofluorescence staining of a serial section showed a similar distribution of CD3ε signal (**Figure 9E**). The MALDI IHC approach did not result in detection of CD8α signal in EG7 tumor sections (**Figure 9D**), while immunofluorescence showed low levels of $CD8^+$ T cells primarily localized to the tumor

periphery (**Figure 9E**). Vimentin signal was distributed throughout tumor tissue and co-localized with regions of increased cellular density observed in post-MSI H&E staining (**Figure 9D & F).**

Figure 9. *Spatial detection of protein markers using MALDI IHC.*

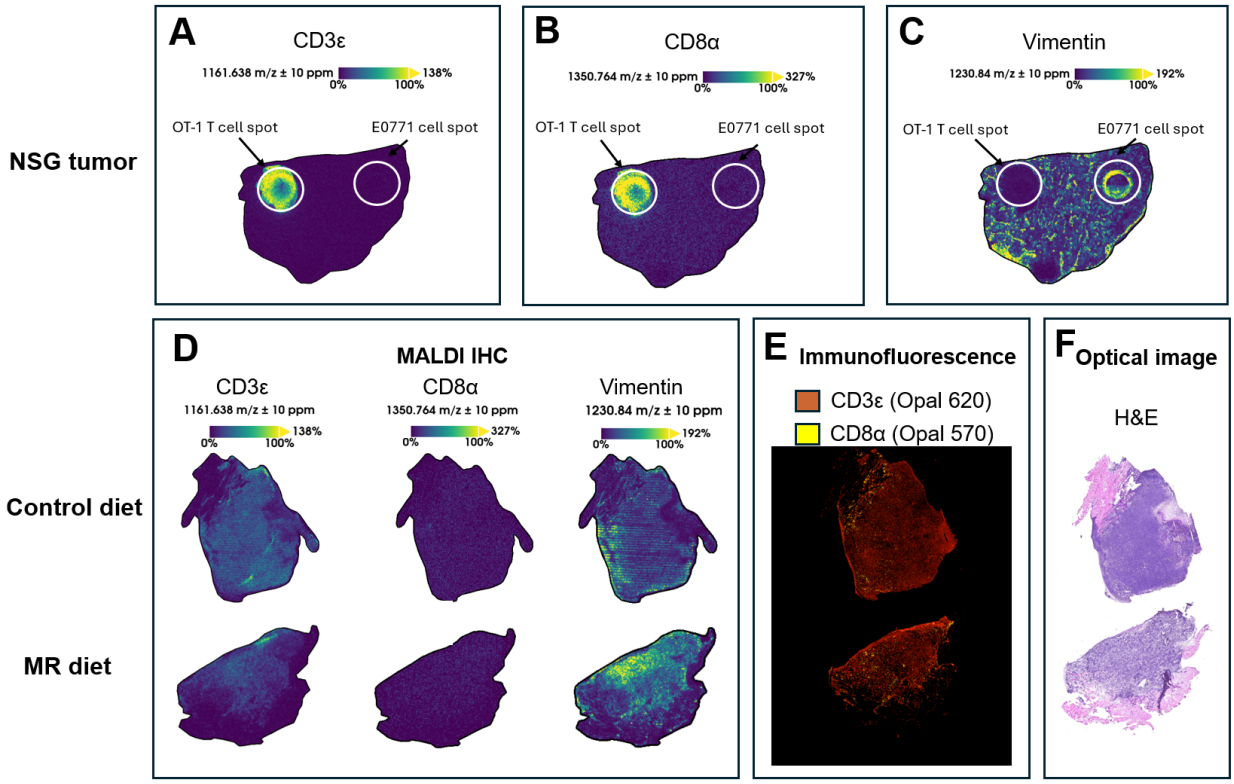

A-C. Spatial distributions of PC-MT™ reporter ions corresponding to (**A**) CD3ε, (**B**) CD8α, and (**C**) vimentin on an NSG mouse tumor section spotted with positive (OT-1) or negative (E0771) control cell lines to evaluate antibody specificity. **D.** Spatial distributions PC-MT™ reporter ions in murine tumors subjected to a control or methionine restricted diet, as detected with MALDI IHC. **E**. Immunofluorescence stains of CD3ε (Opal 620) and CD8α (Opal 570) markers on serial tissue sections corresponding to those analyzed with MALDI IHC. **F.** Hematoxylin and eosin (H&E) staining of tumor tissues following MALDI IHC analysis.

3.3.4 Molecules observed in T cell-infiltrated regions

To assess whether an MR diet affected T cell infiltration, $CD8^+$ T cell density was quantified from immunofluorescence-stained tumor sections using a QuPath workflow (**Supplementary Figure 2A**). Differences in $CD8^+$ T cell density (cells/ mm^2) between control and methionine restricted diet groups were evaluated using a two-tailed Mann-Whitney test (**Figure 10A**). Median $CD8^+$ T cell density was slightly higher in tumors from the control diet group compared to the methionine restricted group; however, this difference was not statistically significant ($p = 0.6623$; **Figure 10A**).

To investigate molecular differences associated with $CD8^+$ T cell infiltration, immunofluorescence images were used to generate regions with high and low $CD8^+$ T cell density (**Supplementary Figure 2B & C**). For nanoDESI MSI, metabolite analyses were performed using a targeted, hypothesis-driven panel of 78 metabolites (reduced to 42 following signal quality filtering), selected based on established roles in tumor immune modulation. In contrast, lipid analyses were performed in an untargeted manner using feature detection in SCiLS Lab™. Mass spectrometry imaging datasets consist of large numbers of spatially resolved pixels that are not independent and are nested within tumors; thus, differences between high- and low-$CD8^+$ T cell regions were assessed using linear mixed-effects models with region as a fixed effect and tumor as a random intercept. Statistical significance was interpreted alongside effect size, as the large number of pixels in MSI datasets can enable detection of small but consistent differences that may not be biologically meaningful.

All metabolites detected using nanoDESI MSI exhibited small effect sizes (log_2 FC ~ 0.2) and were therefore not considered biologically meaningful for downstream visualization (**Figure 10B; Supplementary Figure 3A).** However, several metabolites including ornithine, cysteine, and nicotinamide were significantly enriched in high- $CD8^+$ regions despite not reaching the two-fold change threshold (**Supplementary Figure 10A**).

For lipids detected by MALDI MSI, a strong and consistent enrichment in high- $CD8^+$ T cell regions was observed, with the majority of the 111 lipids analyzed showing higher abundance in these regions (**Figure 10C; Supplementary Figure 3B**). Among these, PG-(40:7), PS-(40:4), and PS-(O-38:5) met both statistical significance after FDR correction and a fold-change threshold of >2, indicating robust enrichment in $CD8^+$ T cell-rich regions (**Supplementary Figure 3B**).

To determine whether an MR diet altered metabolic patterns associated with $CD8^+$ T cell infiltration, molecular profiles in regions with high $CD8^+$ T cell infiltration were compared between control and MR diet conditions. No metabolites met statistical significance ($q < 0.05$) or fold-change (FC > 2) thresholds, indicating weak or inconsistent enrichment in MR *vs.* control tumors (**Supplementary Figure 3C**). In contrast, several lipids exhibited diet-dependent differences between control and MR $CD8^+$ T cell-rich regions. In tumors subjected to a control diet, lipids including PI-(38:6), PS-(40:4), CL-(74:10), and PI-(O-38:5) were enriched, while PA-(44:8) was enriched in MR tumors (**Supplementary Figure 3D**).

Figure 10. *$CD8^+$ T cell density and associated metabolic changes in control and MR tumors.*

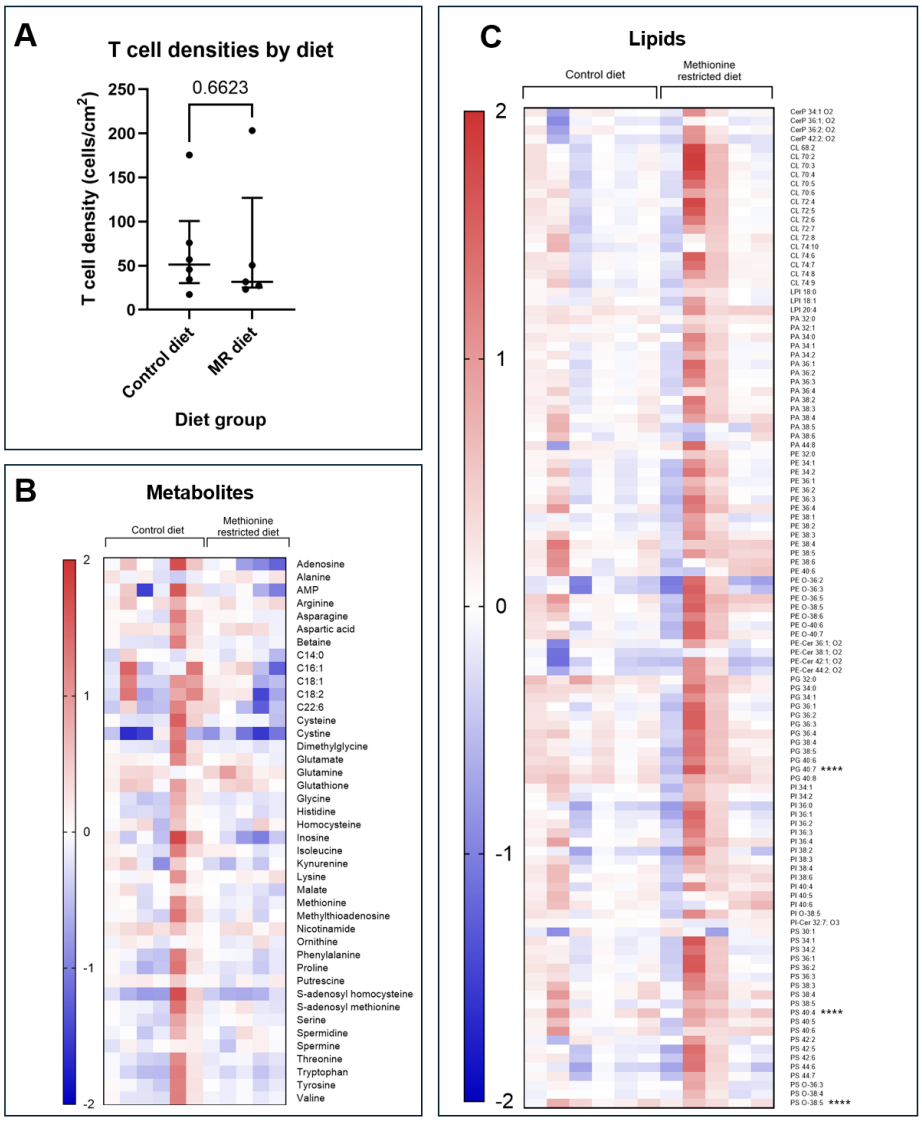

A. Quantification of T cell density (cells/mm^2) in tumors from animals fed a control diet (n = 6) or methionine restricted diet (n = 5). Differences between groups were assessed using a two-tailed, unpaired Mann-Whitney test. Individual tumors are shown as scatter points, with median and interquartile range indicated. **B-C.** Heatmaps showing relative (**B**) metabolite and (**C**) lipid differences between regions with high and low $CD8^+$ T cell abundance across tumors. Log_2 fold changes were calculated as log_2(high $CD8^+$/ low $CD8^+$), where positive values reflect enrichment in high-$CD8^+$ T cell regions and negative values reflect enrichment in low-$CD8^+$ T cell regions. Statistical comparisons were performed on pixel-level ion intensities using linear mixed-effects models with region (high *vs.* low $CD8^+$ T cells) as a fixed effect and tumor as a random intercept. False discovery rate was controlled using the BH procedure. Features meeting both $q < 0.05$ and a fold-change threshold > 2 were considered significant and are denoted with asterisks (* $q < 0.05$; ** $q < 0.01$; *** $q < 0.001$; **** $q < 0.0001$).

3.4 Chapter Discussion

This chapter established a multimodal MSI workflow to investigate the impact of dietary methionine restriction on tumor metabolism and immune infiltration. Analysis using MALDI MSI following TAHS derivatization and nanoDESI MSI provided complementary coverage of methionine cycle metabolites, consistent with previous studies demonstrating synergy between MALDI- and DESI-based imaging approaches[105,106]. The MALDI MSI approach enabled detection of amine-containing metabolites following TAHS derivatization, while nanoDESI preferentially detected highly polar metabolites, including betaine, dimethylglycine, and SAM, in agreement with prior reports [78,103,104]. Variations in relative metabolite abundances between modalities likely reflect technique-dependent ion suppression effect rather than true biological differences [122].

Matrix optimization identified norharmane as the most suitable matrix for lipid imaging, enabling broader lipid class coverage, including cardiolipin species, and improved tissue preservation compared to 2,5-DHA. Detection of cardiolipins with norharmane is consistent with previous MSI studies [92]. Sequential MALDI IHC demonstrated feasibility of protein detection following nanoDESI and MALDI MSI; however, detection of $CD3\varepsilon^+$ and $CD8\alpha^+$ T cells was not achieved. The EG7 tumor model expresses $CD3\varepsilon^+$ [123], preventing discrimination of $CD3\varepsilon^+$ T cells from tumor cells. Low $CD8\alpha^+$ T cell abundance limited detection, highlighting challenges in identifying low-abundance immune populations.

Spatial analysis of regions high and low $CD8\alpha^+$ T cell infiltration revealed molecular differences associated with $CD8\alpha^+$ T cells. Several metabolites, including ornithine, cysteine, and

nicotinamide, were significantly associated with CD8α$^+$ T cell-rich regions, but differences in their abundance were subtle. Consistent enrichment of cysteine, ornithine, and nicotinamide in high-CD8α$^+$ T cell regions aligned with established roles for these metabolites. Cysteine is required for T cell activation, ornithine serves as a precursor for polyamine metabolites linked to T cell exhaustion, and nicotinamide modulates T cell exhaustion [47,49,55]. Further, lipidomic demonstrated revealed widespread enrichment of lipids in CD8$^+$ T cell-rich regions, with PG-(40:7), PS-(40:4), and PS-(O-38:5) showing large effect sizes. These findings suggests that lipid remodelling may be a dominant feature of immune-infiltrated TMEs.

Dietary methionine restriction did not substantially alter metabolite abundances within CD8α$^+$ T cell-rich regions, suggesting that key metabolite pools supporting T cell function may be relatively preserved under dietary constraint. In contrast, several lipids exhibited diet-dependent differences, indicating that lipid metabolism is more responsive to dietary perturbation than small molecule metabolites within immune-associated regions. This is consistent with previous work showing that dietary methionine restriction alters lipid metabolism in cancer cells [124].

Together, these results demonstrate that multimodal MSI enables spatial characterization of metabolic features associated with immune infiltration that are not captured by single-modality approaches. A limitation of this work is that the functional state of T cells could not be assessed, restricting interpretation of whether these metabolic features support or suppress T cell effector function. This limitation is addressed in the following chapter through integration of lipid imaging with markers of T cell exhaustion in human tumors.

Chapter 4: Applying a multimodal MSI workflow to a cohort of human ovarian cancer tissues

4.0 My Contributions

Madison Shiyuk performed all MALDI MSI-related experiments and data analysis. Human tumor tissues were provided by Biospecimen and Biobanking Research Services (BBRS) at BC Cancer (Victoria, BC).

4.1 Chapter Introduction

Metabolic interactions between cancer cells and infiltrating immune cells play a central role in shaping anti-tumor immunity and are increasingly recognized as contributors to immunotherapy resistance in ovarian cancer. Consistent with this, clinical responses to immunotherapy for ovarian cancer remain limited, suggesting that features of the TME suppress effective anti-tumor immunity [29]. Within the TME, cancer cells can inhibit immune responses through multiple metabolic mechanisms. These include competition for essential nutrients [40,44], accumulation of immunosuppressive metabolites such as lactate [46], and the development of metabolically stressful conditions such as hypoxia [45]. Tumor tissues are also metabolically heterogeneous, and distinct metabolic niches within the TME may differentially influence immune cell recruitment, persistence, and functional state [30,125]. However, localized metabolic environments that affect T cell infiltration and activation remain incompletely understood.

Spatially resolved analytical approaches enable investigation of how metabolic heterogeneity within tumors correlates with immune cell localization [59,126]. Sequential application of MALDI

MSI and MALDI IHC enables detection of complementary molecular classes (*e.g.* lipids and proteins), that cannot be captured using a single modality. In this chapter, I apply multimodal MSI to human ovarian cancer tissues to determine how spatial metabolic features relate to T cell infiltration within the TME.

4.2 Methods

4.2.1 Human tissue

Human high-grade serous ovarian carcinoma (HGSC) tumor tissues were obtained through the Biobanking and Biospecimen Research Services (BBRS) program at the BC Cancer Deeley Research Centre. All tissue use was conducted under the University of Victoria Human Research Ethics Board approval (H25-0065).

Tumors were selected based on TIL status (high *vs.* low), as determined by prior tissue microarray analysis performed by BBRS (BC Cancer) using markers for CD79α, PAX5, CD3, and CD8. These markers were used to classify tumors according to their level of immune infiltration.

4.2.2 Cryosectioning and sample preparation

Tumors embedded in OCT were mounted onto a chuck using OCT (Thermo Fisher Scientific, Cat. No. 4585) and sectioned at 10 µm thickness using a using a CM1950 cryostat (Leica Biosystems). Chamber and specimen head temperatures were set to -20°C and -20°C, respectively. A C35 microtome blade (Feather, Cat. No. 24070549) was used for sectioning. Six serial sections were collected from each tissue and thaw-mounted (3 minutes) onto ITO slides (Delta Technologies LLC, Cat. No. CB- 901N-S111) for MALDI analysis or Superfrost™ Plus slides (Thermo Fisher Scientific, Cat. No. 1255015) for nanoDESI or immunofluorescence. To minimize contamination from OCT embedding medium, tissues were manipulated using a brush

rather than with the aid of an anti-roll plate. Sectioned tissues were dried in a nitrogen desiccator cabinet for 1 hour, vacuum sealed, and stored at -80°C until further analysis.

4.2.3 MALDI MSI lipidomics

One section from each tissue (n = 20) was thawed to room temperature for 1 hour in a nitrogen desiccator cabinet. A SPLASH ™ LIPIDOMIX ™ Mass Spec Standard (0.5 µL; Sigma Aldrich, Cat. No. 330707) was spotted onto each slide as a quality control and dried under vacuum for 10 minutes. Norharmane matrix was applied as described in **Supplementary Table 1**.

All tissues were imaged using a timsTOF *flex* MALDI-2 instrument (Bruker) in negative ion polarity with a 50 µm step size over the mass range *m/z* 200-2,500. Laser settings (SmartBeam, Bruker) were 500 shots per pixel, 10,000 Hz frequency, and 10.0 µs post-ionization delay. Trapped ion mobility separation (TIMS) was applied over a mobility range of $1/_{K0}$ 0.88 - 1.90 $V \cdot s/cm^2$, with a ramp time of 200 ms, accumulation time of 48.1 ms, and ramp rate of 4.85 Hz. The electric field gradient was defined by ramp voltages of Δt1 = 20.0 V, Δt2 = 120.0 V, Δt3 = -70.0V, Δt4 = -100.0 V, Δt5 = 0.0V, and Δt6 = -100.0 V. Mass analyzer parameters were optimized to maximize ion transmission, with funnel RF amplitudes of 350 Vpp (Funnel 1), 500 Vpp (Funnel 2), and 500 Vpp (multipole), quadrupole ion energy of 5.0 eV, and pre-TOF focus was set to a 150 µs transfer time and 15 µs pre-pulse storage. External calibration for mobility and *m/z* was performed prior to data acquisition using an ESI-L low concentration tuning mix (Agilent Technologies, Cat. No. G1969-85000). Online calibration during acquisition used norharmane (*m/z* 515.1620), PI-(38:4) (*m/z* 885.5497), CL-(72:8) (*m/z* 1447.9650), and CL-(72:7) (*m/z* 1449.9806).

4.2.4 MALDI immunohistochemistry

Following acquisition with MALDI MSI, tissues were subjected to a MALDI IHC workflow as previously described (**Chapter 3.2.6**) [107]. Miralys™ antibody probes (AmberGen) were applied for the following targets and concentrations: CD8α (4 µg/ mL), CD4 (4 µg/mL), PD-1 (4 µg/mL), CA9 (2 µg/mL), and GLUT-1 (2 µg/mL). Antibody catalogue and lot numbers are provided in **Supplementary Table 5**. An HTX M5 sprayer (HTX Technologies, LLC) was used to apply CHCA matrix as described in **Supplementary Table 1**, followed by recrystallization in vapour from 5% isopropanol at 60 °C for 75 seconds. Slides were imaged using a timsTOF *flex* MALDI-2 instrument (Bruker Daltonics) as described in **Chapter 3.2.7.3.** Online calibration was performed using PC-MT™ ions (CA9: *m/z* 1178.61; and GLUT-1: *m/z* 856.56) as reference masses, as matrix and endogenous background ions were not present in the acquired mass range.

4.2.5 Post-MALDI IHC H&E staining

Following imaging of PC-MTs™, hematoxylin and eosin staining was performed on tissues as described in **Chapter 2.2.8**. Brightfield optical images were obtained at 20x magnification using an Aperio Versa scanner (Leica Biosystems).

4.2.6 Data analysis

4.2.6.1 Reproducibility of MALDI IHC

Data from three serial sections of the same tissue were subjected to MALDI IHC. Resulting datasets were imported into SCiLS Lab™ and normalized to RMS. Mean signal intensities of

PC-MT™ reporter ions for GLUT-1 and CA9 were exported for each tumor. Extracted intensities were imported into GraphPad Prism for visualization. Reproducibility of protein detection across serial sections was assessed by comparing RMS-normalized intensities using scatter plots.

4.2.6.2 Lipid feature finding and annotation

Lipid imaging datasets were imported into SCiLS Lab™ and normalized to TIC prior to feature finding and downstream analyses. Lipid feature finding was performed using the T-REX^3 algorithm enabled by TIMS. Detection parameters included 2 x 2 spatial averaging, a minimum spatial coverage threshold of 5%, a relative intensity threshold of 0.1%, an *m/z* interval width of ± 10 ppm, and a collision cross section (CCS) mobility interval width of 2.00 ± Å^2. Feature detection was limited to a maximum of 5,000 features, resulting in 4,988 detected spectral features. Lipid annotations were assigned using MetaboScape® (Bruker) employing the MCube Lipid Species annotation workflow. Molecular assignments were based on accurate mass (*m/z*) matching, isotopic distribution fitting, and CCS. A total of 257 features were annotated (5.1%) and used for subsequent segmentation and region-based analyses.

4.2.6.3 Lipid spatial segmentation and region definition

Unsupervised spatial analysis was performed in SCiLS Lab™ using bisecting k-means clustering with weak spatial denoising. Segmentation was restricted to annotated lipid features (n = 257; **Chapter 4.2.6.2**), and pixels were grouped based on similarity in lipid expression profiles.

Segmentation-derived regions were saved as regions and exported as SCiLS export files (.sef) for downstream analyses.

4.2.6.4 Quantification and statistical analysis of segmentation regions

The proportion of each tumor represented by segmentation Regions 1-3 (**Chapter 4.2.6.3**) was quantified in SCiLS Lab™ based on the number of pixels assigned to each region. For each tumor, the fractional area represented by each region was calculated as:

$$\text{Regional fraction} = \frac{\text{Number of mass spectra in region}}{\text{Number of mass spectra in the entire tumor}}$$

Tumors were treated as independent biological replicates and stratified into high-TIL (n = 10) and low-TIL (n = 10) groups based on prior TMA analysis (**Chapter 4.2.1**). Fractions of tumors represented by each region were exported to GraphPad Prism for statistical analysis and visualization. Region composition for each tumor was visualized using 100% stacked bar plots. Differences in the fraction of tumor area occupied by each region between high- and low-TIL tumors were assessed using two-tailed, unpaired Mann-Whitney tests. Statistical significance was denoted as * $p < 0.05$ and ** $p < 0.01$.

4.2.6.5 Identification and visualization of region-associated lipids

Lipids associated with segmentation regions (Regions 1-3; **Chapter 4.2.6.3**) were identified using the SCiLS Lab™ “Find Values Co-Localized to Regions” function, restricted to annotated

lipid features (n = 257; **Chapter 4.2.6.2**). Lipids were considered region-associated and were retained for visualization if they exhibited a co-localization score ≥ 0.5.

For heatmap visualization, mean intensities of the selected features (n = 39) were exported for each region across all tumors. Intensities were $\log_2$-transformed and z-score normalized across regions for each lipid according to:

$$z = \frac{(x - \mu)}{\sigma}$$

where x represents the $\log_2$-transformed intensity in each given region, μ is the mean intensity across regions, and σ is the standard deviation for intensities across all regions. Normalized values were visualized in a heatmap using GraphPad Prism.

4.2.6.6 Metabolic marker proteins enriched in segmentation regions

Protein marker distributions for CA9 and GLUT-1 within segmentation regions were evaluated using MALDI IHC datasets acquired from the same tissue sections used for lipid imaging. Signal intensities were normalized to RMS using SCiLS Lab™. Pixel-level intensities within segmentation regions were extracted using Cardinal [118] and analyzed using linear mixed-effects models, with region specified as a fixed effect and tumor included as a random intercept (*lme4*; **Chapter 3.2.13.5.2**) [119]. For comparison between the regions, overall significance was assessed using Type III analysis of variance with Satterthwaite's approximation (*lmerTest)* [120], followed by post-hoc pairwise comparisons using estimated marginal means with Tukey adjustment (*emmeans*) [127]. Across features, p-values (q-values) were adjusted using the BH FDR procedure (**Chapter 3.2.13.5.5**) [121]. Protein intensity data were visualized using box-and-whisker plots with individual tumor values overlaid (GraphPad Prism). Statistical significance was annotated only

for features meeting both a q-value < 0.05 and a fold-change threshold > 2 and was denoted with asterisk notation (* $p < 0.05$; **$p < 0.01$; *** $p < 0.001$; **** $p < 0.0001$).

4.2.6.7 Immune-region workflow

4.2.6.7.1 Definition of immune-associated regions

Regions enriched for CD8α only or for CD8α and PD-1 were defined using MALDI IHC data in SCiLS Lab™. Training regions representing high and low signal intensity were manually annotated based on ion images. To define CD8α-high regions, the color scale of the CD8α ion images was adjusted to display the upper 70% of signal only. Three training regions were created by selecting contiguous pixels within different tissues (total = 150 pixels). Complementary CD8α-low regions were annotated across tumors by selecting contiguous pixels with low CD8α signal intensity (lower 30% of signal). Training regions for high- and low-PD-1 signal were generated using the same workflow. Resulting regions were used to train a supervised pixel classifier using the Linear Discriminant Analysis (LDA) tool in SCiLS Lab™. For high-CD8α-low-PD-1 regions, positive pixels were defined based on mass spectral similarity high- CD8α and low-PD-1 training regions. For high-CD8α-PD-1 regions, positive pixels were defined based on similarity to high- CD8α and high-PD-1 training regions.

4.2.7.2 Statistical analysis of $CD8^+$ and $CD8^+PD\text{-}1^+$ pixels in segmentation regions

To assess differences in the abundances of $CD8^+$ and $CD8^+PD\text{-}1^+$ T cells within segmentation regions, generalized linear mixed-effects models (GLLMs) were applied to pixel count data in R using the *gllmTMB* package [128]. Models were fit using a negative binomial distribution with

region as a fixed effect and tumor as a random intercept. To account for differences in region sizes, the total number of pixels assigned to each segmentation region was included as an offset (log-transformed), thereby modelling T cell density within each region. Post hoc pairwise comparisons between regions were performed using estimated marginal means with Tukey adjustment (*emmeans*)[127], and statistical significance was defined as $q < 0.05$ following BH FDR correction [121].

4.3 Results

To investigate spatial relationships between metabolism and immune infiltration, high-grade serous ovarian carcinoma tumors were stratified by TIL status (high TIL: n = 10; low TIL: n = 10) based on prior tissue microarray analysis. Briefly, immunohistochemical markers for B and T cells, including CD79α, PAX5, CD3, and CD8 were used to determine TIL status (details in **Chapter 4.2.1**).

Tumors comprise multiple cell types with distinct lipid compositions, particularly within cellular membranes. Lipid MSI data were therefore acquired first and used for unsupervised spatial segmentation to delineate regions with distinct lipid profiles, which are indicative of underlying differences in cellular composition. Next, MALDI IHC was performed on the same tissue sections to enable spatial alignment of protein markers with lipid-defined regions. This allowed assessment of the distribution of tumor metabolism-associated proteins (CA9 and GLUT-1) within these regions. Finally, supervised segmentation of immune cell proteins detected by MALDI IHC was used to evaluate $CD8^+$ T cell infiltration and functional status across regions. This approach identified intratumoral regions likely representing distinct TME compartments.

4.3.1 Lipid-defined segmentation regions differ by TIL status

Unsupervised spatial segmentation of lipid features identified three major lipid-defined regions (Regions 1-3; **Figure 11A**). The proportion of each tumor occupied by Regions 1-3 varied substantially across tumors (**Figure 11B**). To assess differences by TIL status, the proportion of tumor area represented by each region was compared between high-TIL and low-TIL groups. Region 2 occupied a significantly greater proportion of high-TIL tumors, whereas Region 3

occupied a significantly greater proportion of low-TIL tumors (**Figure 11C & D**). No significant difference was observed in the proportion of tumor area represented by Region 1 between high-TIL and low-TIL tumors (**Supplementary Figure 4**).

Figure 11. *Tumor compositions of lipid-defined segmentation regions differ by TIL status.*

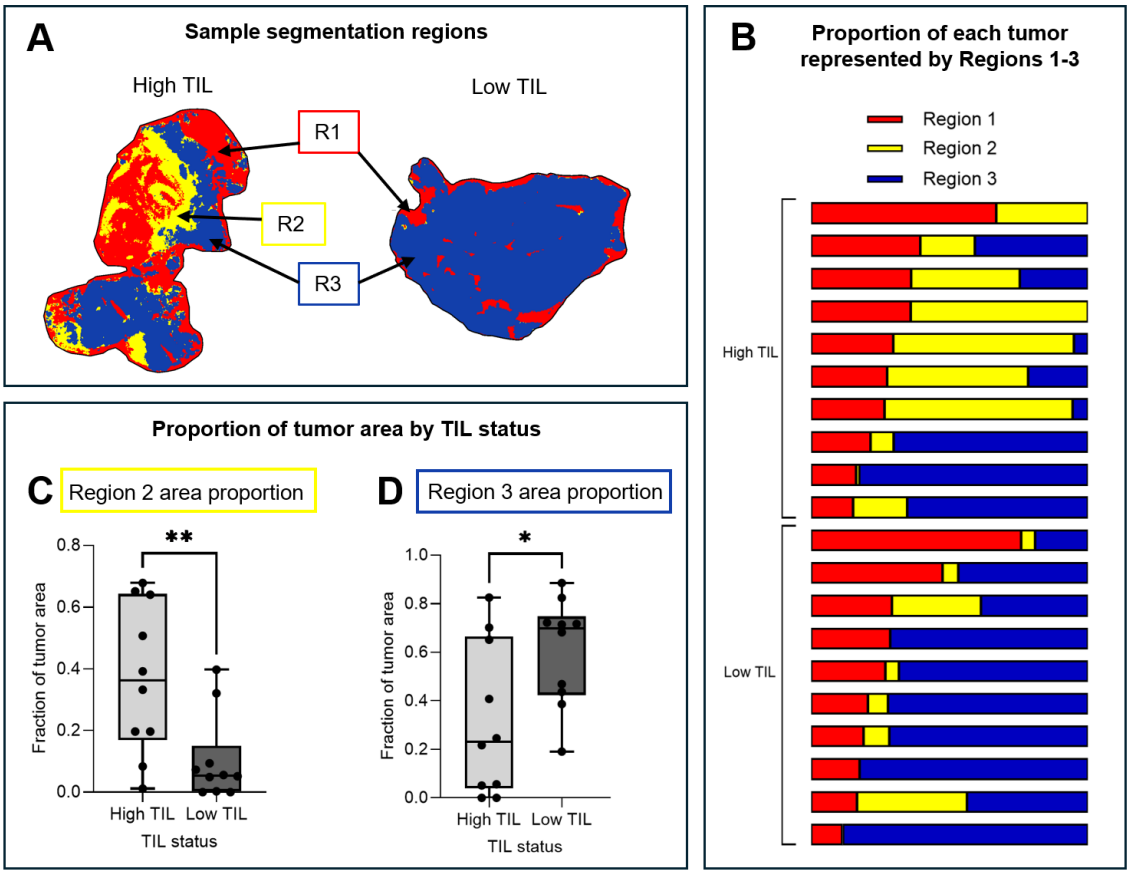

Unsupervised spatial segmentation based on lipid spectra identified three major regions (Regions 1-3) within tumors. **A.** Representative segmentation maps showing the spatial distributions of Regions 1-3. **B.** Region composition of individual tumors visualized as 100% stacked bar graphs showing the fraction of tumor area represented by each segmentation group. **C-D.** Proportion of high TIL (n = 10) and low TIL (n = 10) tumors represented by segmentation Regions 1-3. Tumor proportions represented by each region were calculated as the proportion of pixels within each region relative to the total number of pixels in the tumor. Differences between groups were assessed using two-tailed unpaired Mann-Whitney tests. Box-and-whisker plots show the median and interquartile range with whiskers extending to minimum and maximum values; individual tumors are shown as scatter points. Statistical significance is indicated by asterisks (*$p < 0.05$; **$p < 0.01$).

4.3.2 Molecular characterization of lipid-defined segmentation regions

To identify lipid species contributing to segmentation patterns, the lipid features that most strongly differentiated Regions 1-3 were identified using a co-localization analysis in SCiLS Lab™. Lipids exhibiting a co-localization score ≥0.5 were considered region-associated, and application of this threshold resulted in identification of 23 and 17 lipid features enriched in Regions 2 and 3, respectively. No features met this criterion for Region 1 (**Figure 12A**). Region 2 was enriched in multiple phospholipid classes, including PE, PS, and phosphatidylinositol (PI) (**Figure 12A**). Several of these lipid species may include 20:4 fatty acyl chains based on their total carbon and double bond compositions (*e.g.* PE-(40:4), PI-(38:4), PS-(38:4), and PS-(40:4)), although acyl chain composition cannot be definitively assigned without MS/MS (**Figure 12A**). Additionally, Region 3 was enriched in ceramide-1-phosphates (CerPs), phosphatidic acids (PAs), and PEs containing shorter fatty acyl chains such as PE-(32:0) and PE-(36:3) (**Figure 12A**).

To determine whether lipid-defined regions exhibited differential metabolic features, the distribution of protein markers detected with MALDI IHC were compared between these regions. The proteins CA9 and GLUT-1 were selected as markers of metabolic stress, as their expression is upregulated under conditions of hypoxia and increased glycolytic demand, respectively. Pixel-level intensities of CA9 and GLUT-1 were evaluated across Regions 1-3 using linear mixed-effects models with region as a fixed effect. Signal intensity of CA9 was significantly higher in Regions 2 and 3 compared to Region 1 (**Figure 12B**). Further, GLUT-1 was highest in region 3, followed by Regions 2 and 1, with all pairwise differences between regions reaching significance (**Figure 12C**).

Taken together, these analyses identified three regions with distinct molecular profiles. Region 2 was associated with PE, PI, and PS lipids including PS-(40:2) (**Figure 12D-F**). Region 3 was enriched in CerP, PA, and PE lipids, including PA-(32:1), and displayed the highest GLUT-1 signal (**Figure 12D-F**).

***Figure 12**. Lipids and proteins enriched in segmentation Regions 1-3.*

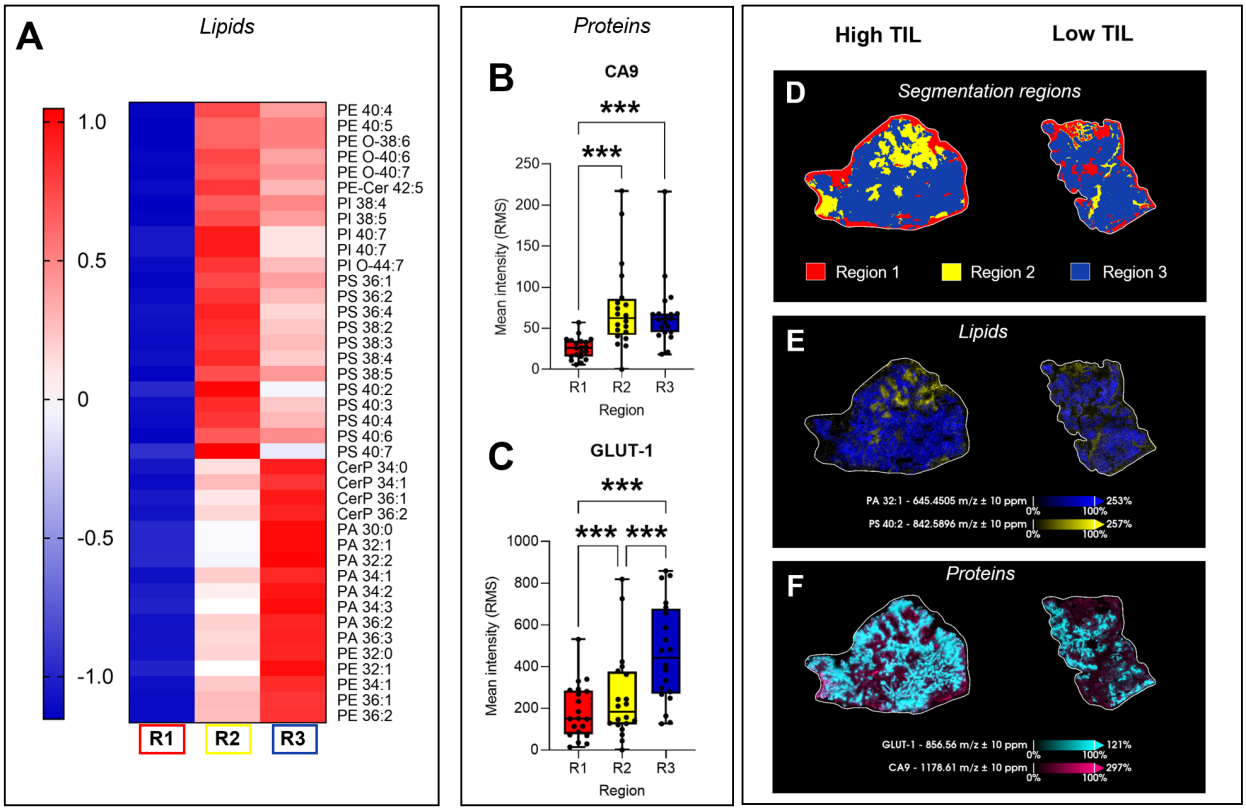

A. Lipids associated with segmentation Regions 1-3. Lipids identified with co-localization scores ≥ 0.5 following *Find Values Co-Localized to Regions* analysis in SCiLS Lab™ were considered region-associated. Mean intensities for the 39 lipids retained for analysis were $\log_2$-transformed and z-score normalized prior to visualization in a heatmap. **B-C.** Signal intensities of (**B**) CA9 and (**C**) GLUT-1 in regions 1-3. Statistical analysis was performed using linear mixed-effects models with post-hoc adjustments (Tukey) and BH FDR correction. **D-F** Representative images of (**D**) segmentation regions, (**E**) lipids enriched in Region 2 (PS-(40:2)) or Region 3 (PA-(32:1)), or (**F**) GLUT-1 and CA9.

4.3.3 $CD8^+$ and $CD8^+PD\text{-}1^+$ T cell abundances in segmentation regions

To assess $CD8^+$ T cell localization within lipid-defined regions, supervised pixel classification was used to identify pixels enriched for CD8α or co-localized CD8α and PD-1 signal, as detected with MALDI IHC (**Figure 13A**). The cell surface marker PD-1 is expressed on exhausted T cells and was thus used as a proxy for T cell exhaustion. Pixels with high CD8α signal were classified as regions with $CD8^+$ T cells, and pixels with high overlapping CD8α and PD-1 signal were classified as regions with $CD8^+PD\text{-}1^+$ T cells (**Figure 13A**).

The abundance of pixels containing $CD8^+$ and $CD8^+PD\text{-}1^+$ T cells within Regions 1-3 was quantified as the proportion of pixels assigned to each class within each region. Differences in the abundance of $CD8^+$ or $CD8^+PD\text{-}1^+$-containing pixels between regions were assessed using generalized linear mixed-effects models with an offset to account for region size, thereby modelling the prevalence of each pixel class within regions. Similar approaches have been applied in previous work, where mixed-effects models were used to assess differences in feature detection across spatial units (*e.g.* pixel-level presence/absence)[129]. In MSI datasets, individual pixels represent discrete sampling units; thus, the proportion of pixels assigned to a given class reflects its spatial prevalence. Regions 2 and 3 had significant enrichment of pixels containing $CD8^+$ cells relative to Region 1 (**Figure 13B**). Region 3 was significantly enriched in pixels containing $CD8^+PD\text{-}1^+$ T cells relative to both Regions 1 and 2 (**Figure 13B**).

These findings indicate that Regions 1-3 represent distinct tumor compartments. Region 1 exhibited comparatively low metabolic and immune signal relative to Regions 2 and 3 (**Figure 14**). Region 2 was characterized by elevated CA9 and GLUT-1 relative to Region 1 and was

enriched in phospholipids (PI, PE, and PS), alongside increased $CD8^+$ pixel prevalence (**Figure 14**). In contrast, Region 3 displayed the highest GLUT-1 abundance and was enriched in signalling lipids, including CerP and PA, as well as increased $CD8^+PD\text{-}1^+$ pixel prevalence (**Figure 14**). Together, these findings suggest that lipid-defined regions correspond to spatial niches with distinct metabolic profiles and differences in T cell infiltration and functional state.

Figure 13. *Prevalence of pixels containing CD8+ and CD8+PD-1+ T cells within segmentation regions.*

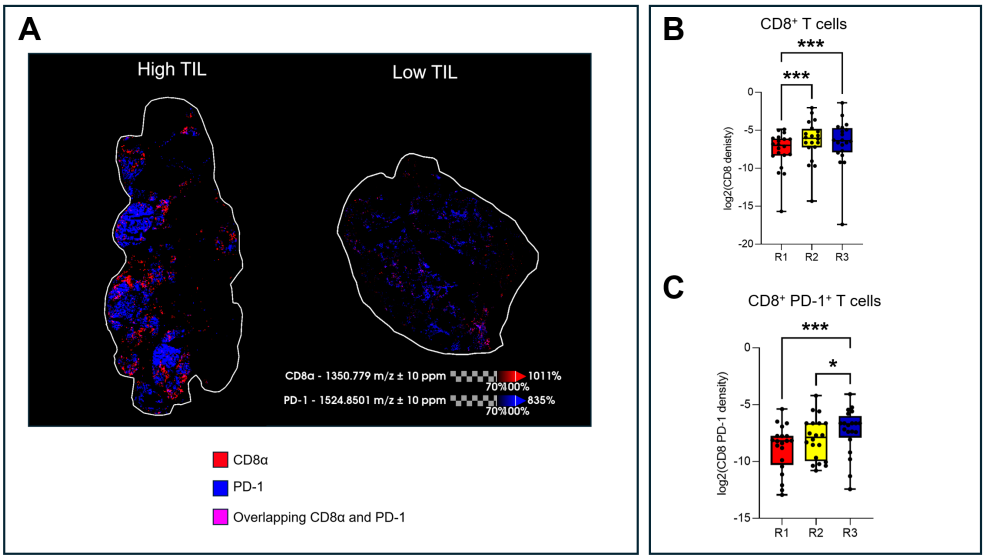

A. Representative ion images showing CD8α, PD-1, or overlapping CD8α and PD-1 signal used to classify pixels containing $CD8^+$ and $CD8^+PD\text{-}1^+$ T cells by supervised classification in SCiLS Lab™. Pixels with CD8α signal alone were classified as $CD8^+$, and pixels with overlapping CD8α and PD-1 signal were classified $CD8^+PD\text{-}1^+$. **B-C.** Quantification $CD8^+$ (**B**) and (**C**) $CD8^+PD\text{-}1^+$ pixel prevalence across lipid-defined segmentation regions (Regions 1-3). Prevalence was defined as the proportion of pixels assigned to each class within each region, as determined using generalized linear mixed-effects models with a negative binomial distribution. Region was included as a fixed effect, and tumor as a random intercept, with region size included as a log-transformed offset. Post-hoc pairwise comparisons (Tukey) were performed and resulting p-values were adjusted for multiple comparisons using the BH FDR procedure.

Figure 14. *Summary of molecules enriched in lipid-defined segmentation regions.*

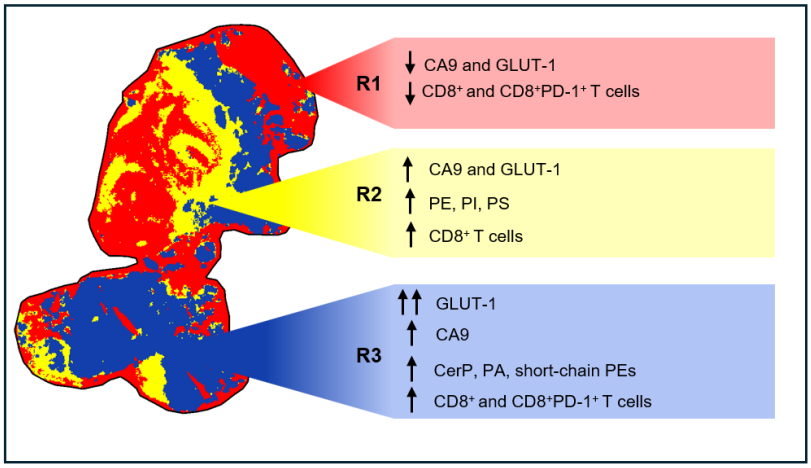

4.4 Chapter Discussion

This chapter investigated spatial metabolic heterogeneity in human ovarian tumors and its relationship to $CD8^+$ T cell infiltration and functional state. Unsupervised spatial segmentation of lipid MSI data identified three regions that differed in prevalence between high- and low-TIL tumors, indicating that spatial metabolic organization is linked to immune infiltration at the tumor level.

These regions appeared to reflect biologically distinct TMEs. Compared to Regions 2 and 3, Region 1 showed limited association with features of tumor-associated metabolic reprogramming and immune engagement. These findings suggest that Region 1 represents a compartment distinct from malignant tumor regions, consistent with prior work demonstrating increased metabolic activity and altered lipid profiles in tumor relative to surrounding tissue [130].

Region 2 is consistent with an immune-infiltrated tumor niche. Although CA9 is typically associated with hypoxia-driven immunosuppression, hypoxia can also promote immune cell recruitment through HIF-1α-dependent signalling, potentially explaining the coexistence of CA9 and increased $CD8^+$ pixel prevalence [45,131]. Enrichment of phospholipids, particularly those likely containing arachidonic acid, aligns with previous reports of spatial accumulation of arachidonic acid-containing phospholipids in tumors [132]. Together, these features are consistent with a metabolically active environment that remains permissive to T cell infiltration.

In contrast, Region 3 appears to represent a metabolically competitive and potentially immunosuppressive niche. Elevated GLUT-1 suggests increased glucose uptake by tumor cells,

which has been linked competition for nutrients between cancer cells and T cells [40,42]. Enrichment of $CD8^+PD\text{-}1^+$ pixels in this region is consistent with this interpretation, as glucose deprivation can contribute to T cell exhaustion [44]. The lipid profile of Region 3, including CerP and PA species, further suggests increased membrane remodelling and signalling activity [133,134]. Ceramide-1-phosphates can activate cytosolic phospholipase A2 to promote arachidonic acid release and downstream eicosanoid production [56,134], and eicosanoids such as prostaglandin E2 can promote T cell exhaustion [57,131]. These features suggest that Region 2 represents a microenvironment in which metabolic and lipid signalling pathways may contribute to T cell dysfunction.

Several limitations should be considered. Expression of PD-1 was used as a proxy for T cell exhaustion, although it may be transiently expressed during T cell activation [135]. Further, MSI measurements capture signals from multiple neighbouring pixels and therefore cannot resolve T cells from other cells. Lipid annotations were based on accurate mass and TIMS measurements rather than MS/MS, limiting structural confirmation, particularly for fatty acyl chains. In addition, histological annotation is required to define the cellular composition of the regions investigated in this study. Finally, these analyses identify spatial associations but do not establish causal relationships between metabolic features and immune function.

Overall, these findings demonstrate that lipid-defined spatial organization in ovarian tumors corresponds to distinct metabolic and immune microenvironments. These results highlight the utility of spatial metabolomics for resolving TME heterogeneity and provide a framework for investigating how metabolic features influence anti-tumor immunity.

Chapter 5: Concluding Remarks

Tumor metabolism plays a critical role in shaping anti-tumor immune responses, yet the spatial relationships between metabolite gradients and immune cell localization remain incompletely understood. This thesis developed and applied MSI workflows to investigate how metabolic features of the TME relate to TILs.

Optimization of MALDI MSI workflows enabled improved detection of metabolites that are typically challenging to detect with this modality. Integration of nanoDESI MSI, MALDI MSI, and MALDI IHC within a multimodal workflow demonstrated feasibility of sequential metabolite, lipid, and protein imaging. Application of multimodal imaging workflows revealed distinct metabolic niches associated with immune infiltration.

Collectively, this work demonstrates that multimodal MSI workflows provide a powerful framework for resolving the metabolic architecture of tumors and its association with immune infiltration. By enabling integration of metabolic and immune features within intact tissues, these approaches offer new opportunities to investigate mechanisms of tumor immunoregulation. Future studies incorporating higher spatial resolution, expanded immune profiling, and functional perturbations will further define how metabolic pathways influence anti-tumor immunity and may inform development of immunotherapeutic strategies.

References

1. Ovarian cancer statistics | Canadian Cancer Society. https://cancer.ca/en/cancer-information/cancer-types/ovarian/statistics (27 Jan. 2026, date last accessed).

2. Cancer statistics at a glance. Canadian Cancer Society. https://cancer.ca/en/research/cancer-statistics/cancer-statistics-at-a-glance (26 Oct. 2023, date last accessed).

3. Cancer Today. https://gco.iarc.who.int/today/en/dataviz/bars?mode=cancer&group_populations=1&types=0_1&sort_by=value1&populations=124&multiple_populations=0&values_position=out (4 Feb. 2026, date last accessed).

4. Goff BA, Mandel L, Muntz HG *et al.* Ovarian carcinoma diagnosis: Results of a national ovarian cancer survey. *Cancer* 2000;**89**(10):2068–75. https://doi.org/10.1002/1097-0142(20001115)89:10<2068::AID-CNCR6>3.0.CO;2-Z.

5. Caruso G, Weroha SJ, Cliby W. Ovarian Cancer: A Review. *JAMA* 2025;**334**(14):1278. https://doi.org/10.1001/jama.2025.9495.

6. Torre LA, Trabert B, DeSantis CE *et al.* Ovarian cancer statistics, 2018. *CA Cancer J Clin* 2018;**68**(4):284–96. https://doi.org/10.3322/caac.21456.

7. Lawrie TA, Winter-Roach BA, Heus P *et al.* Adjuvant (post-surgery) chemotherapy for early stage epithelial ovarian cancer. *Cochrane Database Syst Rev* 2015;**2016**(9). https://doi.org/10.1002/14651858.CD004706.pub5.

8. Trimbos B, Timmers P, Pecorelli S *et al.* Surgical Staging and Treatment of Early Ovarian Cancer: Long-term Analysis From a Randomized Trial. *JNCI J Natl Cancer Inst* 2010;**102**(13):982–7. https://doi.org/10.1093/jnci/djq149.

9. Bristow RE, Tomacruz RS, Armstrong DK *et al.* Survival Effect of Maximal Cytoreductive Surgery for Advanced Ovarian Carcinoma During the Platinum Era: A Meta-Analysis. *J Clin Oncol* 2023;**41**(25):4065–76. https://doi.org/10.1200/JCO.22.02765.

10. González-Martín A, Harter P, Leary A *et al.* Newly diagnosed and relapsed epithelial ovarian cancer: ESMO Clinical Practice Guideline for diagnosis, treatment and follow-up. *Ann Oncol* 2023;**34**(10):833–48. https://doi.org/10.1016/j.annonc.2023.07.011.

11. Fagotti A, Ferrandina MG, Vizzielli G *et al.* Randomized trial of primary debulking surgery versus neoadjuvant chemotherapy for advanced epithelial ovarian cancer (SCORPION-NCT01461850). *Int J Gynecol Cancer* 2020;**30**(11):1657–64. https://doi.org/10.1136/ijgc-2020-001640.

12. McGuire WP, Hoskins WJ, Brady MF *et al.* Cyclophosphamide and Cisplatin Compared with Paclitaxel and Cisplatin in Patients with Stage III and Stage IV Ovarian Cancer. *N Engl J Med* 1996;**334**(1):1–6. https://doi.org/10.1056/NEJM199601043340101.

13. Perren TJ, Swart AM, Pfisterer J *et al.* A Phase 3 Trial of Bevacizumab in Ovarian Cancer. *N Engl J Med* 2011;**365**(26):2484–96. https://doi.org/10.1056/NEJMoa1103799.

14. Burger RA, Brady MF, Bookman MA *et al.* Incorporation of Bevacizumab in the Primary Treatment of Ovarian Cancer. *N Engl J Med* 2011;**365**(26):2473–83. https://doi.org/10.1056/NEJMoa1104390.

15. Liu S, Kasherman L, Fazelzad R *et al.* The use of bevacizumab in the modern era of targeted therapy for ovarian cancer: A systematic review and meta-analysis. *Gynecol Oncol* 2021;**161**(2):601–12. https://doi.org/10.1016/j.ygyno.2021.01.028.

16. Ray-Coquard I, Leary A, Pignata S *et al.* Olaparib plus bevacizumab first-line maintenance in ovarian cancer: final overall survival results from the PAOLA-1/ENGOT-ov25 trial. *Ann Oncol* 2023;**34**(8):681–92. https://doi.org/10.1016/j.annonc.2023.05.005.

17. Li N, Zhu J, Yin R *et al.* Treatment With Niraparib Maintenance Therapy in Patients With Newly Diagnosed Advanced Ovarian Cancer: A Phase 3 Randomized Clinical Trial. *JAMA Oncol* 2023;**9**(9):1230. https://doi.org/10.1001/jamaoncol.2023.2283.

18. DiSilvestro P, Banerjee S, Colombo N *et al.* Overall Survival With Maintenance Olaparib at a 7-Year Follow-Up in Patients With Newly Diagnosed Advanced Ovarian Cancer and a BRCA Mutation: The SOLO1/GOG 3004 Trial. *J Clin Oncol* 2023;**41**(3):609–17. https://doi.org/10.1200/JCO.22.01549.

19. Monk BJ, Barretina-Ginesta MP, Pothuri B *et al.* Niraparib first-line maintenance therapy in patients with newly diagnosed advanced ovarian cancer: final overall survival results from the PRIMA/ENGOT-OV26/GOG-3012 trial. *Ann Oncol* 2024;**35**(11):981–92. https://doi.org/10.1016/j.annonc.2024.08.2241.

20. Konstantinopoulos PA, Ceccaldi R, Shapiro GI *et al.* Homologous Recombination Deficiency: Exploiting the Fundamental Vulnerability of Ovarian Cancer. *Cancer Discov* 2015;**5**(11):1137–54. https://doi.org/10.1158/2159-8290.CD-15-0714.

21. Wang D, Lippard SJ. Cellular processing of platinum anticancer drugs. *Nat Rev Drug Discov* 2005;**4**(4):307–20. https://doi.org/10.1038/nrd1691.

22. Galluzzi L, Senovilla L, Vitale I *et al.* Molecular mechanisms of cisplatin resistance. *Oncogene* 2012;**31**(15):1869–83. https://doi.org/10.1038/onc.2011.384.

23. Ledermann J, Kemp. Update on first-line treatment of advanced ovarian carcinoma. *Int J Womens Health* Jan. 2013:45. https://doi.org/10.2147/IJWH.S30231.

24. Matsuo K, Bond VK, Eno ML *et al.* Low drug resistance to both platinum and taxane chemotherapy on an *in vitro* drug resistance assay predicts improved survival in patients with advanced epithelial ovarian, fallopian and peritoneal cancer. *Int J Cancer* 2009;**125**(11):2721–7. https://doi.org/10.1002/ijc.24654.

25. Matsuo K, Eno ML, Im DD *et al.* Clinical relevance of extent of extreme drug resistance in epithelial ovarian carcinoma. *Gynecol Oncol* 2010;**116**(1):61–5. https://doi.org/10.1016/j.ygyno.2009.09.018.

26. Baert T, Ferrero A, Sehouli J *et al.* The systemic treatment of recurrent ovarian cancer revisited. *Ann Oncol* 2021;**32**(6):710–25. https://doi.org/10.1016/j.annonc.2021.02.015.

27. Pujade-Lauraine E, Hilpert F, Weber B *et al.* Bevacizumab Combined With Chemotherapy for Platinum-Resistant Recurrent Ovarian Cancer: The AURELIA Open-Label Randomized Phase III Trial. *J Clin Oncol* 2014;**32**(13):1302–8. https://doi.org/10.1200/JCO.2013.51.4489.

28. Sato E, Olson SH, Ahn J *et al.* Intraepithelial CD8+ tumor-infiltrating lymphocytes and a high CD8+/regulatory T cell ratio are associated with favorable prognosis in ovarian cancer. *Proc Natl Acad Sci* 2005;**102**(51):18538–43. https://doi.org/10.1073/pnas.0509182102.

29. Matulonis UA, Shapira-Frommer R, Santin AD *et al.* Antitumor activity and safety of pembrolizumab in patients with advanced recurrent ovarian cancer: results from the phase II KEYNOTE-100 study. *Ann Oncol* 2019;**30**(7):1080–7. https://doi.org/10.1093/annonc/mdz135.

30. Yang B, Li X, Zhang W *et al.* Spatial heterogeneity of infiltrating T cells in high-grade serous ovarian cancer revealed by multi-omics analysis. *Cell Rep Med* 2022;**3**(12):100856. https://doi.org/10.1016/j.xcrm.2022.100856.

31. Huang RY, Eppolito C, Lele S *et al.* LAG3 and PD1 co-inhibitory molecules collaborate to limit CD8+ T cell signaling and dampen antitumor immunity in a murine ovarian cancer model. *Oncotarget* 2015;**6**(29):27359–77. https://doi.org/10.18632/oncotarget.4751.

32. Rolland P, Deen S, Scott I *et al.* Human Leukocyte Antigen Class I Antigen Expression Is an Independent Prognostic Factor in Ovarian Cancer. *Clin Cancer Res* 2007;**13**(12):3591–6. https://doi.org/10.1158/1078-0432.CCR-06-2087.

33. Han LY, Fletcher MS, Urbauer DL *et al.* HLA Class I Antigen Processing Machinery Component Expression and Intratumoral T-Cell Infiltrate as Independent Prognostic Markers in Ovarian Carcinoma. *Clin Cancer Res* 2008;**14**(11):3372–9. https://doi.org/10.1158/1078-0432.CCR-07-4433.

34. Qian F, Liao J, Villella J *et al.* Effects of 1-methyltryptophan stereoisomers on IDO2 enzyme activity and IDO2-mediated arrest of human T cell proliferation. *Cancer Immunol Immunother* 2012;**61**(11):2013–20. https://doi.org/10.1007/s00262-012-1265-x.

35. Caneba CA, Yang L, Baddour J *et al.* Nitric oxide is a positive regulator of the Warburg effect in ovarian cancer cells. *Cell Death Dis* 2014;**5**(6):e1302–e1302. https://doi.org/10.1038/cddis.2014.264.

36. Yuan L, Sheng X, Willson AK *et al.* Glutamine promotes ovarian cancer cell proliferation through the mTOR/S6 pathway. *Endocr Relat Cancer* 2015;**22**(4):577–91. https://doi.org/10.1530/ERC-15-0192.

37. Sakaguchi S, Wing K, Onishi Y *et al.* Regulatory T cells: how do they suppress immune responses? *Int Immunol* 2009;**21**(10):1105–11. https://doi.org/10.1093/intimm/dxp095.

38. Curiel TJ, Coukos G, Zou L *et al.* Specific recruitment of regulatory T cells in ovarian carcinoma fosters immune privilege and predicts reduced survival. *Nat Med* 2004;**10**(9):942–9. https://doi.org/10.1038/nm1093.

39. Wherry EJ. T cell exhaustion. *Nat Immunol* 2011;**12**(6):492–9. https://doi.org/10.1038/ni.2035.

40. Chang CH, Qiu J, O'Sullivan D *et al.* Metabolic Competition in the Tumor Microenvironment Is a Driver of Cancer Progression. *Cell* 2015;**162**(6):1229–41. https://doi.org/10.1016/j.cell.2015.08.016.

41. Freeman GJ, Long AJ, Iwai Y *et al.* Engagement of the Pd-1 Immunoinhibitory Receptor by a Novel B7 Family Member Leads to Negative Regulation of Lymphocyte Activation. *J Exp Med* 2000;**192**(7):1027–34. https://doi.org/10.1084/jem.192.7.1027.

42. Xintaropoulou C, Ward C, Wise A *et al.* Expression of glycolytic enzymes in ovarian cancers and evaluation of the glycolytic pathway as a strategy for ovarian cancer treatment. *BMC Cancer* 2018;**18**(1):636. https://doi.org/10.1186/s12885-018-4521-4.

43. Fong MY, McDunn J, Kakar SS. Identification of Metabolites in the Normal Ovary and Their Transformation in Primary and Metastatic Ovarian Cancer. *PLoS ONE* 2011;**6**(5):e19963. https://doi.org/10.1371/journal.pone.0019963.

44. Cham CM, Driessens G, O'Keefe JP *et al.* Glucose deprivation inhibits multiple key gene expression events and effector functions in CD8 $^{+}$ T cells. *Eur J Immunol* 2008;**38**(9):2438–50. https://doi.org/10.1002/eji.200838289.

45. Swietach P, Vaughan-Jones RD, Harris AL. Regulation of tumor pH and the role of carbonic anhydrase 9. *Cancer Metastasis Rev* 2007;**26**(2):299–310. https://doi.org/10.1007/s10555-007-9064-0.

46. Fischer K, Hoffmann P, Voelkl S *et al.* Inhibitory effect of tumor cell–derived lactic acid on human T cells. *Blood* 2007;**109**(9):3812–9. https://doi.org/10.1182/blood-2006-07-035972.

47. Bak SP, Alonso A, Turk MJ *et al.* Murine ovarian cancer vascular leukocytes require arginase-1 activity for T cell suppression. *Mol Immunol* 2008;**46**(2):258–68. https://doi.org/10.1016/j.molimm.2008.08.266.

48. Bündgen G, Ulges A, Pietruschka J *et al.* Polyamines regulate adaptive antitumor immunity by functional specialization of regulatory T cells. *Immunity* 2025;**58**(8):2019-2034.e11. https://doi.org/10.1016/j.immuni.2025.07.007.

49. Srivastava MK, Sinha P, Clements VK *et al.* Myeloid-Derived Suppressor Cells Inhibit T-Cell Activation by Depleting Cystine and Cysteine. *Cancer Res* 2010;**70**(1):68–77. https://doi.org/10.1158/0008-5472.CAN-09-2587.

50. Sanderson SM, Gao X, Dai Z *et al.* Methionine metabolism in health and cancer: a nexus of diet and precision medicine. *Nat Rev Cancer* 2019;**19**(11):625–37. https://doi.org/10.1038/s41568-019-0187-8.

51. Roy DG, Chen J, Mamane V *et al.* Methionine Metabolism Shapes T Helper Cell Responses through Regulation of Epigenetic Reprogramming. *Cell Metab* 2020;**31**(2):250-266.e9. https://doi.org/10.1016/j.cmet.2020.01.006.

52. DeVorkin L, Pavey N, Carleton G *et al.* Autophagy Regulation of Metabolism Is Required for CD8+ T Cell Anti-tumor Immunity. *Cell Rep* 2019;**27**(2):502-513.e5. https://doi.org/10.1016/j.celrep.2019.03.037.

53. Bian Y, Li W, Kremer DM *et al.* Cancer SLC43A2 alters T cell methionine metabolism and histone methylation. *Nature* 2020;**585**(7824):277–82. https://doi.org/10.1038/s41586-020-2682-1.

54. Zhao T, Lum JJ. Methionine cycle-dependent regulation of T cells in cancer immunity. *Front Oncol* 2022;**12**. https://www.frontiersin.org/journals/oncology/articles/10.3389/fonc.2022.969563.

55. Alavi S, Emran AA, Tseng HY *et al.* Nicotinamide Inhibits T Cell Exhaustion and Increases Differentiation of CD8 Effector T Cells. *Cancers* 2022;**14**(2):323. https://doi.org/10.3390/cancers14020323.

56. Balsinde J, Winstead MV, Dennis EA. Phospholipase A_2 regulation of arachidonic acid mobilization. *FEBS Lett* 2002;**531**(1):2–6. https://doi.org/10.1016/S0014-5793(02)03413-0.

57. Mahic M, Yaqub S, Johansson CC *et al.* FOXP3+CD4+CD25+ Adaptive Regulatory T Cells Express Cyclooxygenase-2 and Suppress Effector T Cells by a Prostaglandin E2-Dependent Mechanism. *J Immunol* 2006;**177**(1):246–54. https://doi.org/10.4049/jimmunol.177.1.246.

58. Costello PS, Gallagher M, Cantrell DA. Sustained and dynamic inositol lipid metabolism inside and outside the immunological synapse. *Nat Immunol* 2002;**3**(11):1082–9. https://doi.org/10.1038/ni848.

59. Sun C, Wang A, Zhou Y *et al.* Spatially resolved multi-omics highlights cell-specific metabolic remodeling and interactions in gastric cancer. *Nat Commun* 2023;**14**(1):2692. https://doi.org/10.1038/s41467-023-38360-5.

60. Caprioli RM, Farmer TB, Gile J. Molecular Imaging of Biological Samples: Localization of Peptides and Proteins Using MALDI-TOF MS. *Anal Chem* 1997;**69**(23):4751–60. https://doi.org/10.1021/ac970888i.

61. Karas Michael, Hillenkamp Franz. Laser desorption ionization of proteins with molecular masses exceeding 10,000 daltons. *Anal Chem* 1988;**60**(20):2299–301. https://doi.org/10.1021/ac00171a028.

62. Takáts Z, Wiseman JM, Gologan B *et al.* Mass Spectrometry Sampling Under Ambient Conditions with Desorption Electrospray Ionization. *Science* 2004;**306**(5695):471–3. https://doi.org/10.1126/science.1104404.

63. Shimma S, Furuta M, Ichimura K *et al.* Direct MS/MS analysis in mammalian tissue sections using MALDI-QIT-TOFMS and chemical inkjet technology. *Surf Interface Anal* 2006;**38**(12–13):1712–4. https://doi.org/10.1002/sia.2389.

64. Anderson DMG, Messinger JD, Patterson NH *et al.* Lipid Landscape of the Human Retina and Supporting Tissues Revealed by High-Resolution Imaging Mass Spectrometry. *J Am Soc Mass Spectrom* 2020;**31**(12):2426–36. https://doi.org/10.1021/jasms.0c00119.

65. Unsihuay D, Mesa Sanchez D, Laskin J. Quantitative Mass Spectrometry Imaging of Biological Systems. *Annu Rev Phys Chem* 2021;**72**(1):307–29. https://doi.org/10.1146/annurev-physchem-061020-053416.

66. Heijs B, Potthoff A, Soltwisch J *et al.* MALDI-2 for the Enhanced Analysis of *N* -Linked Glycans by Mass Spectrometry Imaging. *Anal Chem* 2020;**92**(20):13904–11. https://doi.org/10.1021/acs.analchem.0c02732.

67. Esteve C, Tolner EA, Shyti R *et al.* Mass spectrometry imaging of amino neurotransmitters: a comparison of derivatization methods and application in mouse brain tissue. *Metabolomics* 2016;**12**(2):30. https://doi.org/10.1007/s11306-015-0926-0.

68. Sun C, Li Z, Ma C *et al.* Acetone immersion enhanced MALDI-MS imaging of small molecule metabolites in biological tissues. *J Pharm Biomed Anal* 2019;**176**:112797. https://doi.org/10.1016/j.jpba.2019.112797.

69. Lu W, Park NR, TeSlaa T *et al.* Acidic Methanol Treatment Facilitates Matrix-Assisted Laser Desorption Ionization-Mass Spectrometry Imaging of Energy Metabolism. *Anal Chem* 2023;**95**(40):14879–88. https://doi.org/10.1021/acs.analchem.3c01875.

70. Yang H, Ji W, Guan M *et al.* Organic washes of tissue sections for comprehensive analysis of small molecule metabolites by MALDI MS imaging of rat brain following status epilepticus. *Metabolomics* 2018;**14**(4):50. https://doi.org/10.1007/s11306-018-1348-6.

71. Seeley EH, Oppenheimer SR, Mi D *et al.* Enhancement of protein sensitivity for MALDI imaging mass spectrometry after chemical treatment of tissue sections. *J Am Soc Mass Spectrom* 2008;**19**(8):1069–77. https://doi.org/10.1016/j.jasms.2008.03.016.

72. Wang HYJ, Liu CB, Wu HW. A simple desalting method for direct MALDI mass spectrometry profiling of tissue lipids. *J Lipid Res* 2011;**52**(4):840–9. https://doi.org/10.1194/jlr.D013060.

73. Angel PM, Spraggins JM, Baldwin HS *et al.* Enhanced Sensitivity for High Spatial Resolution Lipid Analysis by Negative Ion Mode Matrix Assisted Laser Desorption Ionization Imaging Mass Spectrometry. *Anal Chem* 2012;**84**(3):1557–64. https://doi.org/10.1021/ac202383m.

74. Hanton SD, Cornelio Clark PA, Owens KG. Investigations of matrix-assisted laser desorption/ionization sample preparation by time-of-flight secondary ion mass spectrometry. *J Am Soc Mass Spectrom* 1999;**10**(2):104–11. https://doi.org/10.1016/S1044-0305(98)00135-4.

75. Calvano CD, Monopoli A, Cataldi TRI *et al.* MALDI matrices for low molecular weight compounds: an endless story? *Anal Bioanal Chem* 2018;**410**(17):4015–38. https://doi.org/10.1007/s00216-018-1014-x.

76. Toue S, Sugiura Y, Kubo A *et al.* Microscopic imaging mass spectrometry assisted by on-tissue chemical derivatization for visualizing multiple amino acids in human colon cancer xenografts. *PROTEOMICS* 2014;**14**(7–8):810–9. https://doi.org/10.1002/pmic.201300041.

77. Merdas M, Lagarrigue M, Vanbellingen Q *et al.* On-tissue chemical derivatization reagents for matrix-assisted laser desorption/ionization mass spectrometry imaging. *J Mass Spectrom* 2021;**56**(10):e4731. https://doi.org/10.1002/jms.4731.

78. Shimbo K, Yahashi A, Hirayama K *et al.* Multifunctional and Highly Sensitive Precolumn Reagents for Amino Acids in Liquid Chromatography/Tandem Mass Spectrometry. *Anal Chem* 2009;**81**(13):5172–9. https://doi.org/10.1021/ac900470w.

79. Veličković Dušan, Zemaitis Kevin J., Bhattacharjee Arunima *et al.* Mass spectrometry imaging of natural carbonyl products directly from agar-based microbial interactions using 4-APEBA derivatization. *mSystems* 2023;**9**(1):e00803-23. https://doi.org/10.1128/msystems.00803-23.

80. Zemaitis KJ, Lin VS, Ahkami AH *et al.* Expanded Coverage of Phytocompounds by Mass Spectrometry Imaging Using On-Tissue Chemical Derivatization by 4-APEBA. *Anal Chem* 2023;**95**(34):12701–9. https://doi.org/10.1021/acs.analchem.3c01345.

81. Zenobi R, Knochenmuss R. Ion formation in MALDI mass spectrometry. *Mass Spectrom Rev* (Hoboken) 1998;**17**(5):337–66. https://doi.org/10.1002/(SICI)1098-2787(1998)17:5<337::AID-MAS2>3.0.CO;2-S.

82. Karas M, Krüger R. Ion Formation in MALDI: The Cluster Ionization Mechanism. *Chem Rev* 2003;**103**(2):427–40. https://doi.org/10.1021/cr010376a.

83. Luxembourg SL, McDonnell LA, Duursma MC *et al.* Effect of Local Matrix Crystal Variations in Matrix-Assisted Ionization Techniques for Mass Spectrometry. *Anal Chem* 2003;**75**(10):2333–41. https://doi.org/10.1021/ac026434p.

84. Gemperline E, Rawson S, Li L. Optimization and Comparison of Multiple MALDI Matrix Application Methods for Small Molecule Mass Spectrometric Imaging. *Anal Chem* 2014;**86**(20):10030–5. https://doi.org/10.1021/ac5028534.

85. Lu T, Freytag L, Narayana VK *et al.* Matrix Selection for the Visualization of Small Molecules and Lipids in Brain Tumors Using Untargeted MALDI-TOF Mass Spectrometry Imaging. *Metabolites* 2023;**13**(11):1139. https://doi.org/10.3390/metabo13111139.

86. Fu J, Gu J, Bao Z *et al.* 2,5-Dihydroxyterephthalic Acid: A Matrix for Improved Detection and Imaging of Amino Acids. *Anal Chem* 2023;**95**(51):18709–18. https://doi.org/10.1021/acs.analchem.3c01731.

87. Shroff R, Muck A, Svatoš A. Analysis of low molecular weight acids by negative mode matrix-assisted laser desorption/ionization time-of-flight mass spectrometry. *Rapid Commun Mass Spectrom* 2007;**21**(20):3295–300. https://doi.org/10.1002/rcm.3216.

88. Wang J, Qiu S, Chen S *et al.* MALDI-TOF MS Imaging of Metabolites with a N-(1-Naphthyl) Ethylenediamine Dihydrochloride Matrix and Its Application to Colorectal Cancer Liver Metastasis. *Anal Chem* 2015;**87**(1):422–30. https://doi.org/10.1021/ac504294s.

89. Liu H, Chen R, Wang J *et al.* 1,5-Diaminonaphthalene Hydrochloride Assisted Laser Desorption/Ionization Mass Spectrometry Imaging of Small Molecules in Tissues Following Focal Cerebral Ischemia. *Anal Chem* 2014;**86**(20):10114–21. https://doi.org/10.1021/ac5034566.

90. Leopold J, Prabutzki P, Engel KM *et al.* A Five-Year Update on Matrix Compounds for MALDI-MS Analysis of Lipids. *Biomolecules* 2023;**13**(3):546. https://doi.org/10.3390/biom13030546.

91. Eiersbrock FB, Orthen JM, Soltwisch J. Validation of MALDI-MS imaging data of selected membrane lipids in murine brain with and without laser postionization by quantitative nano-HPLC-MS using laser microdissection. *Anal Bioanal Chem* 2020;**412**(25):6875–86. https://doi.org/10.1007/s00216-020-02818-y.

92. Yang H, Jackson SN, Woods AS *et al.* Streamlined Analysis of Cardiolipins in Prokaryotic and Eukaryotic Samples Using a Norharmane Matrix by MALDI-MSI. *J Am Soc Mass Spectrom* 2020;**31**(12):2495–502. https://doi.org/10.1021/jasms.0c00201.

93. Westmacott G, Ens W, Hillenkamp F *et al.* The influence of laser fluence on ion yield in matrix-assisted laser desorption ionization mass spectrometry. *Int J Mass Spectrom* 2002;**221**(1):67–81. https://doi.org/10.1016/S1387-3806(02)00898-9.

94. Campbell JM, Vestal ML, Blank PS *et al.* Fragmentation of leucine enkephalin as a function of laser fluence in a MALDI TOF-TOF. *J Am Soc Mass Spectrom* 2007;**18**(4):607–16. https://doi.org/10.1016/j.jasms.2006.11.008.

95. Miller PE, Denton MB. The quadrupole mass filter: Basic operating concepts. *J Chem Educ* 1986;**63**(7):617. https://doi.org/10.1021/ed063p617.

96. Boesl U. Time-of-flight mass spectrometry: Introduction to the basics. *Mass Spectrom Rev* 2017;**36**(1):86–109. https://doi.org/10.1002/mas.21520.

97. Spraggins JM, Djambazova KV, Rivera ES *et al.* High-Performance Molecular Imaging with MALDI Trapped Ion-Mobility Time-of-Flight (timsTOF) Mass Spectrometry. *Anal Chem* 2019;**91**(22):14552–60. https://doi.org/10.1021/acs.analchem.9b03612.

98. Burnum-Johnson KE, Zheng X, Dodds JN *et al.* Ion mobility spectrometry and the omics: Distinguishing isomers, molecular classes and contaminant ions in complex samples. *TrAC Trends Anal Chem* 2019;**116**:292–9. https://doi.org/10.1016/j.trac.2019.04.022.

99. Hernandez DR, DeBord JD, Ridgeway ME *et al.* Ion dynamics in a trapped ion mobility spectrometer. *The Analyst* 2014;**139**(8):1913–21. https://doi.org/10.1039/C3AN02174B.

100. Soltwisch J, Heijs B, Koch A *et al.* MALDI-2 on a Trapped Ion Mobility Quadrupole Time-of-Flight Instrument for Rapid Mass Spectrometry Imaging and Ion Mobility Separation of Complex Lipid Profiles. *Anal Chem* 2020;**92**(13):8697–703. https://doi.org/10.1021/acs.analchem.0c01747.

101. Jiang L, Hilger RT, Laskin J. Hardware and software solutions for implementing nanospray desorption electrospray ionization (nano-DESI) sources on commercial mass spectrometers. *J Mass Spectrom* 2024;**59**(7):e5065. https://doi.org/10.1002/jms.5065.

102. Laskin J, Heath BS, Roach PJ *et al.* Tissue Imaging Using Nanospray Desorption Electrospray Ionization Mass Spectrometry. *Anal Chem* 2012;**84**(1):141–8. https://doi.org/10.1021/ac2021322.

103. Marques C, Friedrich F, Liu L *et al.* Global and Spatial Metabolomics of Individual Cells Using a Tapered Pneumatically Assisted nano-DESI Probe. *J Am Soc Mass Spectrom* 2023;**34**(11):2518–24. https://doi.org/10.1021/jasms.3c00239.

104. Duncan KD, Bergman HM, Lanekoff I. A pneumatically assisted nanospray desorption electrospray ionization source for increased solvent versatility and enhanced metabolite detection from tissue. *Analyst* 2017;**142**(18):3424–31. https://doi.org/10.1039/C7AN00901A.

105. Eberlin LS, Liu X, Ferreira CR *et al.* Desorption Electrospray Ionization then MALDI Mass Spectrometry Imaging of Lipid and Protein Distributions in Single Tissue Sections. *Anal Chem* 2011;**83**(22):8366–71. https://doi.org/10.1021/ac202016x.

106. Škrášková K, Claude E, Jones EA *et al.* Enhanced capabilities for imaging gangliosides in murine brain with matrix-assisted laser desorption/ionization and desorption electrospray ionization mass spectrometry coupled to ion mobility separation. *Methods* 2016;**104**:69–78. https://doi.org/10.1016/j.ymeth.2016.02.014.

107. Yagnik G, Liu Z, Rothschild KJ *et al.* Highly Multiplexed Immunohistochemical MALDI-MS Imaging of Biomarkers in Tissues. *J Am Soc Mass Spectrom* 2021;**32**(4):977–88. https://doi.org/10.1021/jasms.0c00473.

108. Lim MJ, Yagnik G, Henkel C *et al.* MALDI HiPLEX-IHC: multiomic and multimodal imaging of targeted intact proteins in tissues. *Front Chem* 2023;**11**. https://www.frontiersin.org/articles/10.3389/fchem.2023.1182404.

109. Shafer CC, Neumann EK. Optimized combination of MALDI MSI and immunofluorescence for neuroimaging of lipids within cellular microenvironments. *Front Chem* 2024;**12**:1334209. https://doi.org/10.3389/fchem.2024.1334209.

110. Pratavieira M, Silva Menegasso AR da, Roat T *et al.* In Situ Metabolomics of the Honeybee Brain: The Metabolism of l-Arginine through the Polyamine Pathway in the Proboscis Extension Response (PER). *J Proteome Res* 2020;**19**(2):832–44. https://doi.org/10.1021/acs.jproteome.9b00653.

111. Sezgin S, Hassan R, Zühlke S *et al.* Spatio-temporal visualization of the distribution of acetaminophen as well as its metabolites and adducts in mouse livers by MALDI MSI. *Arch Toxicol* 2018;**92**(9):2963–77. https://doi.org/10.1007/s00204-018-2271-3.

112. Eggink M, Wijtmans M, Kretschmer A *et al.* Targeted LC–MS derivatization for aldehydes and carboxylic acids with a new derivatization agent 4-APEBA. *Anal Bioanal Chem* 2010;**397**(2):665–75. https://doi.org/10.1007/s00216-010-3575-1.

113. Domon B, Costello CE. A systematic nomenclature for carbohydrate fragmentations in FAB-MS/MS spectra of glycoconjugates. *Glycoconj J* 1988;**5**(4):397–409. https://doi.org/10.1007/BF01049915.

114. Takeo E, Sugiura Y, Uemura T *et al.* Tandem Mass Spectrometry Imaging Reveals Distinct Accumulation Patterns of Steroid Structural Isomers in Human Adrenal Glands. *Anal Chem* 2019;**91**(14):8918–25. https://doi.org/10.1021/acs.analchem.9b00619.

115. Hung MH, Lee JS, Ma C *et al.* Tumor methionine metabolism drives T-cell exhaustion in hepatocellular carcinoma. *Nat Commun* 2021;**12**(1):1455. https://doi.org/10.1038/s41467-021-21804-1.

116. Lanekoff I, Heath BS, Liyu A *et al.* Automated Platform for High-Resolution Tissue Imaging Using Nanospray Desorption Electrospray Ionization Mass Spectrometry. *Anal Chem* 2012;**84**(19):8351–6. https://doi.org/10.1021/ac301909a.

117. Monaghan J, Nguyen K, Woytowich N *et al.* imzML Writer: An Easy-to-Use Python Pipeline for Conversion of Continuously Acquired Raw Mass Spectrometry Imaging Data to imzML Format. *Anal Chem* 2025;**97**(11):5932–7. https://doi.org/10.1021/acs.analchem.4c06520.

118. Bemis KD, Harry A, Eberlin LS *et al. Cardinal* : an R package for statistical analysis of mass spectrometry-based imaging experiments. *Bioinformatics* 2015;**31**(14):2418–20. https://doi.org/10.1093/bioinformatics/btv146.

119. Bates D, Mächler M, Bolker B *et al.* Fitting Linear Mixed-Effects Models Using **lme4**. *J Stat Softw* 2015;**67**(1). https://doi.org/10.18637/jss.v067.i01.

120. Kuznetsova A, Brockhoff PB, Christensen RHB. lmerTest Package: Tests in Linear Mixed Effects Models, Articles. *J Stat Softw* 2017;**82**(13):1–26. https://doi.org/10.18637/jss.v082.i13.

121. Benjamini Y, Hochberg Y. Controlling the False Discovery Rate: A Practical and Powerful Approach to Multiple Testing. *J R Stat Soc Ser B Stat Methodol* 1995;**57**(1):289–300. https://doi.org/10.1111/j.2517-6161.1995.tb02031.x.

122. Taylor AJ, Dexter A, Bunch J. Exploring Ion Suppression in Mass Spectrometry Imaging of a Heterogeneous Tissue. *Anal Chem* 2018;**90**(9):5637–45. https://doi.org/10.1021/acs.analchem.7b05005.

123. Suto R, Udono H, Yamamoto A *et al.* Effect of Accessory Cells on Stimulation of Murine T-Cell Leukemia with Antibodies to the CD3/T Cell Antigen Receptor Complex. *Jpn J Cancer Res* 1993;**84**(4):438–44. https://doi.org/10.1111/j.1349-7006.1993.tb00155.x.

124. Arisan S, Sever A, Obakan-Yerlikaya P *et al.* Targeting Methionine Metabolism Reveals AMPK-SAMTOR Signaling as a Therapeutic Vulnerability in Prostate Cancer. *Biology* 2025;**14**(5):507. https://doi.org/10.3390/biology14050507.

125. Wang ZB, Long MH, Yu P *et al.* Spatial profiling of the metabolism-immune axis in ovarian cancer. *Front Pharmacol* 2026;**16**:1672020. https://doi.org/10.3389/fphar.2025.1672020.

126. Chen P, Geng H, Ma B *et al.* Integrating spatial omics and single-cell mass spectrometry imaging reveals tumor–host metabolic interplay in hepatocellular carcinoma. *Proc Natl Acad Sci* 2025;**122**(31):e2505789122. https://doi.org/10.1073/pnas.2505789122.

127. Estimated Marginal Means, aka Least-Squares Means • emmeans. n.d. https://rvlenth.github.io/emmeans/ (22 Mar. 2026, date last accessed).

128. Brooks M E, Kristensen K, Benthem K J ,van *et al.* glmmTMB Balances Speed and Flexibility Among Packages for Zero-inflated Generalized Linear Mixed Modeling. *R J* 2017;**9**(2):378. https://doi.org/10.32614/RJ-2017-066.

129. Veličković M, Kadam L, Kim J *et al.* Advanced multi-modal mass spectrometry imaging reveals functional differences of placental villous compartments at microscale resolution. *Nat Commun* 2025;**16**(1):2061. https://doi.org/10.1038/s41467-025-57107-y.

130. Sommella E, Salviati E, Caponigro V *et al.* MALDI Mass Spectrometry Imaging Highlights Specific Metabolome and Lipidome Profiles in Salivary Gland Tumor Tissues. *Metabolites* 2022;**12**(6):530. https://doi.org/10.3390/metabo12060530.

131. Fumet JD, Latour C, Nuttin L *et al.* Tumor-Associated Macrophages Produce PGE2 to Promote CD8+ T-cell Exhaustion and Drive Resistance to PD-L1 Blockade in Microsatellite-Stable Colorectal Cancer. *Cancer Res* 2026;**86**(3):785–801. https://doi.org/10.1158/0008-5472.CAN-25-0079.

132. Hiraide T, Ikegami K, Sakaguchi T *et al.* Accumulation of arachidonic acid-containing phosphatidylinositol at the outer edge of colorectal cancer. *Sci Rep* 2016;**6**(1):29935. https://doi.org/10.1038/srep29935.

133. Zhukovsky MA, Filograna A, Luini A *et al.* Phosphatidic acid in membrane rearrangements. *FEBS Lett* 2019;**593**(17):2428–51. https://doi.org/10.1002/1873-3468.13563.

134. Chalfant CE, Spiegel S. Sphingosine 1-phosphate and ceramide 1-phosphate: expanding roles in cell signaling. *J Cell Sci* 2005;**118**(20):4605–12. https://doi.org/10.1242/jcs.02637.

135. Simon S, Labarriere N. PD-1 expression on tumor-specific T cells: Friend or foe for immunotherapy? *OncoImmunology* 2018;**7**(1):e1364828. https://doi.org/10.1080/2162402X.2017.1364828.

Appendix

Supplementary Figure 1. *Tandem mass spectra for derivatized metabolites.*

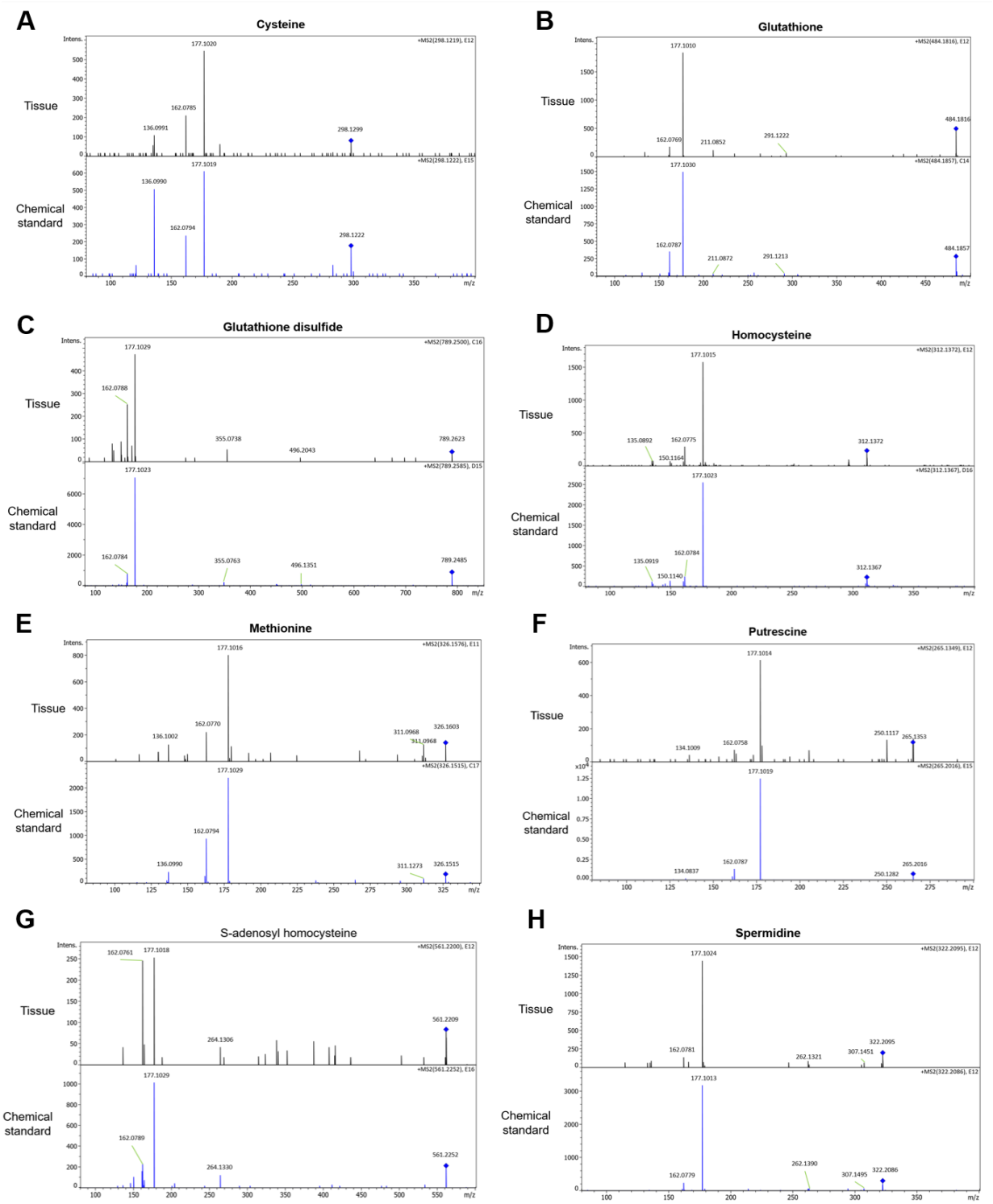

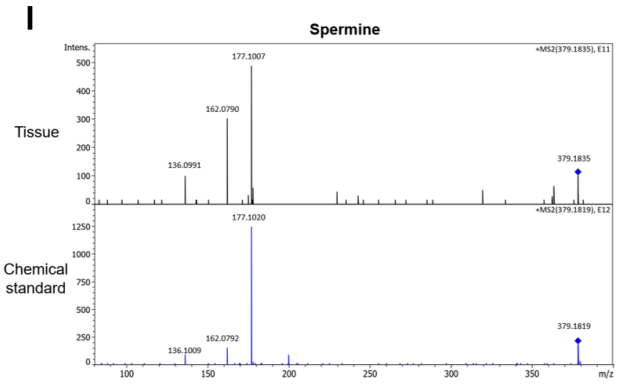

A-I. Tandem mass spectra for metabolites detected with MALDI MSI following TAHS derivatization. For each metabolite, fragments from spectra acquired on tissue are compared to fragments derived from a chemical standard subjected to identical derivatization conditions. Tandem mass spectra were collected with an isolation width of ± 1 *m/z* around the precursor ion mass. These spectra represent tissues and chemical standards described in **Chapter 3.2.4** and **Chapter 3.9.1**.

Supplementary Figure 2. *QuPath workflows for CD8+ cell detection and ROI generation.*

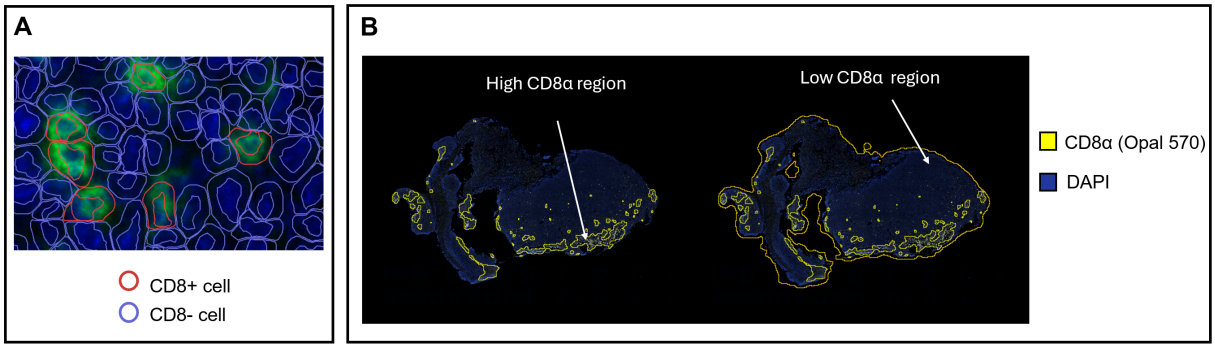

A. Representative immunofluorescence image analyzed in QuPath for automated cell detection and classification. Nuclei were detected using the DAPI channel and CD8+ T cells were identified based on fluorescence intensity in the Opal 570 channel. Cells exceeding the 1+ classification threshold were annotated as CD8+ cells (red outline), while DAPI-stained nuclei for CD8- cells are shown in blue. **B-C.** Example (**A**) high-CD8 and (**B**) low-CD8 regions of interest (ROI) generated using QuPath pixel classification. Pixels with CD8+ cells were identified using the Opal 570 fluorescence channel, and total tissue regions were identified using DAPI signal. High CD8 tissue regions were subtracted from total tissue regions to generate complementary regions representing tumor tissue with low CD8+ T cell abundance. This figure corresponds to analyses performed and discussed in **Chapter 3.2.13.4** and **Chapter 3.3.4.**

Supplementary Figure 3. *Metabolites and lipids associated with CD8+ T cell regions and dietary effects.*

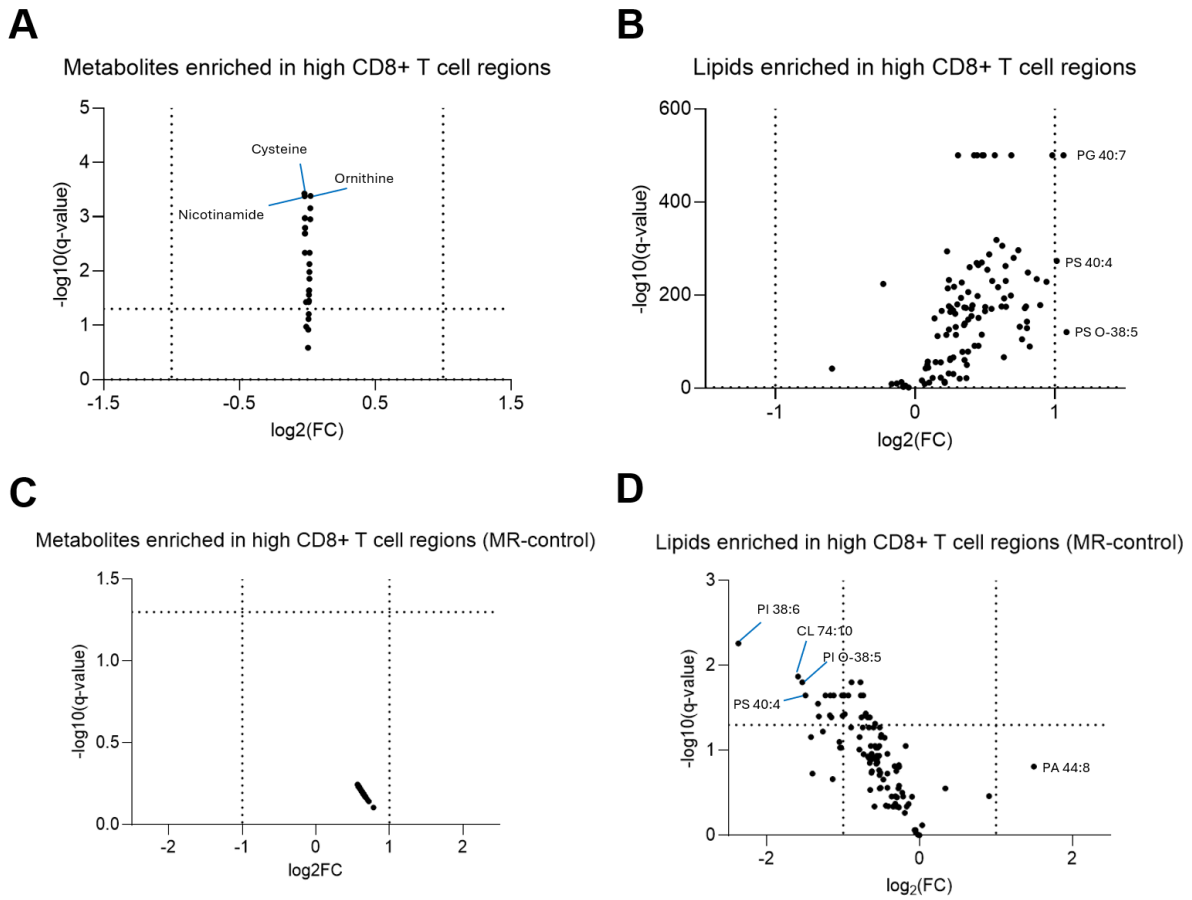

A-B. Volcano plots showing (**A**) metabolite and (**B**) lipid differences between regions with high and low CD8+ T cell abundance across tumors. Log_2 fold changes were calculated as log_2(high CD8+/ low CD8+). The x-axis represents log_2 fold-change and the y-axis represents -log_{10}(q-value). Statistical comparisons were performed on pixel-level data using linear mixed-effects models with region (high *vs.* low $CD8^+$ T cells) as a fixed effect and tumor as a random intercept. False discovery rate was controlled using the BH procedure. Features meeting both $q < 0.05$ and a fold-change threshold > 2 were prioritized for interpretation. For visualization purposes, -log_{10}(q-values) approaching infinity were capped at 500. These plots correspond to data shown in **Figure 10B & C**. **C-D.** Volcano plots evaluating the effect on immune infiltration-associated molecular patterns for (**C**) metabolites and (**D**) lipids. Analyses were restricted to pixels within high- $CD8^+$ T cell regions. For each feature, statistical comparisons were performed as desrcibed above, with diet as a fixed effect and tumor as a random interecept. The x-axis represents the estimated effect of diet on log_2 intensity (MR – control) and the y-axis represents -log_{10}(q-value). In all volcano plots, horizontal reference lines indicate the FDR threshold ($q = 0.05$) and vertical lines indicate the fold-change cutoff ($FC = 2$).

Supplementary Figure 4. *Reproducibility of MALDI IHC protein signals across serial sections.*

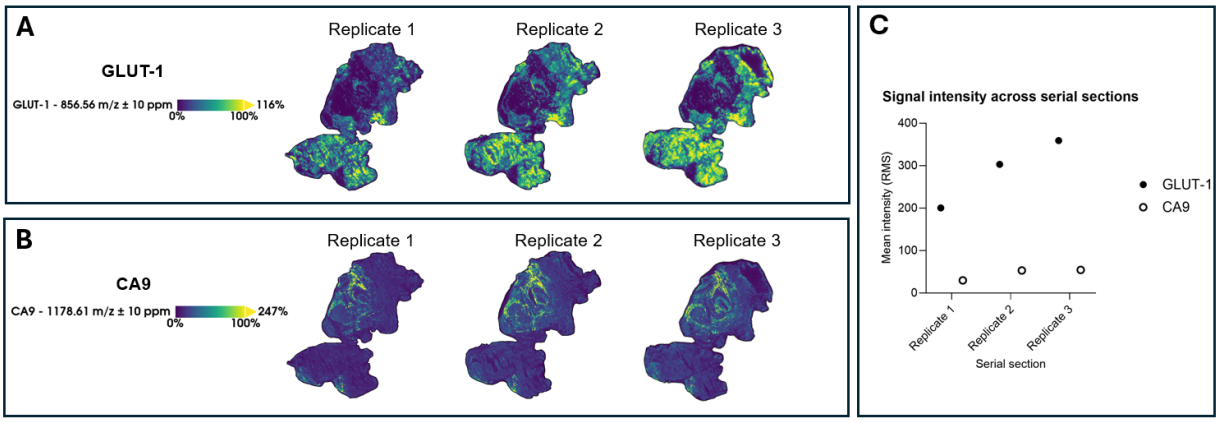

A. Ion images of the PC-MT™ reporter ion corresponding to GLUT-1 across three serial tumor sections analyzed by MALDI IHC. **B.** Ion images of the PC-MT™ reporter ion corresponding to CA9 across the same serial sections. **C.** Mean RMS-normalized intensities of GLUT-1 and CA9 extracted from serial tumor sections. Scatter plots illustrate consistency of protein detection across replicate sections.

Supplementary Figure 5. *Fractional tumor area of segmentation Region 1 by TIL status.*

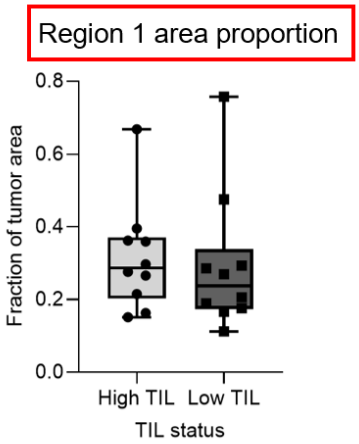

A. Quantification of the fractional tumor area represented by Region 1 in tumors stratified by TIL status (high TIL: n = 10; low TIL: n = 10). Region fractions were calculated as the number of spectra assigned to Region 1 divided by the total number of spectra within the tumor. Differences between groups were assessed using a two-tailed unpaired Mann-Whitney test. Box-and-whisker plots display the median and interquartile range, with whiskers extending to the minimum and maximum values; individual tumors are shown as scatter points. Statistical significance was defined as $p < 0.05$. Corresponding plots for Regions 2 and 3 are shown in **Figure 11 C &**

Supplementary Table 1. *Matrix application parameters.*

Matrix	Concentration (mg/mL)	Solvent	Nozzle temp (ºC)	Plate temp (ºC)	# passes	Flowrate (µL/ min)	Velocity (mm/min)	Track spacing (mm)	Pattern	Pressure (psi)	Gas flowrate (L/min)	Dry time (s)	Nozzle height (mm)	Density (mg/ mm^2)
TAHS	1.25	ACN	55	25	6	100	1200	3	CC	10	2	0	40	2.08×10^{-4}
EDC	2	MS water	37.5	37.5	4	25	1200	3	CC	10	3	2	40	5.56×10^{-5}
4-APEBA	6	MS water	37.5	37.5	4	25	1200	3	CC	10	3	2	40	6.67×10^{-3}
2,5-DHB	15	90% ACN + 0.1% TFA	60	30	14	125	1200	3	CC	10	3	0	40	7.29×10^{-3}
2,5-DHA	15	90% ACN + 0.1% TFA	70	25	20	125	1200	3	CC	10	2	5	40	1.04×10^{-2}
Norharmane	7	2:1 chloroform: methanol	30	25	12	120	1200	3	CC	10	2	30	40	2.80×10^{-3}
CHCA	10	70% ACN + 0.1% TFA + 10 mM ammonium phosphate	60	25	8	100	1350	3	CC	10	2	10	40	1.98×10^{-3}
DAN-HCl	4.44	9:8:1 EtOH: H_2O: HCl	30	25	25	20	1200	2	CC	10	2	13	40	1.63×10^{-3}
NEDC	7	70% MeOH	30	25	14	60	1200	3	CC	10	2	0	40	1.11×10^{-3}
2,5-DHT	10	90% EtOH + 0.1% TFA	60	25	8	100	1350	3	CC	10	2	2	40	2.08×10^{-4}

Supplementary Table 2. *Feature list of methionine cycle metabolites.*

	m/z			
Name	**[M-H]-**	**[M+H]+**	**TAHS derivative**	**4-APEBA derivative**
5-methyl-tetrahydrofolate	458.1788	460.1945	636.2889	813.2832
Arginine	173.1038	175.1195	351.2139	528.2083
Betaine	116.0711	118.0868	294.1812	471.1756
Cystathionine	221.0596	223.0753	399.1697	576.1640
Cysteine	120.0119	122.0276	298.1220	475.1163
Decarboxylated SAM	354.1474	356.1631	532.2575	709.2518
Dimethylglycine	102.0555	104.0712	280.1656	457.1599
Glutathione	306.0760	308.0916	484.1860	661.1804
Homocysteine	134.0276	136.0432	312.1376	489.1320
Methionine	148.0432	150.0589	326.1533	503.1477
MTA	296.0817	298.0974	474.1918	651.1862
Ornithine	131.0820	133.0977	309.1921	486.1865
Oxidized glutathione	611.1441	613.1598	789.2542	966.2486
Putrescine	87.0922	89.1079	265.2023	442.1966
SAH	383.1138	385.1294	561.2238	738.2182
SAM	397.1294	399.1451	575.2395	752.2338
Spermidine	144.1501	146.1657	322.2601	499.2545
Spermine	201.2079	203.2236	379.3180	556.3123
Tetrahydrofolate	444.1632	446.1788	622.2732	799.2676

Supplementary Table 3. *Feature list of metabolites relevant to cancer biology.*

	m/z	
Name	**[M+H]+**	**TAHS derivative**
1-Methylnicotinamide (MNA)	138.0790	314.1734
2-Hydroxyglutarate	149.0450	325.1394
5-methyl-tetrahydrofolate	460.1940	636.2884
5-Phosphoribosylamine	230.0430	406.1374
6-phosphogluconate	277.0325	453.1269
Adenosine	268.1050	444.1994
ADP	428.0370	604.1314
alanine	90.0560	266.1504
alpha-ketoglutarate	147.0293	323.1238
AMP	348.0710	524.1654
Anthranilic acid	138.0560	314.1504
Arginine	175.1200	351.2144
asparagine	133.0610	309.1554

aspartic acid	134.0450	310.1394
ATP	508.0040	684.0984
Betaine	118.0870	294.1814
C14:0	229.2170	405.3114
C16:0	257.2480	433.3424
C16:1	255.2320	431.3264
C18:0	285.2790	461.3734
C18:1	283.2640	459.3584
C18:2	281.2480	457.3424
C20:0	313.3110	489.4054
C20:2	309.2790	485.3734
C20:4	305.2480	481.3424
C20:6	301.2170	477.3114
C22:0	341.3420	517.4364
C22:2	337.3110	513.4054
C22:4	333.2790	509.3734
C22:6	329.2480	505.3424
CTP	483.9920	660.0864
Cystathionine	223.0750	399.1694
Cysteine	122.0280	298.1224
Cystine	241.0320	417.1264
Decarboxylated SAM	356.1630	532.2574
Dimethylglycine	104.0710	280.1654
Glucose	181.0712	357.1656
Glucose-6P	261.0375	437.1320
Glutamate	148.0610	324.1554
Glutamine	147.0770	323.1714
Glutathione (GSH)	308.0920	484.1864
Glutathione disulfide (GSSG)	613.1600	789.2544
Glycine	76.0400	252.1344
GTP	523.9980	700.0924
Histidine	156.0770	332.1714
Homocysteine	136.0430	312.1374
Inosine	269.0890	445.1834
Isoleucine	132.1020	308.1964
Kynurenine	209.0930	385.1874
Lactate	90.0320	266.1264
Lysine	147.1130	323.2074
Malate	135.0293	311.1238
Methionine	150.0590	326.1534
Methylthioadenosine	298.0970	474.1914
NAD	664.1170	840.2114
NADH	666.1330	842.2274

NADP	744.0830	920.1774
NADPH	746.0990	922.1934
Nicotinamide	123.0560	299.1504
Ornithine	133.0980	309.1924
Phenylalanine	166.0870	342.1814
Phosphoribosyl pyrophosphate	390.9596	567.0541
Proline	116.0710	292.1654
Putrescine	89.1080	265.2024
Quinolinic acid	168.0300	344.1244
Ribose 5-phosphate	231.0270	407.1214
S-Adenosyl-L-homocysteine (SAH)	385.1290	561.2234
S-Adenosyl-L-methionine (SAM)	399.1450	575.2394
Serine	106.0500	282.1444
Spermidine	146.1660	322.2604
Spermine	203.2240	379.3184
Tetrahydrofolate	446.1790	622.2734
Threonine	120.0660	296.1604
Tryptophan	205.0980	381.1924
TTP	482.9970	659.0914
Tyrosine	182.0820	358.1764
UTP	484.9760	661.0704
Valine	118.0870	294.1814

Supplementary Table 4. *Miralys™ antibody probes used for mouse tumor tissues.*

Antibody target	PC-MT™ *m/z* $[M+H]^+$	Working concentration (µg/mL)	Species reactivity	Part number (AmberGen)	Lot number
CD3ε	1161.638	1	Mouse	AP1001596	L21000827
CD8α	1350.764	1	Mouse	AP1001595	L21000828
Vimentin	1230.84	1	Human, mouse	AP1001122	L21000143

Supplementary Table 5. *Miralys™ antibody probes used for human tumor tissues.*

Antibody target	PC-MT™ *m/z* $[M+H]^+$	Working concentration (µg/mL)	Species reactivity	Part number (AmberGen)	Lot number
PD-1	1524.83	4	Human, mouse	AP1001188	L21000534
CD4	1659.839	4	Human	AP1001478	L21000744
CD8α	1350.764	4	Human	AP100152	L21000858
GLUT-1	856.56	2	Human, mouse	AP1001199	L21000519
CA9 (SLC2A1)	1178.61	2	Human	A1001459	L21000865